

©Copyright 2013
Michelle Jeung-Eun Lee

Targeted therapies for medulloblastoma: understanding the mechanisms of drug resistance and
exploring new peptide-based therapeutics

Michelle Jeung-Eun Lee

A dissertation
Submitted in partial fulfillment of the
Requirements for the degree of

Doctor of Philosophy

University of Washington
2013

Reading Committee:
James M. Olson, Chair
Robert Hevner
Richard Morrison

Program Authorized to Offer Degree:
Neurobiology & Behavior

University of Washington

Abstract

Targeted therapies for medulloblastoma: understanding the mechanisms of drug resistance and exploring new peptide-based therapeutics

Michelle Jeung-Eun Lee

Chair of the Supervisory committee:

James M. Olson

Professor of Pediatrics, University of Washington

Member, Fred Hutchinson Cancer Research Center

Medulloblastoma, the most common malignant pediatric brain tumor, is currently treated with nonspecific cytotoxic therapies including surgery, radiation, and aggressive chemotherapy. Despite enhancements in treatment strategies, the majority of medulloblastoma cancer patients are left with significant neurological, intellectual and physical disabilities secondary to the effects of these nonspecific cytotoxic therapies on the developing brain. Therefore, additional therapeutic possibilities need to be explored to minimize adverse effects and increase response rate in medulloblastoma patients.

A major challenge of brain tumor surgery is removing all of the tumor tissues while preserving as much healthy brain tissue as possible. The extent of surgical resection can modulate 5-year survival potential by 30-50%, far greater than the impact of any drug - yet there has never been a clinical trial focused on improving surgical outcomes. With the goal of improving detection of cancer foci during surgical resection, our lab developed NP-chitosan-Chlorotoxin-Cy5.5 nanoparticle, also known as tumor paint nanoparticle. In the first part of my thesis, I have shown simple near-infrared fluorescence based methodology to assess the pharmacokinetic properties of these nanoparticles. These data obtained can be incorporated into early nanoparticle synthesis decisions as well as more detailed documentation required for the FDA approval for human clinical trials.

As medulloblastoma exhibits marked intertumor heterogeneity, with at least four distinct molecular variants, patients may require separate therapeutic strategies. The development of a targeted inhibitor of a pathway that is implicated in malignancy, together with identification of patient populations most likely to respond to these therapies may offer more effective therapeutic option than standard treatment strategies available in clinics. The second part of my dissertation work involves investigating the efficacy and pharmacodynamic effects of saridegib (IPI-926), one of the Sonic hedgehog (Shh) pathway inhibitors identified, in Shh-driven

mouse model of medulloblastoma. Although saridegib has shown effectiveness in reducing and eliminating tumor cells in mice initially, drug resistance inevitably occurred. Understanding the mechanisms of resistance to targeted therapy and developing strategies to overcome them are critical for achieving long-term efficacy of targeted therapy in patients. Therefore, I further investigated mechanisms adopted by medulloblastoma cells during cancer progression. I found that overexpression of the Pgp drug transporter contributes to drug resistance in Shh-driven medulloblastoma and the combination of saridegib with Pgp inhibitor partially reversed the drug resistance. Our data provide a strong rationale for the use of a concurrent combination of Shh pathway inhibitors with Pgp inhibitors for the treatment of medulloblastoma and suggest that this approach may delay the development of resistance to Shh pathway inhibitors.

The last part of my dissertation work involved engineering cysteine rich peptides toward the goal of producing Pgp-insensitive therapies for medulloblastoma. Toward this goal, I used a nature-derived knottin peptide as a scaffold and computationally designed variants that could specifically bind to glypican-2, which is overexpressed in medulloblastoma. My aim was to express only a fragment of midkine, a known ligand of glypican-2, that would bind to glypican-2 but not crosslink with growth factor signaling pathways, thereby inhibiting tumor growth. Our ultimate goal is to generate cysteine knot peptide variants capable of targeting and killing brain tumor initiating cells in medulloblastoma patients. This work may provide significant clinical benefit to human medulloblastoma patients, and may serve as an important step towards integrating knottin drugs into mainstream therapy.

TABLE OF CONTENTS

List of Figures.....	ii
List of Table	iii
CHAPTER 1. Introduction	1
The Cerebellum	1
Sonic hedgehog pathway	1
Sonic hedgehog pathway during Cerebellar Development	2
Medulloblastoma	3
Small-molecule Shh pathway inhibitors for cancer therapy	4
Aims of my Dissertation Research	5
CHAPTER 2. Pharmacokinetics and Biodistribution of Tumor Targeting Nanoparticles	10
Summary.....	10
Introduction	11
Results	12
Discussion.....	14
Materials and Methods	15
CHAPTER 3. Drug Resistance Mechanisms in Mouse Model of Medulloblastoma.....	25
Summary.....	25
Introduction	25
Results	26
Discussion.....	32
Materials and Methods	33
CHAPTER 4. Mid-size Medicines for the Treatment of Brain Cancer	50
Summary.....	50
Introduction	50
Results	55
Discussion.....	58
Materials and Methods	59
CHAPTER 5. Conclusion and Future Directions.....	76
References	79

LIST OF FIGURES

Figure Number	Page
Figure 1.1 Cerebellum architecture and development.....	7
Figure 1.2 Mechanics of the vertebrate Shh signaling	8
Figure 2.1 Serum half life of nanoparticles.	18
Figure 2.2 Freezing effects on NIRF signal	19
Figure 2.3 Ex vivo NIRF Imaging of each organ.....	20
Figure 2.4 Comparison of H&E staining and high-resolution NIRF fluorescence imaging	21
Figure 2.5 Biodistribution of NP-chitosan-Cy5.5 and NP-CTX-chitosan-Cy5.5 nanoparticles	22
Figure 2.6 Co-localization of iron oxide nanoparticle core and Cy5 signal in liver	23
Figure 2.7 Rapid and easy method to generate key pharmacokinetic data.....	24
Figure 3.1 The Smo inhibitor saridegib causes regression of mouse medulloblastoma	37
Figure 3.2 Saridegib improves survival in the <i>Ptc^{C/C}</i> medulloblastoma model.....	38
Figure 3.3 3D tumor volume rendering and analysis of pathology	39
Figure 3.4 MRIs demonstrate decreasing tumor volumes during saridegib administration.....	40
Figure 3.5 Monitoring tumor response via MRI	41
Figure 3.6 Effect of saridegib on proliferation and apoptosis	42
Figure 3.7 Saridegib maintenance administration prolongs survival in medulloblastoma mice....	43
Figure 3.8 Mechanisms of resistance in saridegib treated <i>Ptc^{C/C}</i> tumors	44
Figure 3.9 Differential gene expression in vehicle- and saridegib-treated <i>Ptc^{C/C}</i> samples	45
Figure 4.1 A proposed model of Glypican-2 and midkine action	62
Figure 4.2 Midkine sequence and structure.....	63
Figure 4.3 Expression of Glypican-2 in brain cancers	64
Figure 4.4 Computational method to design and study peptide variants	65
Figure 4.5 3D structures of WT and four MKC mutant dimers	66
Figure 4.6 Core C α RMSD/F in MD simulations	67
Figure 4.7 Backbone mobility in WT, and four mutant MKC dimers	68
Figure 4.8 Main chain and side chain contact analysis during MD simulation	69
Figure 4.9 Expressing knottin proteins using Daedalus platform	70
Figure 4.10 Biochemical characteristics of E.Coli and Mammalian WT MKC	71
Figure 4.11 Biochemical characteristics of WT and Mutant1 mammalian MKC.....	72

LIST OF TABLE

Table Number	Page
Table 1.1 Shh pathway inhibitors in current clinical trials.....	9
Table 3.1 Drug concentrations in plasma, brain and tumor	46
Table 3.2 Top 10 networks of the genes significantly altered in saridegib treated Ptc ^{C/C} tumor....	47
Table 3.3 Top genes differentially expressed in saridegib treated Ptc ^{C/C} tumor.....	48
Table 3.4 Primer used for sequencing	49
Table 4.1 Glypican family during embryogenesis and in adult tissues	73
Table 4.2 Detailed description of WT and four MKC mutants.....	74
Table 4.3 Analysis of charged residues and salt bridges formed in WT and mutant MKC	75

ACKNOWLEDGEMENTS

I am truly blessed to have Jim as my advisor and mentor. He has been a role model for me since I first arrived at the University of Washington. His invaluable guidance and insights will always remain within me wherever I am in my life.

My sincerest thanks to committee members, Dr. Robert Hevner, Dr. Richard Morrison, Cecelia Moens, Dr. Dianne Lattemann, and Dr. Thomas Montine for their guidance that has shaped my research and honed my scientific thinking. I also want to thank Dr. Raimondo D'Ambrosio who advised me during my first rotation. I thank many wonderful teachers I had during college years, including Dr. Yong Jeong, and Dr. Daeshik Kim.

I thank all members of the Olson lab for their invaluable support, friendship, and encouragement. In particular, thanks to Sally Ditzler, Joyoti Dey, Stacey Hansen, Beryl Hatton, Chris Mehlin, Colin Correnti, Sarah Leary, Beth Villavicencio, Michelle Sanger, Kyle Pedro, Andrew Richardson, Karina Bloom, Barbara Pullar, Andy Strand, Mark Stroud, Chris Hubert and Phil Olsen, who have made my everyday at work exciting and fun.

I want to acknowledge the rich and supportive environments provided by Neurobiology & Behavior graduate program. I am indebted to Lucia Wisdom and Ann Wilkinson for everything they have done in making my graduate career smooth and exciting. I also want to thank Michele Karantsavelos for taking care of NeuBeh orphan at the Hutch. I wish to thank Dr. Marc Binder, Tina Schulstad, and the Graduate Neuroscience Training Grant for supporting my research work.

Thank you to all of the friends I have made while on this journey. I especially want to thank Nora Lee whose constant support and absolute friendship made my graduate years a wonderful experience. And to Joyoti Dey whose knowledge, friendship, and encouragement have supported me through fun times and difficult times. I also owe a deep thanks to my remarkable friends Jiwon Kim, Jaeyoung Choi, Israel Jung, Su-in Lee, Chris Baik, and Korean-American Scientists and Engineers Association (KSEA) Young Generation. I also would like to thank KSEA-Seattle chapter (especially Dr. Jaehoon Kim, Dr. Junho Cha, Dr. Wookeun Shin, and Mr. Heonmin Lim) and HESED for being my loving community away from home. I also want to thank Braulio Peguero, my Neurobiology & Behavior colleagues, and all my other friends whom I might have failed to mention here. Thank you all! My life has been made richer because of you.

I cannot adequately thank my family for supporting me in every step of my life journey. I am especially indebted to my father who has been a source of inspiration through his own research. He always encouraged me to be curious, ask questions, and follow my heart. My mother has always been my faithful advocate and a source of strength. She always strived to give me the best in life, even if it involved her personal sacrifices. My brothers, David and Alex, have always believed in me and helped me reach my goals. My grandmother has been a source of unconditional love for as long as I can remember. I also want to thank my mother and father-in-law for their constant and unwavering support. I especially want to thank my beloved husband, Taesoo Kim whose love and encouragement allowed me to finish this journey. He is my most enthusiastic cheerleader; he is my best friend; and he is an amazing husband.

Lastly but certainly not the least, I thank my Father in Heaven for providing me with the strength and knowledge beyond my own.

DEDICATION

To all the children and their families who are in this battle against cancer

CHAPTER 1

Introduction

The Cerebellum

The cerebellum is located at the base of the brain and occupies approximately 10% of total brain volume and contains more than half of the total number of neurons in the human brain (Andersen et al., 1992). In addition to its classic functions in motor coordination and balance, there is increasing evidence that the cerebellum is also involved in higher cognitive processes such as emotion and cognition (Hatten and Roussel, 2011; Schutter and van Honk, 2005).

The cerebellar cortex has a remarkably simple laminar structure. It consists of an outer cortical structure and set of subcortical nuclei, the cerebellar nuclei, which project to cerebellar targets (Figure 1.1 A). Previous studies indicate that the dorsomedial ventricular zone gives rise to the major output neurons of the cerebellar cortex, the Purkinje cells, neurons of the cerebellar nuclei, and cerebellar interneurons. A secondary germinal zone forms along the rostral rhombic lip, which generates the cerebellar granule neurons (GNPs) (Figure 1.1 B) (Laine and Axelrad, 2002). These GNPs undergo proliferation at embryonic day (E) 10.5 in mouse, then between E12-E15 they migrate dorsally over to the roof of the cerebellar anlage to form the external granular layer (EGL) (Fairweather et al., 2008; Olive et al., 2009). In the postnatal (P) phase, the GNPs undergo massive proliferation in response to mitogens secreted by Purkinje cells. This proliferation phase peaks at P5-P8 and declines thereafter to stop at around P15. From about P8 on, GNPs in the EGL then exit the cell cycle and initiate their inward radial migration. They move past the growing network of Purkinje cells in the molecular layer (ML). Once passed the ML, GNPs further differentiate to become mature granule neurons and form the internal granular layer (IGL) (Lerner et al., 2011). Neuronal differentiation is completed in the IGL by around P21 in mice and a year after birth in humans (Wang and Zoghbi, 2001). The final development of the cerebellum requires a fine balance between proliferation, migration, differentiation, and cell death.

Sonic hedgehog pathway

The primary cilium is a microtubule based membrane structure that projects from the surface of many eukaryotic cells (Neunaber et al., 2010). The primary cilium receives mechanical and chemical signals from other cells and the surrounding environment, and transmits these signals to the nucleus to elicit a cellular response. Recent work has shown that primary cilia concentrate receptors and signaling

transduction components that are important in development including the Sonic Hedgehog (Shh) signaling (Michaud and Yoder, 2006).

The Shh pathway is an essential embryonic signaling pathway that regulates body patterning and organ development. In adults, Shh signaling is normally dormant, but its inappropriate activation has been linked to several human cancers (Ng and Curran, 2011). Two important molecules in Shh signaling are Patched1 (Ptch1) and Smoothed (Smo), which are transmembrane proteins involved in Shh-dependent trafficking in the primary cilia. In the absence of Shh, Ptch1 represses the activity of Smo presumably by preventing its translocation into primary cilium from intracellular endosomes (Volk and Loscher, 2005). Without activation of Smo, SUFU (Suppressor of fused; important negative regulator of Shh signaling) inactivates the glioma-associated oncogene family zinc finger (Gli) transcription factors, converting full-length Gli proteins into truncated repressor form: Gli-R. Full-length Gli proteins are sequentially phosphorylated by GSK3, protein kinase A, and casein kinase I to form Gli-R, leading to partial degradation (Tempe et al., 2006; Wang and Li, 2006). Gli-R then translocates to the nucleus to repress Shh target genes (Osterlund and Kogerman, 2006; Volk and Loscher, 2005). Binding of Shh to its receptor Ptch1 leads to internalization of Ptch1. The inhibition of Smo is then relieved, allowing accumulation of Smo in the primary cilia where dissociation of SUFU-Gli complex is promoted. This results in nuclear translocation and activation of Gli1 and Gli2 transcription factors, and degradation of the repressor form, Gli-R (Osterlund and Kogerman, 2006; Volk and Loscher, 2005). Gli proteins stimulate the transcription of Shh pathway target genes such as Ptch, Wnt, bone morphogenetic protein (BMP), etc (Figure 1.2).

Detection of loss of function mutations in the Shh signaling pathway in familial basal cell carcinoma (Gorlin syndrome) patients established a clear genetic contribution of Shh pathway activity to oncogenesis (Johnson et al., 1996). Since these initial findings, additional evidence was provided by the identification of somatic mutations that cause activation of Shh signaling in various types of human cancers, including basal cell carcinomas (BCCs), medulloblastoma, rhabdomyosarcoma, leukemia, gastrointestinal, lung, ovarian, pancreatic, breast and prostate cancers (Yang et al., 2010). More definitive proof that aberrant Shh signaling can induce cancers has come from transgenic mouse studies in which conditional loss of function of Ptch1 or gain of function of Smo recapitulate BCC and medulloblastoma (Pasca di Magliano and Hebrok, 2003).

Sonic hedgehog pathway during Cerebellar Development

The characterization of Shh-activated mutant mice has contributed to our understanding of Shh signaling and its role in cerebellar development. In the cerebellum, the expansion of GNPs is orchestrated principally by Shh. Shh is secreted by the Purkinje cells around E17 and drives the proliferation of GNPs

in the postnatal phase of cerebellar development in the EGL. Shh regulates both size and foliation of the cerebellum (Corrales et al., 2006), and the duration and intensity of the proliferation phase of EGL is critical for the final morphology and function of the cerebellum. Persistent Shh signaling results in uncontrolled proliferation of GNPs and can cause medulloblastoma, a cerebellar pediatric cancer.

Medulloblastoma

Medulloblastoma is the most common malignant pediatric brain tumor (Becker et al., 2005). It is thought to arise from genetic anomalies in developmental pathways required for normal maturation of the cerebellum. The median age at diagnosis is 5 years with the range extending into young adulthood. Standard treatment strategies for medulloblastoma involve nonspecific cytotoxic therapies including surgical resection, whole-brain and spinal cord radiation, and aggressive chemotherapy. The overall survival rate for patients with medulloblastoma has reached 70-80% under standard treatment protocols (Siegel et al., 2012; Rutkowski et al., 2010). Although the survival rates have improved over the years, the majority of survivors suffer from significant neurological, intellectual and physical disabilities secondary to the effects of nonspecific cytotoxic therapies on the developing brain (Becker et al., 2004).

Gene expression profiling of primary medulloblastomas have led to identification of multiple molecularly distinct subgroups (Amaral et al., 2004; Cho et al., 2011; Ramalho et al., 2004). Genetic and molecular genetic analyses of medulloblastoma have identified changes in the regulation of signaling pathways that are important for cerebellar progenitor cell neurogenesis, including pathways that promote growth. Four principle subgroups of medulloblastoma include WNT, SHH, Group 3 and Group 4. (Since less is known about the biology of the Group 3 and Group 4, the generic names are used until the underlying biology driving these subgroups is better characterized). Medulloblastoma subgroups have highly disparate cytogenetics, mutational spectra and gene expression signatures, in addition to divergent clinical phenotypes such as patient demographics, tumor cell histology and patient outcome. For instance, studies of genetically engineered mice show that medulloblastoma tumors arise from at least two different progenitor populations. SHH subgroup medulloblastomas are generated from cerebellar GNPs (Metcalf and de Sauvage, 2011) whereas WNT subgroup tumors develop from lower rhombic lip progenitors (Tremblay et al., 2009). There is also marked clinical difference between WNT and SHH subgroup medulloblastomas. WNT medulloblastomas have the best prognosis of any subgroup (greater than 95% survival) and are the least common of the four subgroups (Ellison et al., 2011). These tumors typically occur in older children, and exhibit class histology. WNT subgroup ubiquitously harbors somatic mutations of CTNNB1 that promote stabilization and nuclear localization of β -catenin (Zurawel et al., 1998). Meanwhile, SHH medulloblastomas represent intermediate prognosis subgroup with overall survival ranging from 60% to 80% (Taylor et al., 2012). SHH subgroup is predominant in infants and

young adults, and desmoplastic histology is almost exclusively restricted to this group. Around half of SHH activated medulloblastoma tumors have confirmed loss of PTCH1, loss of SUFU, or gain-of-function SMO mutations (Brugieres et al., 2010; Yauch et al., 2009).

The establishment of the subgrouping of medulloblastoma has revamped how medulloblastoma needs to be viewed and approached in the design of future clinical trials. As each subgroup has very distinct molecular genetic profiles, each requires subgroup specific therapeutic approach. Although the initial studies with Shh inhibitors have shown early promise, targeted therapies based on genetics and molecular characteristics have not been routinely implemented in the clinic. It is expected that in the future, medulloblastoma patients will be stratified and treated based on their biological markup of their disease, which will hopefully lead to improved patient outcomes with less adverse effects. My dissertation was aimed at furthering our understanding of Shh pathway targeted therapy and hence I focus on the Shh pathway inhibitors in the section below.

Small-molecule Shh pathway inhibitors for cancer therapy

Our understating of Shh signaling pathway signaling has led to the discovery of small molecule inhibitors of the Shh pathway. The discovery of these Shh pathway modulators provides an avenue to regulate the activity of Shh pathway implicated in medulloblastoma, advanced basal cell carcinoma (BCC), pancreatic cancer, prostate cancer and developmental disorders. The first generations of Shh inhibitors are cyclopamine and jervine, which were isolated from corn lilies as compounds causing teratogenic effects in lambs (Bryden et al., 1971; Winkler et al., 2009). Cyclopamine interfere with Shh signaling by binding directly to Smo protein (Chen et al., 2002) and was shown to inhibit proliferation and to induce apoptosis in various types of cancers. Despite the attractive pharmacological effects against a number of cancer xenografts, the clinical development of cyclopamine as a therapeutic agent in cancer was hampered by its poor pharmacokinetic properties (e.g., weak potency, rapid clearance, chemical instability). This encouraged a search for novel inhibitors with preferential characteristics for drug development. Therefore, several synthetic and semi-synthetic small molecule inhibitors of Shh signaling pathway have been discovered. Currently, all the Shh pathway therapeutics in clinical trials act at the level of Smo and thus would not be effective against tumors that harbor molecular lesions downstream of Smo (See Table 1.1 for summary of Smo inhibitors in clinical trials).

GDC-0449 (vismodegib) produced by Genentech is a more potent and specific synthetic oral Smo inhibitor that showed activity in inhibiting the tumor growth. GDC-0449 was recently approved by the Food and Drug Administration (FDA) for treatment of advanced BCC (January 2012). Clinical trials are ongoing in various cancers including small cell lung cancer, pancreatic, esophageal, gastric, breast and prostate cancers. In a case report of a medulloblastoma patient, treatment with GDC-0449 initially

resulted in rapid regression of the tumor and reduction of symptoms; however, the tumor ultimately relapsed with D473H resistance mutation in Smo (Yauch et al., 2009).

LDE225 produced by Novartis is another small molecule inhibitor that specifically inhibits Smo in the Shh signaling pathway. LDE225 is currently being investigated in Phase I or II trials in patients with BCC and other advanced solid tumors. The results demonstrated that LDE225 was well tolerated and LDE225-treated BCCs displayed complete clinical response in three cases, partial response in nine cases, and no response in one case (Skvara et al., 2011). In Patched mutant medulloblastoma mice, LDE225 has been shown to inhibit Shh signaling and induced tumor regression. However, as for GDC-0449, drug resistance was observed during the course of LDE225 treatment. The mechanisms of resistance include amplification of Gli2, point mutations in Smo, and upregulation of signaling pathways that interact with Shh, such as PI3K. Interestingly, the combination treatment of LDE225 with PI3K inhibitor or dual PI3K-mammalian target of rapamycin (mTOR) inhibitor markedly delayed the development of resistance, suggesting the importance of multiple signaling inhibitions for cancer therapy (Buonamici et al., 2010).

Saridegib (IPI-926) produced by Infinity is a semi-synthetic cyclopamine analog that inhibits Smo in the Shh pathway. Several Phase I and II clinical trials using saridegib were conducted in different types of cancers including pancreatic cancer, and chondrosarcoma. Despite the promising preclinical studies, the saridegib clinical trial was stopped in all trials when interim analysis revealed that metastatic pancreatic cancer patients treated with gemcitabine plus placebo showed longer survival than patients on reduced dose of gemcitabine plus saridegib.

Trials with Shh pathway inhibitors showed beneficial effects on various cancers. Shh directed therapeutics could provide promising strategies for treating Shh-activated cancers. It is better to use a specific small molecule inhibitor in order to minimize adverse effects; however, targeting one molecule may not be sufficient enough to kill cancer cells and reverse malignant status because cancer is a disease of multiple signals and signal networks, which contributes to treatment failure. Therefore, multi-targeting approach (targeting Shh signaling combined with inhibitors of other key pathways such as Akt, Wnt, Notch, TGF- β) could become a novel strategy for designing personalized therapy to win the battle against cancer.

Aims of my Dissertation Research

The objective of my dissertation research was to understand the molecular mechanisms underlying tumorigenesis and drug resistance in medulloblastoma with the goal of developing more efficacious targeted therapies. The three areas I have been interested in are 1) developing a molecular imaging agent for the localization of the malignant tumor during surgical resection, 2) understanding drug

resistance mechanisms against Shh pathway targeted therapy and strategies to overcome drug resistance, and 3) developing tumor specific peptide variants that binds to receptors present on tumor cells. Toward this goal, first, I aimed to characterize pharmacokinetic properties of dual modality (MRI and NIR fluorescence imaging) tumor targeting agent for the diagnosis, monitoring, and surgical guidance of cancer. The findings from this study are described in Chapter 2. Toward my second aim, a vast array of resistance mechanisms, involving mutations or amplification of the target protein, overexpression of downstream signaling pathways, possibility of crosstalk with other signaling pathways, and overexpression of drug transporters, were examined. My finding that altered expression and activity of P-glycoprotein (Pgp) drug transporter plays a critical role in drug resistance in Shh-driven mouse model of medulloblastoma is described in Chapter 3. Finally, I aimed to develop and computationally design knottin peptides that target specific proteins and pathways that are overly expressed in medulloblastoma tumors. These peptides would eventually be used to target chemotherapy specifically to medulloblastoma cells. My findings are summarized in Chapter 4.

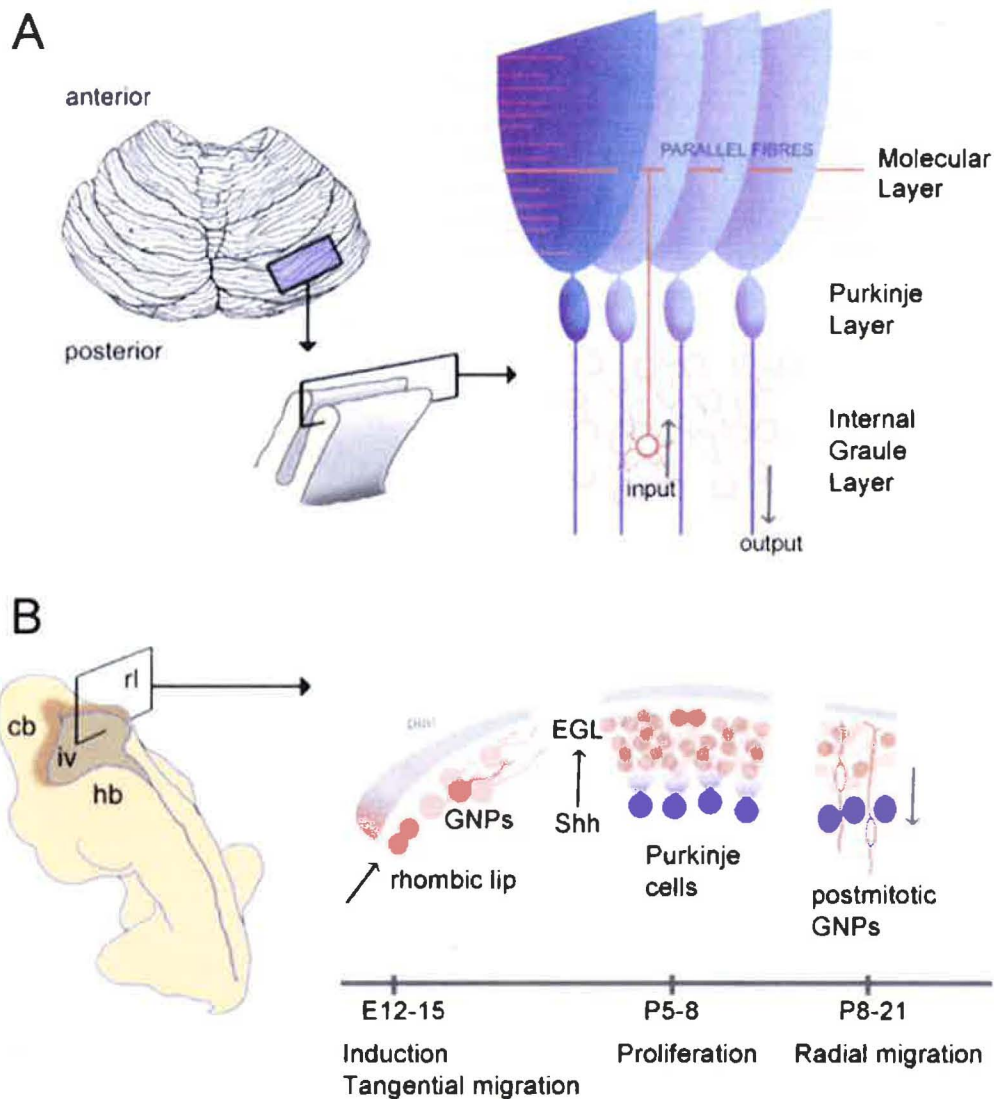


Figure 1.1 Cerebellum architecture and development

(A) Arrangement of Purkinje cells and granule cells in a layered cerebellum follows a stereotyped arrangement. A subpial molecular layer is composed of Purkinje cell dendritic trees and granule cell axons and few cell bodies. A monolayer of Purkinje cell bodies separates the molecular layer from hugely populous internal granule layer. (B) This arrangement develops via two phases of proliferation and migration. At the rhombic lip, GNPs migrate tangentially into a superficial, transient external granule layer. Here, they proliferate in a series of symmetrical divisions in response to Shh signaling from underlying Purkinje cells. The vastly expanded post-mitotic derivatives of the EGL then migrate through the Purkinje cell layer. (Figure modified from Butts and et al., 2010)

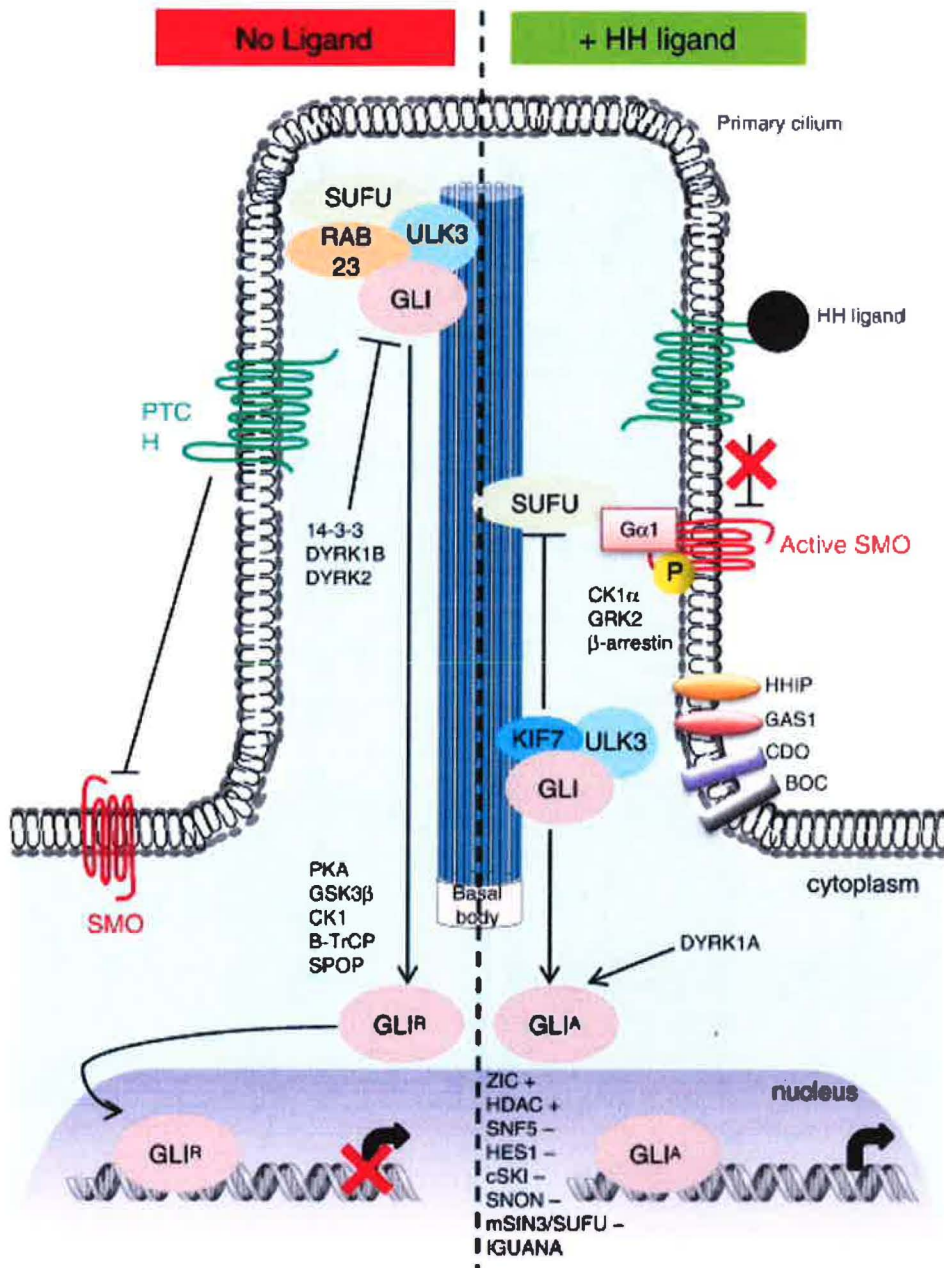


Figure 1.2 Mechanics of the vertebrate Shh signaling

(A) In the absence of Shh, its receptor Patched1 (PTCH1), located on the plasma membrane inhibits Smoothed (SMO) by possibly exporting an endogenous agonist of SMO outside the cell. Under this circumstance, different kinases phosphorylate Gli2/3, creating a repressor form of this transcription factor (Gli^R). Iguana and SUFU prevent the active form of Gli (Gli^A) from transactivating Shh-responsive genes. (B) Upon binding of Shh, Ptc1 is internalized relieving the inhibition on SMO. Intracellular accumulation of PTCH1 activates SMO, which itself translocate to the plasma membrane in primary cilium. SMO then engages yet unknown components of the signaling pathway, culminating in activation of the Gli proteins, which regulate the expression of Shh target genes. (Figure taken from Rubin and de Perrot, 2012)

Agent	Target	Manufacturer	Phase	Number of trials	IC50 μ M (Potency compared to cyclopamine)	Response	Reference
GDC-0449	Smo	Genentech	Phase II	28	\sim 0.003 (~170X)	BCC (18/33) Metastatic BCC (9/18) Advanced BCC (3/3) Medulloblastoma (1/1)	(Doggrell, 2010) (Amin et al., 2010) (LoRusso et al., 2011)
LDE225	Smo	Novartis	Phase I, II	5	N.D	NBCCS with BCC (12/13) Medulloblastoma (no result)	(Skvara et al., 2011)
PF-04449913	Smo	Pfizer	Phase I	2	N.D		
Saridegib (IPI-926)	Smo	Infinity	Phase I, II	2	0.015 (~30X)	BCC (4/17)	
BMS-833923	Smo	Bristol-Myers Squibb	Phase I, II	5	N.D		

Table 1.1 Shh pathway inhibitors in current clinical trials

Abbreviations: N.D, not determined

CHAPTER 2

Rapid Pharmacokinetic and Biodistribution Studies Using Chlorotoxin-Conjugated Iron Oxide Nanoparticles: A Novel Non-Radioactive Method

Modified from an article published in Plos One:

Lee MJ-E, Veisoh O, Bhattarai N, Sun C, Hansen SJ, et al. Rapid Pharmacokinetic and Biodistribution Studies Using Chlorotoxin-Conjugated Iron Oxide Nanoparticles: A Novel Non-Radioactive Method. (2010) PLoS ONE 5(3): e9536. doi:10.1371/journal.pone.0009536

Summary

Recent advances in nanotechnology have led to the development of biocompatible nanoparticles for in vivo molecular imaging and targeted therapy. Many nanoparticles have undesirable tissue distribution or unacceptably low serum half-lives. Pharmacokinetic (PK) and biodistribution studies can help inform decisions determining particle size, coatings, or other features early in nanoparticle development. Unfortunately, these studies are rarely done in a timely fashion because many nanotechnology labs lack the resources and expertise to synthesize radioactive nanoparticles and evaluate them in mice.

To address this problem, we developed an economical, radioactivity-free method for assessing serum half-life and tissue distribution of nanoparticles in mice. Iron oxide nanoparticles coated with chitosan and polyethylene glycol that utilize chlorotoxin as a targeting molecule have a serum half-life of 7–8 hours and the particles remain stable for extended periods of time in physiologic fluids and in vivo. Nanoparticles preferentially distribute to spleen and liver, presumably due to reticuloendothelial uptake. Other organs have very low levels of nanoparticles, which is ideal for imaging most cancers in the future. No acute toxicity was attributed to the nanoparticles.

We report here a simple near-infrared fluorescence based methodology to assess PK properties of nanoparticles in order to integrate pharmacokinetic data into early nanoparticle design and synthesis. The nanoparticles tested demonstrate properties that are excellent for future clinical imaging strategies and potentially suitable for targeted therapy.

Introduction

Nanomedicine, the application of nanotechnology in the practice of medicine, offers many advantages over conventional therapeutics. Properly developed, nanoparticles and other nanoscale therapeutics offer improved intracellular penetration, enhanced absorption into selected tissues, better pharmacokinetic (PK) properties, increased clinical efficacy and reduced toxicity (Peer et al., 2007). Nanomedicine faces several challenges during preclinical development. Recently, the Food and Drug Administration (FDA) and the Alliance for NanoHealth (ANH) recognized seven scientific challenges in bringing nanomedicine to patients (Peer et al., 2007). Among the seven challenges, three emphasize the importance of studying the pharmacokinetics of nanotechnology-based therapeutics. These include evaluation of nanoparticle biodistribution following systemic injection, the study of transport across biological barriers, and the development of imaging modalities for tracking the fate of nanomedicine over time.

Pharmacokinetic and biodistribution characteristics are important parameters to consider when designing and testing novel nanoparticles. In order to achieve an effective level of nanoparticles in the target tissue or tumor site, targeted nanoparticles should transition from circulating blood to the tissue of interest and bind to its molecular target as a first step in nanoparticle retention or cellular internalization. Unfortunately, many types of systemically injected nanoparticles are rapidly cleared from the blood stream by the reticuloendothelial system (RES) and the mononuclear phagocytic system (MPS) mainly through the liver, spleen, and bone marrow (Peer et al., 2007; Ferrari, 2005) resulting in a low therapeutic index. Development of nanoparticles that avoid rapid clearance is a necessary requirement for sufficient delivery to the desired target (Ferrari, 2005; Alexis et al., 2008). Nanoparticles with an extremely high circulation half-life should also be avoided as this may contribute to off target tissue toxicity and reduced signal-to-noise ratio due to non-specific binding.

Nanoparticle core, linker, and coating materials along with synthesis and purification techniques influence serum half-life and biodistribution (Emerich and Thanos, 2006). Linker molecules like chitosan can sterically stabilize the corona, and prevent aggregation. Surface modification of nanoparticles with synthetic polymers like polyethylene glycol (PEG), polyvinyl alcohol (PVA), or polysaccharide can enhance solubility of hydrophobic materials, minimize nonspecific binding, prolong circulation time, and enhance tumor specific targeting (Laurent et al., 2008; Sheng et al., 2009). Since chemical and physical properties of nanoparticles determine their in vivo fate, it is desirable to measure pharmacokinetic profiles early in the development process so that this information can be used to influence nanoparticle design and candidate prototype selection. Traditionally, pharmacokinetic studies were based on either quantification of the therapeutic agent (e.g., using HPLC and mass spectroscopy) or by radiolabeling the agent and measuring radioactivity in homogenized tissue (Rossin et al., 2005; Kaul and Amiji, 2004). Both

approaches are relatively expensive, time consuming, and outside of the expertise of many nanoparticle synthesis laboratories. Even though pharmacokinetic data is critical in making decisions regarding particle size, coating, synthesis procedures, and purification methods these studies are often conducted in the late stages of nanoparticle development due to these roadblocks. Here we describe a new, fast, and economical method for evaluating PK and biodistribution properties of nanoparticles using near infrared (NIR) based technology that allows these critical steps to be performed early in the nanoparticle development.

Some groups, including ours, incorporate near infrared fluorophore (NIRF) molecules into nanoparticle synthesis to facilitate intra-operative visualization of targeted cells or tissues (Josephson et al., 2002; Kircher et al., 2003). We capitalized on this reporter molecule to assess serum half-life and biodistribution of a chitosan-conjugated iron oxide core nanoparticle. This nanoparticle serves as a platform to deliver targeted anticancer therapeutics and as an imaging agent for visualizing tumors in mice (Veisheh et al., 2009). The results suggest potential utility of these nanoparticles for future medical applications. This paper describes the development of a new non-radioactive method for assessing serum half-life, biodistribution and in vivo stability using the NIRF, Cy5.5. This novel method provides 21-micron histological resolution for identifying populations of cells that bind to the nanoparticles. We demonstrate this new technique by analyzing the tissue distribution and serum half-life of a new chitosan-conjugated nanoparticle.

Results

Serum Half-Life of Nanoparticles

For assessment of serum half-life, we focused on a reproducible, quantitative assay that utilized the NIRF dye, Cy5.5, which was incorporated into the nanoparticle. Blood was collected from mice at 1, 3, 6, 10, 24, and 48 hours after injection of 200 μ l of 1 mg/ml of NP-chitosan-CTX-Cy5.5 or the non-targeted control, NP-chitosan-Cy5.5. Blood was centrifuged and the plasma was collected for analysis. The blood plasma was added to a 96 well clear bottom plate and scanned using the Odyssey scanner. The Cy5.5 signal could be readily detected and quantified in small volume blood samples using a 96 well format NIR fluorescence scanner as described in the Methods section. NP-chitosan-CTX-Cy5.5 exhibited a longer circulation time than NP-chitosan-Cy5.5 (Figure 2.1). Exponential decay analysis of NP-chitosan-CTX-Cy5.5 revealed an elimination half-life of 8 hours compared to 7 hours for NP-chitosan-Cy5.5.

Biodistribution

Radioactivity-based pre-clinical biodistribution studies typically fail to show anatomic resolution that would distinguish signal differences among subpopulations of cells within a tissue. Likewise, whole organ biophotonic imaging for fluorescence-labeled therapeutics also lacks microscopic resolution and further suffers from the fact that the quantitative data from whole organs is dramatically affected by size and shape of the organ. After demonstrating that the Cy5.5 fluorescent signal is retained after freezing (Figure 2.2), we developed an assay in which a NIR fluorescence scanner was used to quantitatively assess Cy5.5 signal at 21-micrometer resolution.

Mice were injected through the tail vein with 200 μ l of 1 mg/ml NP-chitosan-Cy5.5 or NP-chitosan-CTX-Cy5.5. Whole organs were removed 6, 24, or 48 hours after injection and scanned using the IVIS-100 imaging system (Figure 2.3A). All tissue was frozen in OCT then sliced in 12-micron sections and mounted on glass slides. The slides were scanned on the Odyssey NIR scanner and images were obtained using the 700 nm channel (Figure 2.3B). The slice assay revealed, with anatomic resolution, small areas within certain organs that bind the conjugate that would be missed by methods that involved homogenization or whole organ imaging. For example, signal was present in the wall of the aorta in heart slices (Figure 2.4C), but not evident on whole organ imaging (Figure 2.3). While the amount of signal is small, the data show the capability of the method to detect small foci of NIRF-positive cells within an organ that otherwise appears to have minimal signal.

Consistent with whole-organ biophotonic images, significant localization was seen in slices from the tissues of the RES (liver, spleen, and bone marrow) as well as the kidneys (Figure 2.3 and 2.4). Histological analysis revealed that binding was not uniform in these tissues. The binding patterns in liver and spleen suggested macrophage uptake (Figure 2.4). High concentration of nanoparticles was revealed in the spleen white pulp. In kidney, the signal localized to the renal cortex.

Similar to most nanoparticles, tissue binding was higher in spleen and liver than other tissues. In spleen and liver, NIRF signal decreased slightly between hour 6 and hour 48 (Figure 2.5). With the exception of bone marrow, in which 4–5 fold increase in signal over background was observed, the signal in all other whole organs was statistically indistinguishable from background. There was no significant difference in normal tissue biodistribution between untargeted and chlorotoxin-targeted nanoparticles indicating that the targeting peptide influences specific binding to tumors (Veisheh et al., 2009; Pirollo and Chang, 2008), but does not affect non-specific binding to normal tissue (Figure 2.5).

Nanoparticle Stability

To analyze the stability of nanoparticle suspensions against agglomeration within the biological system, nanoparticles were kept in phosphate buffered saline (PBS) of physiologic pH. No apparent size change was observed after incubation of nanoparticles in media for several months. Nanoparticles were

found to be stable with no sign of aggregation or loss of functionality (Veiseh et al., 2009). The stability of the Cy5.5-nanoparticle-nanoparticle bond upon storage in vivo was confirmed by Prussian-blue staining for iron oxide nanoparticle core and Cy5 fluorescent signal in the liver. Colocalization of Prussian blue staining and Cy5 fluorescent indicate that Cy5.5 fluorophores remain attached to iron oxide nanoparticle, confirming the stability of nanoparticles in vivo (Figure 2.6).

Toxicity Studies

Guided by the biodistribution data, tissues were carefully evaluated for evidence of nanoparticle toxicity. Mice received a single intravenous injection of 200 μ l of 1 mg/ml of NP-chitosan-Cy5.5 or NP-chitosan-CTX-Cy5.5. All mice were evaluated twice weekly for the duration of the studies for clinical symptoms of toxicity. None were observed. Seven days after the injection, tissue was removed and fixed in 10% formalin. A veterinary pathologist reviewed Hematoxylin and Eosin (H&E)-stained tissue sections from liver, spleen, kidney, lung, heart, colon, skeletal muscle, ovary/testes, small intestine, and brain of mice injected with control or CTX-targeted chitosan-conjugated nanoparticles (data not shown). Despite relatively high levels of nanoparticles in liver, spleen, and bone marrow, no significant lesions were observed. In kidneys, mild multifocal tubular abnormalities were observed in subsets of both nanoparticle injected and non-injected groups, leading to the conclusion that these mild differences in histological appearance were not related to nanoparticle injection. None of the other tissues had abnormal findings. Overall, the toxicity studies indicate that the nanoparticles were well tolerated and that renal function and renal pathology should be closely monitored if the non-targeted nanoparticles are advanced toward clinical use.

Discussion

The goal of our approach is to provide rapid and easy monitoring of nanoparticle distribution. In the early stages of nanoparticle development, when decisions are being made about materials, coatings, synthetic processes and purification, key PK data can be generated in the same mice that are utilized to assess nanoparticle targeting to cancer cells or other targets. The stability of nanoparticles is often studied in biological media such as PBS and Dulbecco's modified Eagle's medium (DMEM) with 10% of fetal bovine serum (FBS) (Fang et al., 2009). However, nanoparticles in solutions with physiological salt concentration, pH and temperature cannot fully recapitulate different types of cells or immune system in biological system. Therefore, we focused on evaluating nanoparticles pharmacokinetic in vivo. In this setting, we found that Cy5.5 signal perfectly matched Prussian Blue staining for the iron oxide nanoparticles, indicating exceptional in vivo stability. The PK data can be utilized to inform development

and make “go, no-go” decisions. Importantly, serum half-life, biodistribution, and stability are all evaluated in the same mice, which reduces the number of research animals utilized (Figure 2.7) and all data is generated on a single piece of equipment, which reduces capital equipment costs.

The serum half-life of NP-chitosan-CTX-Cy5.5 and NP-chitosan-Cy5.5 is 7–8 hour, which is within the ideal therapeutic range. We attribute the prolonged serum half-life to the PEG surface coating with chitosan linker, which was designed to reduce nanoparticle agglomeration and the rate of nonspecific phagocytosis of the nanoparticles by reticuloendothelial cells. Nanoparticle serum levels in the first 24 hours, coupled with the biodistribution data, indicate that both liver and kidney are involved in nanoparticle elimination. The serum half-life of the tested nanoparticles was in the range that is generally considered optimal.

Biodistribution studies revealed expected localization in kidney, spleen, and liver for both targeted and non-targeted nanoparticles. High uptake by mononuclear phagocytic system in the liver and spleen are one of the greatest challenges of using nanoparticles for tumor targeting. Our new approach allows quantitative measure of nanoparticles distributed in deep tissues of MPS-rich organs with anatomical resolution.

The biodistribution findings have different implications for therapeutics versus imaging. For imaging tumor foci, the primary concern is the signal in tumor compared to adjacent normal tissue and it does not matter whether other organs have higher signal than the tumor unless they are potential sites of metastases or might obscure visualization of the tumor area by emitting bright signal. In contrast, targeted therapeutics depends on either having higher targeting to tumor tissue than all other organs that might be adversely affected by the therapeutic payload or choosing to deliver a therapy that does not adversely affect organs that sequester or excrete nanoparticles nonspecifically. NIR imaging enables relatively quick and simple measurements of serum half-life, biodistribution and stability. These data can be incorporated into early nanoparticle synthesis decisions as well as more detailed documentation required for nanoparticles that are submitted to the FDA for human clinical trials. The data obtained from NIR fluorescence imaging provides sensitive, specific, and real-time pre-clinical information that complements efficacy studies focused on tumor visualization.

Materials and Methods

Nanoparticle Synthesis and Characterization

Nanoparticles were synthesized as described previously (Veiseh et al., 2009). Transmission electron microscopy (TEM) has shown the iron oxide cores with a mean diameter of 7 nm. BCA protein quantification and fluorescence quantification determined a yield of 16.2 CTX peptides and 1.5

fluorophores per nanoparticles on average.

Serum Half-Life

All animal studies were conducted in accordance with Fred Hutchinson Cancer Research Center's Institute of Animal Care and Use Committee (IACUC) approved protocols as well as with federal guidelines. 3–5 month old mice on a C57BL6 background (Charles River Laboratories, Inc.) were injected through the tail vein with 200 μ l of 1 mg/ml targeted NP-CTX-chitosan-Cy5.5 nanoparticle (n= 3) or non-targeted NP-chitosan-Cy5.5 control nanoparticles (n= 3). At six different time points after injection, 1, 3, 6, 12, 24, and 48 hours, blood was collected by retro-orbital eye bleed or terminal heart puncture. Because of limitations on the amount of blood that can be drawn from each animal, no animal was used for more than two time points. Blood samples were drawn from three independent mice for each time point and frozen at -80°C until analysis. Samples were thawed at room temperature for 30 minutes prior to analysis. Whole blood was spun using a benchtop centrifuge for 5 minutes at 10,000 rpm to separate the plasma. 50 μ l of plasma was then added to a 96 well clear bottom plate. The plate was scanned on the Odyssey NIR fluorescence imaging instrument (LI-COR, Lincoln, NE) using the 700 nm-channel (exc = 685 nm with em= 705 nm) to measure Cy5.5 fluorescence signal. Concentration of nanoparticles was interpolated from the NP-chitosan-Cy5.5 fluorescence standard curve. A separate study was done in advance to ensure that fluorescent signal was not modified by freezing (Figure 2.2). The stability of infrared signal during the process of freezing was addressed in a group of mice receiving free Cy5.5 dye and CTX-Cy5.5. Mice were injected via lateral tail vein with 100 μ l of either Cy5.5 or CTX-Cy5.5. 24 hours post-injection the animals were euthanized and the kidneys removed. One kidney was homogenized in 1 ml of PBS, 30 μ l was added to a 96 well plate and the NIRF signal was analyzed using the Odyssey imaging system before and after the freezing process.

Biodistribution of Nanoparticle

Animals were injected via tail vein with 200 μ l of 1 mg/ml NPCTX-chitosan-Cy5.5 targeted nanoparticle, or NP-chitosan-Cy5.5 non-targeted control nanoparticles. Three additional non-injected animals were included as controls. 6, 24, or 48 hours after injection (n= 3) the animals were euthanized and tissues were dissected from twelve different organs: kidney, spleen, liver, colon, brain, heart, lung, pancreas, muscle, small intestine, gonads, and bone marrow. Bone marrow was extracted by flushing the bone marrow cavity with phosphate-buffered saline (PBS) then centrifuged to pellet the marrow. Each tissue was imaged using the IVIS-100 (Xenogen Co., Alameda, CA). Tissues were then embedded in OCT and kept frozen at -80°C until needed. The frozen tissues were sliced in 12 mm thick sections and mounted onto glass slides. The tissue sections were thawed at room temperature for 30 minutes and the

fluorescence intensity was measured using the Odyssey fluorescence scanner at a resolution of 21 mm. The images were analyzed with the public domain ImageJ software (US National Institutes of Health, Bethesda, MD). The average fluorescence intensity was determined for each tissue type using the same threshold settings (low threshold: 400, high threshold: 20,000). Data are reported as the average channel fluorescence of the tissue, given as relative units after background subtraction. For visual illustrations of fluorescence signals, color maps are generated using Matlab (Mathworks, Natick, MA).

Nanoparticle Stability

Colloidal stability of nanoparticles was evaluated by suspending the nanoparticles in PBS media of physiologic condition (pH 7.4, 37 μ C) for several months. For histology and fluorescence imaging analysis, 12-mm-thick sections were prepared from the same OCT embedded frozen sample as above. Fluorescence imaging of side-by-side non-injected controls and injected liver was performed in the Cy5 channel (exc = 620–650 nm with em = 680–710 nm) using a TissueFax-System (TissueGnostics, Vienna, Austria). The same tissue sections were stained with Prussian blue and nuclear fast red counterstain for visualizing iron nanoparticles. Sections were then imaged with TissueFax.

Toxicity Studies

Additional Mice were injected with 200 μ l of 1 mg/ml NPCTX- chitosan-Cy5.5 (n= 3) or NP-chitosan-Cy5.5 (n= 3) via the tail vein. Seven days after the injection the following organs were harvested and fixed in 10% formalin: brain, heart, lung, liver, spleen, kidney, pancreas, gonad, small intestine, colon, and muscle. The tissues were paraffin embedded and Hemotoxylin and Eosin stained according to standard protocols. Each tissue was analyzed by a veterinary pathologist.

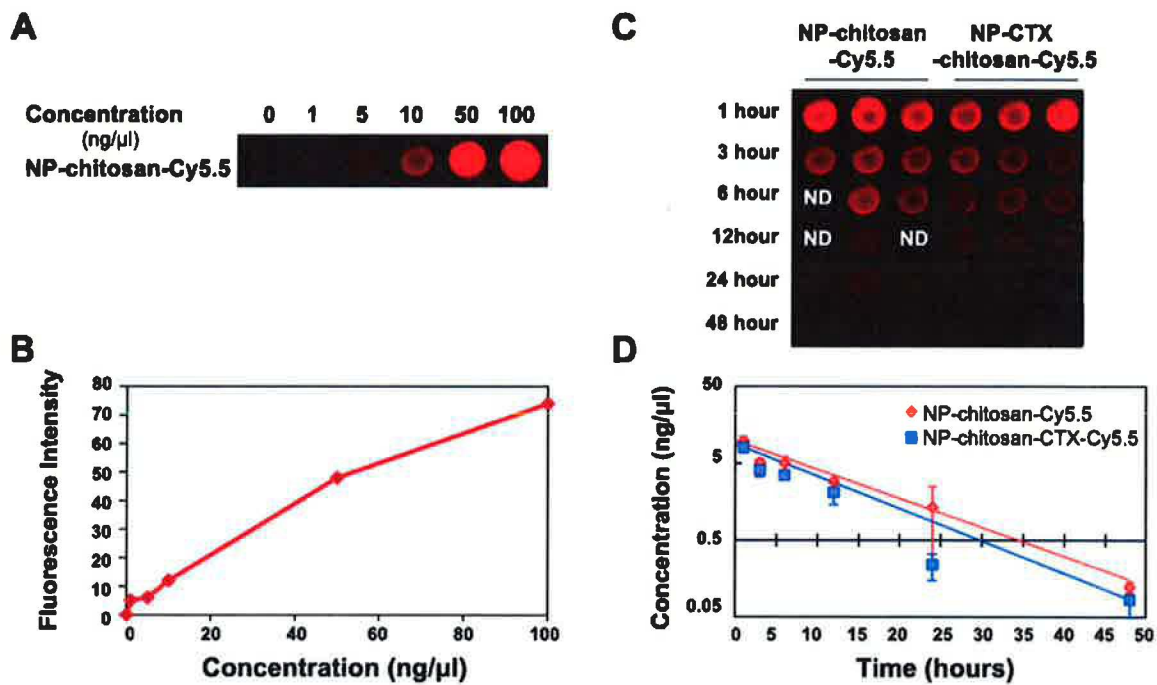


Figure 2.1 Serum half-life of nanoparticles.

(A and B) Standard curve generated by quantifying intensity of known concentrations of NP-chitosan-Cy5.5 or NP-CTX-chitosan-Cy5.5. (C and D) Measured fluorescence intensity of nanoparticles in serum. Each data point represents the mean fluorescence intensity integrated above the baseline. This baseline subtraction avoids systematic errors from underlying autofluorescence. Error bars represent standard errors of the mean. The curve indicates an exponential decay curve fit to the data ($n = 3$ mice per time point).

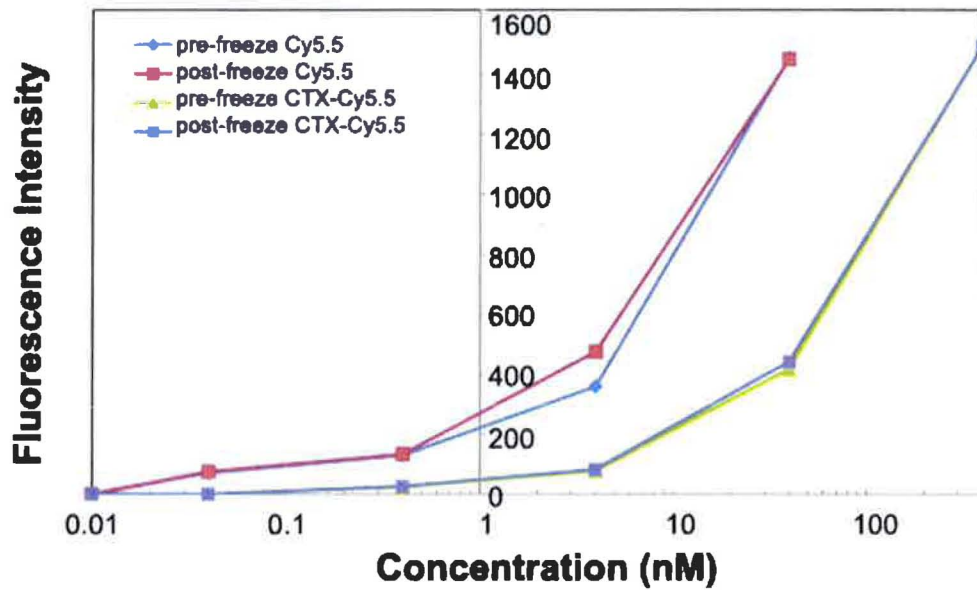


Figure 2.2 Freezing effects on NIRF signal

The stability of infrared signal during the process of freezing was addressed in a group of mice receiving free Cy5.5 dye and CTX-Cy5.5. Mice were injected via lateral tail vein with 100 μ l of either Cy5.5 or CTX-Cy5.5. 24 hours post-injection the animals were euthanized and the kidneys removed. One kidney was homogenized in 1 ml of PBS, 30 μ l was added to a 96 well plate and the NIRF signal was analyzed using the Odyssey imaging system before and after the freezing process.

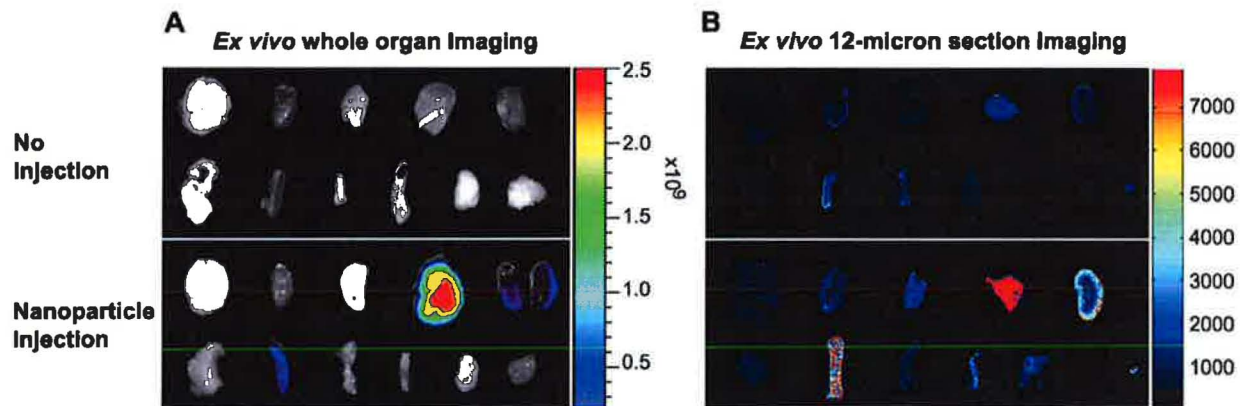


Figure 2.3 Ex vivo NIRF Imaging of each organ

Fluorescence image of whole organs in non-injected (top) or NP-CTX-Chitosan-Cy5.5 injected (bottom) animals. Images were acquired six hours post injection. (A) Mice were injected 200 μ l of 1 mg/ml. Six hours after injection, the animals were euthanized and the organs were collected. Ex vivo fluorescence images of whole organ was obtained using the Xenogen imaging system. The spectrum gradient bar corresponds to the fluorescence intensity unit p/sec/cm²/sr. (B) Fluorescence image of 12-micron sections obtained using the Odyssey imaging system. The spectrum gradient bar corresponds to relative fluorescent level. (Top row: brain, heart, lung, liver, and kidney. Bottom row: pancreas, spleen, small intestine, colon, gonad, muscle, and bone marrow) Bone marrow is only shown with the Odyssey scanner.

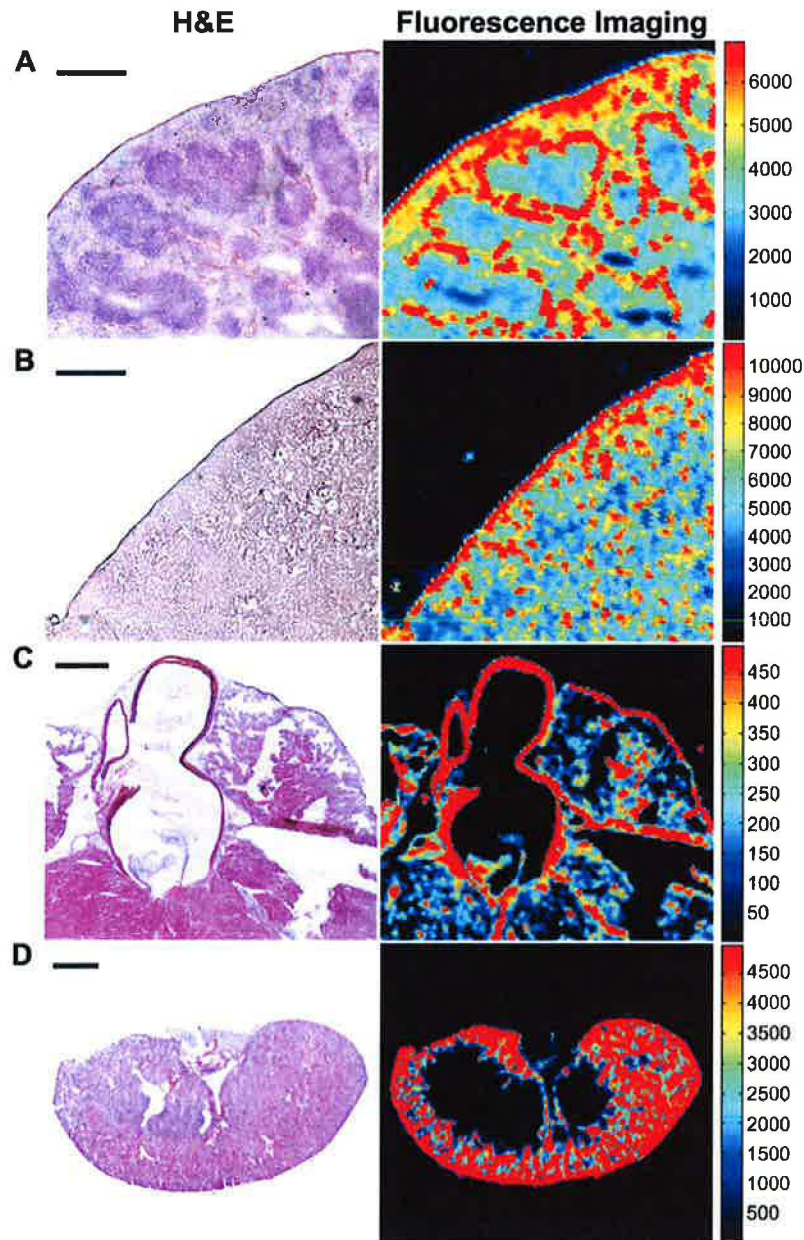


Figure 2.4 Comparison of H&E staining and high-resolution NIRF fluorescence imaging

(A) In spleen, NIRF signal was observed in large cells within the white pulp (bar, 500 μm). (B) In liver, the pattern was less obvious, but clearly heterogeneous (bar, 500 μm). (C) In heart, the muscle walls of the atria and ventricle showed no signal above background but the walls of the aorta showed significant signal (bar, 50 μm). (D) In kidney, high NIRF signal was found in the renal cortex (bar, 1 mm). All images were taken of tissues that were harvested 24 hours post nanoparticle injection.

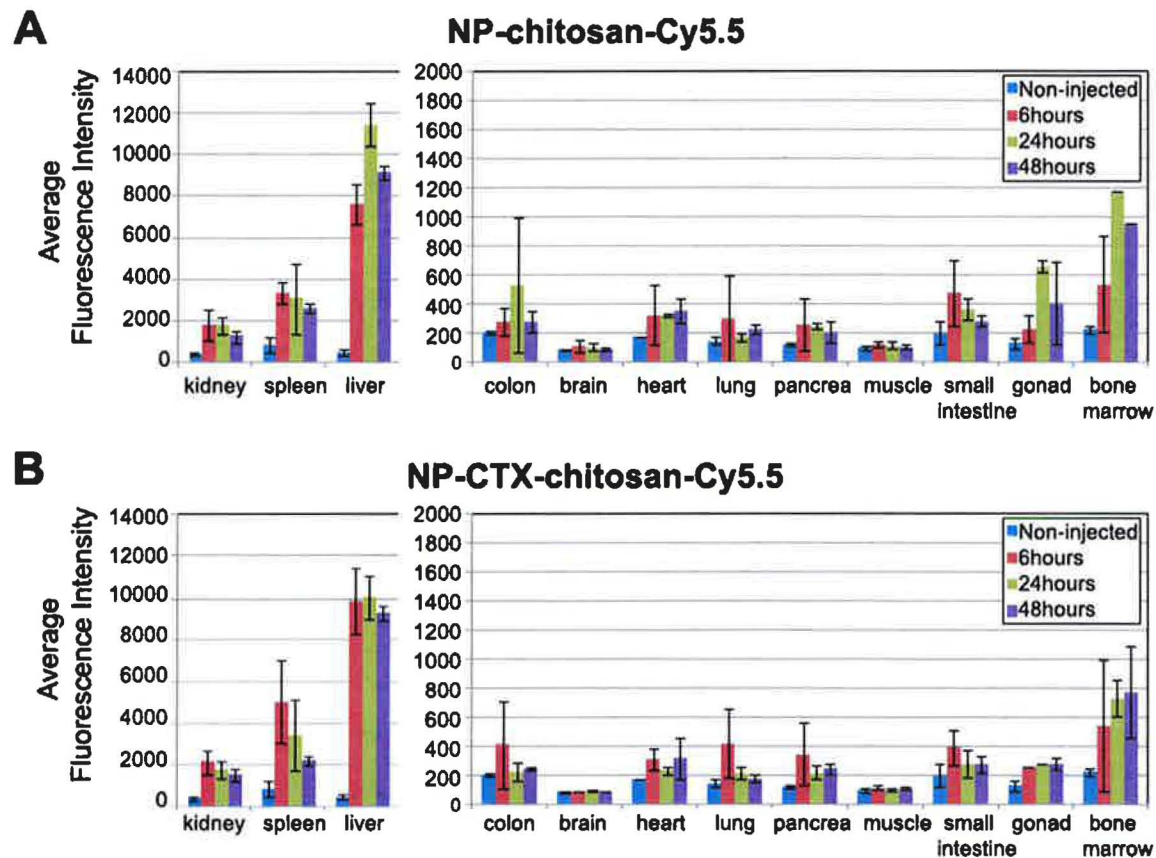


Figure 2.5 Biodistribution of NP-chitosan-Cy5.5 and NP-CTX-chitosan-Cy5.5 nanoparticles

Relative fluorescence intensity was determined using the Odyssey scanner. Bars represent tissue from animals that were not injected with nanoparticles (blue), or injected with nanoparticles and harvested 6 hours (red), 24 hours (green), or 48 hours (purple) after injection. Bars represent the average of 3 animals for each nanoparticle at each time point. The error bars are standard deviation from the mean. (A) Ex vivo biodistribution of NP-chitosan-Cy5.5 non-targeted nanoparticle. (B) Ex vivo biodistribution of NP-CTX-chitosan-Cy5.5 targeted nanoparticle.

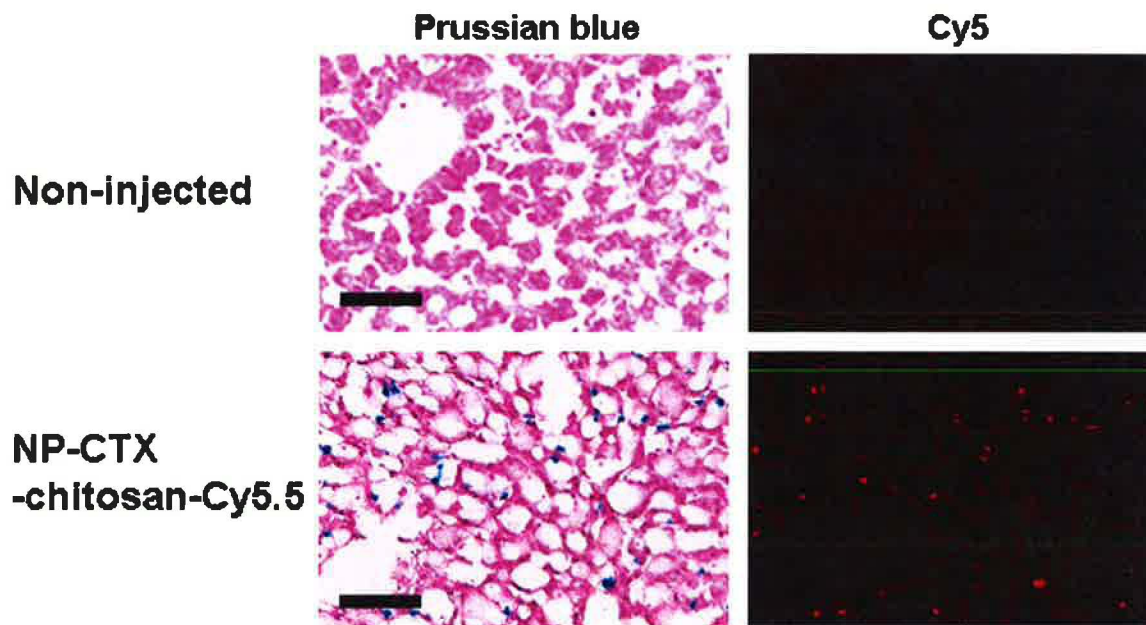


Figure 2.6 Co-localization of iron oxide nanoparticle core and Cy5 signal in liver

No iron uptake or Cy5 fluorescent signal was detected in non-injected control tissue (top row). Co-localization of Prussian blue/hemotoxylin staining and Cy5 signal from the same tissue section suggest that the nanoparticles remain stable in vivo (bottom row) (bar, 50 μm).

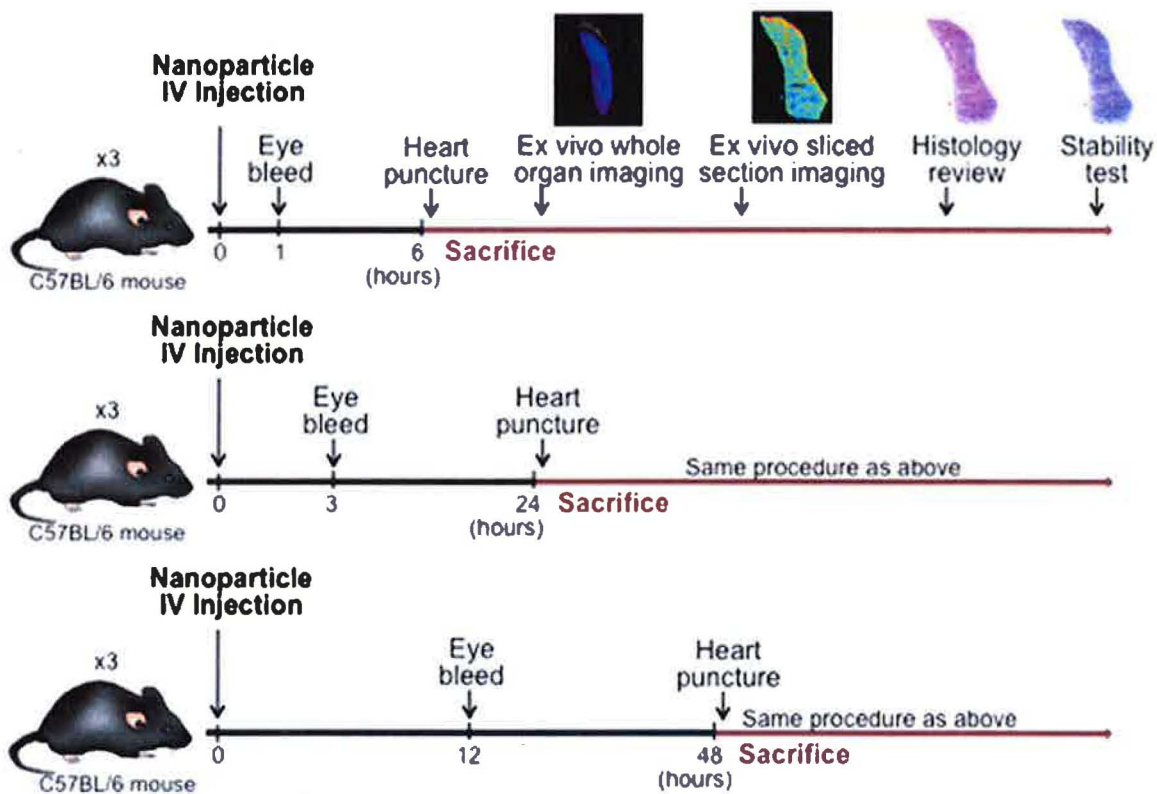


Figure 2.7 Rapid and easy method to generate key pharmacokinetic data

Our approach minimizes the number of mice required to evaluate nanoparticle pharmacokinetic properties. Serum half-life, whole organ biodistribution, biodistribution at cellular level up to 12 μm resolution, histological and in vivo stability analysis can be performed from the same set of mice that are used to assess nanoparticle targeting to cancer cells or other targets.

CHAPTER 3

Drug resistance mechanisms in mouse medulloblastoma model

Modified from an article published in PNAS:

Lee, M.J., Hatton, B.A., Villavicencio, E.H., Khanna, P.C., Friedman, S.D., Ditzler, S., Pullar, B., Robison, K., White, K.F., Tunkey, C., *et al.* (2012). Hedgehog pathway inhibitor saridegib (IPI-926) increases lifespan in a mouse medulloblastoma model. *Proc Natl Acad Sci U S A* 109, 7859-7864.

Summary

The Sonic Hedgehog (Shh) pathway drives a subset of medulloblastomas, a malignant neuroectodermal brain cancer, and other cancers. Small molecule Shh pathway inhibitors have induced tumor regression in mice and patients with medulloblastoma; however, drug resistance rapidly emerges, in some cases via *de novo* mutation of the drug target. Here we assess the response and resistance mechanisms to the natural product derivative, saridegib, in an aggressive Shh-driven mouse medulloblastoma model. In this model, saridegib treatment induced tumor reduction and significantly prolonged survival. Furthermore, the effect of saridegib on tumor initiating capacity was demonstrated by reduced tumor incidence, slower growth and spontaneous tumor regression that occurred in allografts generated from previously treated autochthonous medulloblastomas compared to those from untreated donors. Saridegib, a known P-glycoprotein (Pgp) substrate, induced Pgp activity in treated tumors and this likely contributed to emergence of drug resistance. Unlike other Smoothed (Smo) inhibitors, the drug resistance was not mutation-dependent nor Gli2 amplification-dependent and saridegib was found to be active in cells with D473H point mutation that rendered them resistant to another Smo inhibitor, GDC-0449. The five-fold increase in lifespan in mice treated with saridegib as a single agent compares favorably with both targeted and cytotoxic therapies. The absence of genetic mutations that confer resistance distinguishes saridegib from other Smo inhibitors.

Introduction

Medulloblastoma is the most common malignant brain cancer in children. While long term survival for standard- and high- risk medulloblastoma patients is now greater than 70% and 50% respectively, this comes at a significant cost of toxicity due to surgery, radiation, and chemotherapy (Rossi et al., 2008). Shh pathway activation represents about 20-25% of all medulloblastoma cases. Shh pathway activation also drives several other types of cancer through cell autonomous oncogenic mechanisms or induction of micro-environment properties that provide a growth advantage to tumor cells

(Katoh and Katoh, 2009). Therefore, pathway inhibitors are being actively investigated for Shh-driven cancers.

Current therapeutic candidates primarily target the Smoothed (Smo) protein. In normal Shh signaling, Smo is released from inhibition by the Patched (Ptch) receptor by surface binding of Shh. Smo then activates downstream Shh targets such as the Gli transcription factors. HhAntag, the first synthetic small molecule Smo antagonist reported, induces resolution of autochthonous brain tumors and flank medulloblastoma xenografts in the *Ptch1^{+/-}; p53^{-/-}* mouse model (Romer et al., 2004). Newer generation synthetic small molecules targeting Smo protein are now being used in patients. GDC-0449 was reported to induce significant reduction in tumor burden in an adult Shh-driven medulloblastoma patient (Yauch et al., 2009). While these were important first steps toward effectively targeting the Shh pathway in cancer, responses were pronounced yet short-lived due to the emergence of drug resistance (Metcalf and de Sauvage, 2011; Rudin et al., 2009; Yauch et al., 2009). It remains to be determined whether these drugs confer a survival benefit to medulloblastoma patients. The identification of Smo inhibitors that remain active against cells that develop resistance to other agents in this class could benefit patients, particularly if acquired resistance is limited or slower to develop.

Saridegib is a novel, selective and potent small molecule that targets the Shh pathway by inhibiting Smo. Saridegib is orally bioavailable and has demonstrated biological activity in multiple preclinical animal models of cancer (Metcalf and de Sauvage, 2011). In this study we assessed saridegib activity in a very aggressive mouse medulloblastoma model, the conditional *Patched1*-null (hereafter referred to as *Ptc^{C/C}*), that lacks both alleles of *Patched1* (*Ptch1*) specifically in cerebellar granule neuron precursors (Yang et al., 2008). The *Ptc^{C/C}* model is notable for massive hyperproliferation of granule cells throughout the cerebellum and the evolution of highly aggressive tumors that are clinically evident as early as P21 and induce death within weeks after mice become symptomatic.

With few exceptions, targeted therapies have been disappointing in human clinical trials, largely due to rapid emergence of resistance mutations. In this study, we evaluated the efficacy of saridegib in a highly aggressive medulloblastoma model and evaluated drug resistance with particular attention to cell autonomous point mutations or amplifications that confer resistance to other agents. Here, we showed that drug resistance observed following extended treatment periods is primarily due to increased expression and activity of P-glycoprotein (Pgp) drug transporter rather than the emergence of genetic mutations that prevent drug-target interactions.

Results

Saridegib induces clinical remission and extends survival

We performed a pilot study to evaluate the efficacy of saridegib in 21-day old *Ptc^{C/C}* mice with clinical evidence of medulloblastoma. Mice were randomized to receive either daily intraperitoneal (IP) saridegib (20 mg/kg/dose, n=3) or vehicle (n=2) for 19 days. Full resolution of clinical symptoms was evident by 19 days of treatment (Figure 3.1A). In contrast, vehicle treated mice showed progressive tumor growth. Analysis of gross tumor pathology following treatment demonstrated a strong response to saridegib therapy, with decreased cerebellar tumor size in treated mice (Figure 3.1B). Imaging with Tumor Paint (Ctx:Cy5.5), a tumor-tracking molecular bioconjugate (Veisoh et al., 2007), exhibited a reduction in tumor burden in saridegib treated mice (Figure 3.1C) and histopathological analysis of cerebellar tumor sections also revealed a decrease in tumor burden (Figure 3.1D). The foliation pattern in the cerebellum was completely obliterated in vehicle treated tumors, whereas saridegib treated animals manifested regions of tumor cell death, as indicated by pyknotic nuclei with retention of normal cerebellar architecture.

Given these promising results, we performed a larger scale study and extended the duration of therapy. Study animals received 6 weeks of daily saridegib (n=26) versus vehicle control (n=11). Three- to five-week-old mice with tumors were randomized to receive daily saridegib (20 mg/kg/dose) or vehicle. Kaplan-Meier analysis demonstrated that all mice treated with daily saridegib for 6 weeks (red line) survived, while all vehicle-treated (blue line) mice developed ataxia and neurologic deficits and eventually succumbed to their disease ($P < 0.001$; Figure 3.2). Clinical symptoms were resolved in many of the saridegib treated mice, accompanied by restored neurologic function and increased activity. The profound difference between 100% survival and neurologic recovery in saridegib -treated mice compared to 100% death in vehicle-treated mice prompted in depth analyses of tumor response.

Magnetic resonance imaging (MRI) detects sub-clinical disease progression

Using a technique that preserved intracerebral architecture, histological findings were compared to MRI findings in mice that were sacrificed within days of an MRI (Figure 3.3). Histopathological evaluation of tumor treated with saridegib for 6 weeks showed reduced tumor volume and a moderate reduction in tumor cell density. Extending these findings noninvasively, MRI analyses at 3 week intervals showed that saridegib treatment induced substantial tumor regression after three weeks of daily administration (Figure 3.4). Hydrocephalus, enlarged ventricles, (yellow arrow) and trans-ependymal cerebral spinal fluid (CSF) flow (red arrow) were commonly noted in vehicle-treated mice and were minimal in drug-treated mice (Figure 3.4A and Figure 3.5). Mice treated with saridegib showed a reduction of Ki67-positive cells in tumor after 4 days of treatment (Figure 3.6), indicating an arrest of cell proliferation. Nevertheless, approximately half of the mice treated with saridegib (20 mg/kg/day)

exhibited a rebound in tumor growth by 6 weeks following maximal size reduction at 3 weeks (Figure 3.4B-C).

The MR images were also used to calculate tumor volumes (see Figure 3.3 for representative images of 3D-rendered tumor volumes generated from serial MR images). This analysis confirmed the significant reduction in tumor volume by 3 weeks of saridegib treatment (average tumor volume at enrollment = 1108 mm³; average tumor volume after 3 weeks of daily saridegib = 580 mm³; $P=0.0005$), but also showed that not all tumors continued regressing as treatment continued (average tumor volume after 6 weeks of daily saridegib = 848 mm³; $P=0.05$). In contrast, all tumors in vehicle-treated mice continued progressing, with average tumor volumes increasing from 1082 mm³ at enrollment to 1408 mm³ at the 3 week time point. MRI volumetrics were additionally validated by 3D tumor volume rendering of serial H&E stained tissue sections from a cohort of mice analyzed by MRI (Figure 3.3). The MRI and histological findings prompted two sets of experiments, one to assess the impact of maintenance treatment regimens on survival and the other to establish the mechanism(s) underlying disease progression during treatment.

Maintenance saridegib administration prolongs survival

To further establish the extent to which saridegib can prolong survival, we assessed maintenance dosing regimens. Mice were given daily saridegib (20 mg/kg/dose) for six weeks (n=24), and then either taken off drug (n=12) or given maintenance dosing (20 mg/kg twice per week) for six additional weeks (n=12). Tumors progressed rapidly after the withdrawal of drug following the initial six weeks of daily treatment (light purple), resulting in death within an average of 10 days (Figure 3.7A). In contrast, 46% of mice receiving maintenance dosing (purple) were still alive six weeks after starting twice-a-week therapy. Thus, continued saridegib treatment following six weeks of daily therapy prolonged median survival five-fold compared to vehicle treated control animals. Having established tumor regression, neurologic improvement and a survival advantage conferred to $Ptc^{C/C}$ mice, we next sought to determine whether tumor initiating capacity, which is important for metastases generation, was impaired by drug treatment.

Saridegib reduces medulloblastoma tumor initiating capacity

Medulloblastoma cells from the $Ptc^{C/C}$ mice have tumor initiating potential, as evidenced by their ability to form new tumors when transplanted to wild type recipient mice. Tumors were established from 9 of 11 drug-naïve donors and 43% (54 out of 127) of recipients grew flank tumors. In contrast, the same approach yielded tumors in only 23% (18 out of 78) of recipients when donors were treated with daily saridegib for 6 weeks (20 mg/kg) prior to transplantation (Figure 3.7B). This demonstrated that saridegib

reduced tumor initiating potential in this aggressive medulloblastoma mouse model when transplanted in flank ($P=0.017$). Interestingly, the tumor growth rate in saridegib treated donor allografts differed from that of the drug naïve donor group. Flank allografts established from the drug treated donor group grew much more slowly and often stopped growing. One out of six tumors showed spontaneous tumor regression in the absence of drug after initial growth to 895mm³.

Saridegib induces regression of flank allografts from drug refractory donors

To explore whether the resistance was through cell-autonomous mechanisms, we used the allograft models to investigate the effect of saridegib treatment on tumor size. When the flank allograft tumor volumes reached 1000 mm³, recipient mice received either daily saridegib (20 mg/kg) or vehicle treatment and the growth of flank allografts was monitored over a nine-week period. Daily IP administration of saridegib into recipient mice suppressed tumor growth to the point that tumors were undetectable in 100% of both allograft groups (Figure 3.7C). We attribute the response of flank tumors derived from the saridegib -treated donor mouse to higher drug concentrations in the flank tumors compared to brain tumors, the latter of which are protected by the blood brain barrier. Consistent with this, saridegib concentrations were approximately 10-15 fold higher in flank tumors than in cerebellar tumors at the same dosing regimen (Table 3.1). Interestingly, the markedly higher drug concentrations achieved in flank tumors were sufficient to overcome the drug tolerance observed in the cerebellar tumor of the donor mouse. However, the higher concentration alone was not sufficient to sustain remission in mice that received flank allografts from drug-naïve donors. Two of five tumors progressed while on therapy during the 9-week trial despite initially disappearing in response to saridegib administration.

Escape from Shh inhibition accompanies tumor progression in saridegib treated mice

To better understand drug engagement with Shh pathway activity after prolonged treatment, we assessed the level of *Gli1* inhibition by saridegib at the end of 6 weeks of daily therapy. Reduced suppression of Shh signaling at the end of therapy would indicate the emergence of saridegib-resistant cells. This possibility was supported by the observation that saridegib suppressed *Gli1* levels by 83% after 4 days of daily treatment, by 52% after 2 weeks of therapy and by 29% after 6 weeks of therapy, respectively, compared to that of vehicle treated control tumors (Figure 3.8A). The blood brain barrier has been shown to limit drug penetration into the brain over time through induction of drug efflux pumps (Loscher and Potschka, 2005). This was not the case in our study, as saridegib concentrations increased in cerebellar tumors over time (Table 3.1).

Pgp-mediated efflux transport

One of the main mechanisms of drug resistance in cancer cells is aberrant expression of ATP-binding cassette (ABC) transporters, which utilize active transport to efflux drugs from treated cells. Many chemotherapeutic drugs and Shh inhibitors are substrates of the ABC transporter Pgp. To determine whether Pgp was up-regulated in response to saridegib therapy, we quantified Pgp transporter expression via Western blotting in samples from vehicle treated and saridegib treated mice. The expression levels of Pgp in tumor homogenates were significantly increased by daily treatment with saridegib for six weeks (Figure 3.8B). We compared the function of Pgp in untreated and saridegib-treated medulloblastomas using calcein-AM, a fluorescent Pgp substrate that quantitatively measures Pgp activity. Intracellular accumulation of calcein in untreated and saridegib treated mice was measured by flow cytometry. 79.5% of vehicle treated tumor cells incorporated calcein as compared with only 38.6% of accumulation in saridegib treated *Ptc^{C/C}* tumors (Figure 3.8D). The experiment was repeated in the presence of the Pgp inhibitor, verapamil. Increase in the intracellular level of fluorescence after exposure to verapamil indicates the presence of Pgp transporters in saridegib treated *Ptc^{C/C}* (Figure 3.8C).

To determine whether Pgp inhibition influenced the affect of saridegib on Gli1 expression, we measured Gli1 levels in the presence of the Pgp inhibitor, verapamil, and saridegib. Indeed, inhibition of Pgp transporter via verapamil treatment reversed drug resistance, suggested by decreased *Gli1* levels within tumors receiving the combined therapy (Figure 3.8A).

Lack of resistance-inducing mutations or Gli amplification

Previous studies revealed that Smo activating or drug resistance point mutations occur in the sixth (TM6) or seventh (TM7) transmembrane domains (Taipale et al., 2000; Yauch et al., 2009). In contrast, tumors that grew despite ongoing saridegib therapy showed no evidence of mutations in TM6 or TM7. Of the 8 brain and 3 flank tumors from which the *Smoothened* gene was sequenced, only one showed sequence variations that could not be readily attributed to known inter-strain single nucleotide polymorphisms. This point mutation at Asparagine 223 is not within any of the seven transmembrane domains of the Smo protein and does not map to a region of the protein with a known functional domain. We conclude that it is unlikely that the re-growth of both intracranial and flank allografted medulloblastomas is dependent on *de novo Smoothened* mutations.

A recent report showed that point mutations were found only infrequently in tumors that developed resistance to the Smo inhibitor, NVP-LDE225, but Gli2 amplifications were observed in 50% of resistant tumors (Buonamici et al., 2010). PCR analyses of genomic DNA from 8 saridegib resistant brain tumors revealed no Gli2 amplification. Thus, the cell autonomous genetic events that lead to resistance to GDC-0449 and NVP-LDE225 were not present in saridegib-treated medulloblastoma tumors, indicating that this cycloamine derivative interacts with the target protein in a manner distinct

from the synthetic Shh inhibitors. Furthermore, comparative genomic hybridization (aCGH) showed no focal gains or losses across the entire genome of saridegib-treated tumors compared to normal.

Expression profiling of saridegib treated tumor showed minor changes in Shh pathway signatures

We used Illumina microarray to validate mRNA expression signature of vehicle and saridegib treated tumors. We identified several networks/pathways that were statistically significantly enriched, including those involved in cancer, neurological disease, cell death, and cellular movement using Ingenuity Pathway Analysis (Table 3.2). Top most differentially expressed genes are listed in Table 3.3. We examined the level of 11 gene SHH subgroup signatures: butyrylcholinesterase (BCHE); GLI1; GLI2; inter- α -trypsin inhibitor heavy chain H2 (ITIH2); microtubule-associated monooxygenase, calponin and LIM domain containing 1 (MICAL1); PDZ and LIM domain 3 (PDLIM3); PTCH2; RAB33A; secreted frizzled-related protein 1 (SFRP1); orthodenticle homeobox 2 (OTX2); and neurogenin 1 (NEUROG1). Recurrent tumors showed characteristics of Shh subgroup similar to vehicle treated group (Figure 3.9). Among those genes, secreted frizzled-related protein 1 (SFRP1) and Orthodenticle homeobox 2 (OTX2) showed statistically significant differential expression in drug treated group compared to that of vehicle treated group.

Saridegib activity on D473H SMO mutant

Saridegib was assayed alongside other Smo inhibitors in the C3H10 differentiation assay as previously described (Tremblay et al., 2009). Saridegib and inhibitors GDC-0449, LDE-225 and SANT-1 all have activity in the 7-30 nM EC₅₀ range. Cyclopamine is less potent with an EC₅₀ range of 500 nM-1mM. To determine the ability of saridegib to suppress Shh signaling in the context of the D473H SMOOTHENED (*SMO*) mutant known to confer resistance to the Shh pathway antagonist GDC-0449 (Yauch et al., 2009), we measured the half maximal concentration (IC₅₀) of saridegib required to inhibit Gli-luciferase activity (Figure 3.7D). Saridegib inhibited reporter activity at an IC₅₀ of 9nM in C3H10T1/2 cells transfected with wild type *SMO* and also showed activity against the D473H *SMO* mutant at an IC₅₀ of 244nM. Saridegib induced greater than 95% inhibition at 1 μ M concentration in D473H *SMO* mutant cells, which compares favorably with GDC-0449 (3% inhibition at 1 μ M concentration), cyclopamine (the parent drug from which saridegib is derived, 48% inhibition at 1 μ M concentration) and other drugs screened for activity against this mutation (Dijkgraaf et al., 2010). These findings are in contrast to results obtained with other hedgehog pathway antagonists and suggest that saridegib retains the ability to impair downstream hedgehog signaling even in the presence of some activating *SMO* mutations.

Discussion

Medulloblastoma is an aggressive malignant brain cancer that is particularly difficult to cure in the recurrent disease setting. Conventional therapies for medulloblastoma impose unacceptable toxicities on children with this disease and more effective, less toxic alternatives are critical for future care. Smo inhibitors show promise for targeting Shh-driven tumors, but resistance emerges rapidly (Dijkgraaf et al., 2011; Rudin et al., 2009; Yauch et al., 2009). Because this pathway is considered crucial for several cancer types, efforts are underway to advance drugs that are less prone to resistance induction.

In this study, six weeks of daily saridegib resulted in 100% survival compared to 0% in the vehicle-treated medulloblastoma-bearing mice. Additionally, a substantial resolution in clinical symptoms was observed in the majority of saridegib treated mice, secondary to reduced hydrocephalus, calvarial swelling and accompanied by increased mouse activity. Treatment with saridegib sharply reduced tumor allograft engraftment success and some allografts established from saridegib donors underwent spontaneous regression after initial significant growth. Both observations are consistent with the notion that Smo inhibitors limit medulloblastoma tumor initiating capacity.

This is the first study to examine hedgehog pathway antagonism in the conditional *Ptc^{C/C}* mice. A previous study demonstrated the efficacy of the HhAntag hedgehog antagonist in a less aggressive *Ptch1^{+/-}; p53^{-/-}* model of medulloblastoma arising in the *Ptch1* heterozygous, *p53* null background (Romer et al., 2004). While these results share similarities to our current study, an important contrast must be noted in the extent of tumor burden in response to heterozygous versus homozygous loss of *Patched1* within the cerebellum. In the *Ptc^{C/C}* model, all cerebellar granule neuron precursor cells are lacking the inhibition normally mediated by the Patched1 receptor, and tumor formation is early, aggressive and uniform throughout the cerebellum. Thus, the response to saridegib was remarkable given the continuous source of neoplastic cells and the extent of initial tumor burden in intracranial *Ptc^{C/C}* tumors.

The heptahelical structure of the Smo receptor is required for binding of cyclopamine and is targeted by G protein coupled receptor modulators (Chen et al., 2002) and mutations near the highly conserved transmembrane domains can reduce the affinity of compounds specifically targeted to this binding pocket. In contrast to the previous report of mutation-based resistance to GDC-0449, we did not observe mutations in the TM6 or TM7 domains of the *Smo* allele, nor did we observe *Gli2* amplification.

Gene expression profiling suggests minor alteration of two Shh signature genes in the saridegib-treated group. We found downregulation of SFRP1 genes and up-regulation of OTX2. Previously, SFRP1 has been identified as a prime biomarker for the Shh subgroup (Northcott et al., 2011), and a high expression level of SFRP1 was found in *Ptch1^{+/-}* tumors (Pei et al., 2012). The expression of OTX2 is low or absent in Shh-driven human medulloblastoma (Di et al., 2005; Adamson et al., 2010). OTX2 copy number gain has been associated with more aggressive tumor phenotypes and decreased patient survival

(Adamson et al., 2010), and inhibition of OTX2 in medulloblastoma cell lines decreased tumor proliferation and formation in vitro (Bunt et al., 2010). Although OTX2 is an essential gene in Shh-independent medulloblastoma, little is known about its role in Shh-dependent medulloblastoma and its mechanism by which OTX2 regulates the expression of its target genes. Given that OTX2 is upregulated in saridegib resistant tumor, it will be important to perform detailed molecular studies of oncogenic pathways driven by OTX2. These studies will aid the development of new therapeutic strategies for Shh-independent medulloblastoma patients as well as Shh-dependent patients who develop resistance against Smo therapy.

The absence of genetic mutations in *Smo* or amplifications of *Gli2* raise the question of why tumors eventually grow in mice treated with saridegib. It is possible that this is a reflection of the highly aggressive model, in which most cells in the granule cell lineage completely lack negative regulation of the mitogenic Shh pathway. Alternatively, saridegib activity could be affected by common drug resistance mechanisms such as ABC transporters. Indeed, we saw increased Pgp expression in the brain tumors of mice treated for 6 weeks with saridegib (Figure 3.8). Furthermore, co-administration of verapamil, a Pgp inhibitor, partially restored the capacity of saridegib to reduce *Gli1* even after extended (6 week) treatment periods. A Pgp functional assay with calcein-AM revealed increased level of efflux activity in saridegib treated *Ptc^{CC}*. The relationship between Pgp and saridegib activity is somewhat confusing because the binding site of cycloamine, and presumably the cycloamine derivative saridegib, lies on a portion of Smo that is internal to the plasma membrane. In addition, it is not clear whether the drug accesses the binding site from the cytoplasmic side or the surface of the plasma membrane.

Unlike studies of other oncology drugs, including cytotoxic chemotherapy agents, our results are unique because they show a fivefold increase in survival in mice with advanced, aggressive, autochthonous brain tumors. Our nonclinical studies clearly demonstrate the efficacy of saridegib in resolving clinical symptoms of advanced medulloblastoma and prolonging survival in the *Ptc^{CC}* model.

Materials and Methods

Mouse Models and Drug Dosing

Animal experiments were conducted in accordance with the NIH and Institutional guidelines. Conditional *Patched1* null mice (*Ptc^{CC}*) were generated by breeding mice homozygous for the floxed *Ptch1* allele (Adolphe et al., 2006) to *Math1-Cre* mice (Yang et al., 2008). For allograft studies, medulloblastomas from symptomatic *Ptc^{CC}* mice were harvested, triturated, filtered, and resuspended in equal parts of DMEM and Matrigel (BD Biosciences). 1×10^6 cells were injected subcutaneously into the flank of wild type littermates. Tumor volume was calculated from caliper measurements ($0.5 \times \text{length} \times$

width²). Postnatal day (P) 21 to P36 *Ptc*^{C/C} mice were randomized to receive either saridegib (Infinity Pharmaceuticals; 20mg/kg/dose) or vehicle control (5% (2-Hydroxypropyl)- β -Cyclodextrin (HPBCD), Sigma-Aldrich) administered via daily intraperitoneal (IP) injection. Saridegib drug levels in tumor and brain samples were determined as previously described (Olive et al., 2009). For combination therapy, ABC transporter inhibitor verapamil (Sigma-Aldrich; 15mg/kg/dose) was administered weekly via oral gavage between third and sixth week.

Tumor Pathology

We preserved tissue while maintaining the spatial integrity of the brain and ventricular spaces within the skull. Whole brains within the skull were fixed in 10% formalin, decalcified using Formical 4 (Decal Chemical) and embedded in paraffin. Tissues were cut into 4 μ m sections in the horizontal plane and H&E stained to generate computerized three-dimensional (3D) renderings of the tumors. Sections were scanned using a TissueFax microscope (TissueGnostics), stacked and aligned using the StackReg function of ImageJ and 3D models rendered using Imaris.

Magnetic Resonance Imaging and Chlorotoxin: Cy5.5 (Ctx: Cy5.5) Imaging Analysis

Magnetic resonance imaging (MRI) was performed using a 3 Tesla MRI system (Philips Achieva) and a custom mouse head coil. Serial MR scans were performed under halothane anesthesia using a 35 minute coronal high-resolution T2-weighted sequence (TE=110ms, TR=2000ms, bandwidth=212, 2 NEX or signal averages, pixels in-plane=256x256, slice thickness=320 μ m, interslice gap=160 μ m). DICOM images were exported from the MRI scanner to a web-based repository (BioScribe) and then imported into ITK-SNAP (www.itksnap.org). Ctx: Cy5.5 *in vivo* imaging was carried out as previously described (Veiseh et al., 2007).

Gene Expression Analysis

Total RNA was extracted (RNeasy Plus Kit, Qiagen) and converted to cDNA (Taqman Reverse Transcription kit, ABI). Quantitative RT-PCR was performed using Taqman Master Mix and the 7300HT System (ABI) using Taqman primers for mouse *Gli1* and *Gapdh* and SDS2.3 software (ABI). All conditions were run in triplicate and normalized to mouse *Gapdh* controls.

For whole-genome expression analysis, RNA was hybridized to mouse-specific (MouseWG-6 v2.0) expression BeadChips (Illumina). Probe intensities were normalized with the Illumina specific Lumi Bioconductor R package. Functional gene-interaction network analysis was performed by using Ingenuity Pathways Analysis (Ingenuity Systems).

Gene Amplification Analysis

Gli2 amplification was assessed by Real Time PCR using SYBR green PCR kit (Qiagen). Tumors were snap frozen and analyzed for Gli2 using three different primer sets and for GAPDH as normalization control. Genomic DNA from 4 mice of different genomic backgrounds was used as controls for each assay along with a no template control. Four technical replicates were performed.

Western Analysis

Tumor samples were homogenized in RIPA lysis buffer, which included protease inhibitors. Equal amounts of proteins were loaded onto 4-12% SDS-PAGE gel, transferred onto PVDF membrane, and probed with the antibody of interest: Pgp (C219; 1:100; Covance).

Immunohistochemical Staining

Tissues were cut into 4- μ m sections and immunostained with the following antibodies: anti-Ki67 (1:1,000; Novocastra) and anti-Cleaved Caspase 3 (1:50; Biocare Medical). Sections were scanned with a TissueFax microscope (TissueGnostics). For Ki67 and Cleaved-Caspase 3 staining quantification, positive staining was quantified with National Institutes of Health image analysis software, Image J, and reported as percentage area of staining in the cerebellum.

DNA Sequencing Analysis

Frozen tumor samples were lysed in a Geno/Grinder 2000 (SPEX CertiPrep) followed by DNA isolation using a QIAamp DNA mini kit (Qiagen). Samples were quantitated with a Nanodrop 2000c (Thermo). PCR primers were tagged with M13F forward (TGTAACGACGGCCAGT) or M13 reverse (CAGGAAACAGCTATGAC). Information on primer sequences for SMO exons 1-12 is provided in Table 3.4. PCRs were run on a Dyad DNA Engine (MJ Research/Bio-Rad) using the following conditions: 95°C 5 min followed by 35 cycles of 95°C 30 s, 60°C 30s, 68°C 45 s, followed by 68°C 10 min. Target sequence was sequenced by the Sanger method (Gene Wiz) in both forward and reverse directions.

Gli-Luciferase Reporter Assay

Gli-Luciferase reporter assays were performed as described (Yauch et al., 2009)

Gene Expression Analyses

Purified total RNA was hybridized to mouse-specific (WG-6 v2) expression beadchips (Illumina). Probe intensities were normalized by the Illumina specific Lumi Bioconductor R package. Functional

gene interaction network analysis was performed using Ingenuity Pathways Analysis (Ingenuity Systems).

Array Comparative Genomic Hybridization

Genomic DNA was labeled and hybridized to Mouse Genome 244K array-CGH (Agilent Technologies) using WT littermate genomic DNA as a reference. Arrays were scanned with an Agilent microarray scanner and image analysis was performed using Agilent Feature Extraction software.

Pgp Functional Assay by Flow Cytometry

Pgp functionality was assessed by measuring fluorescent dye efflux of calcein-AM (Molecular Probes) with or without Pgp inhibitor, verapamil. 5×10^5 cerebellar Ptc^{C/C} tumor cells were incubated with or without 10 μ M verapamil for 1hr at 37°C. Then cells were incubated with non-fluorescent 1 μ M Calcein-AM for another 30 min at 37°C. Cells were washed and resuspended in cold PBS and analyzed for calcein fluorescence by flow cytometry (Excitation: 495nm; emission: 515nm). Debris was eliminated by gating on forward versus side scatter. The function of Pgp is expressed as the mean percentage of fluorescence intensity of gated FITC positive cells. The assays were performed in triplicate.

Statistical Considerations

Studies were designed to detect differences in event rates that approximately corresponded to a doubling of median improvement in survival of (3 weeks) with 90% power based on simulated power experiments. These estimates were made using two-sided log-rank test at P<0.05 significance level. Survival analyses used animal death times and censoring times when animals were sacrificed at approximately 6 weeks or as otherwise stated. Survival curves were plotted using Kaplan-Meier method and compared using two-sided log-rank test. The Bonferroni test was used to correct multiple comparisons. Statistical analyses were performed in R statistical systems (<http://www.r-project.org>).

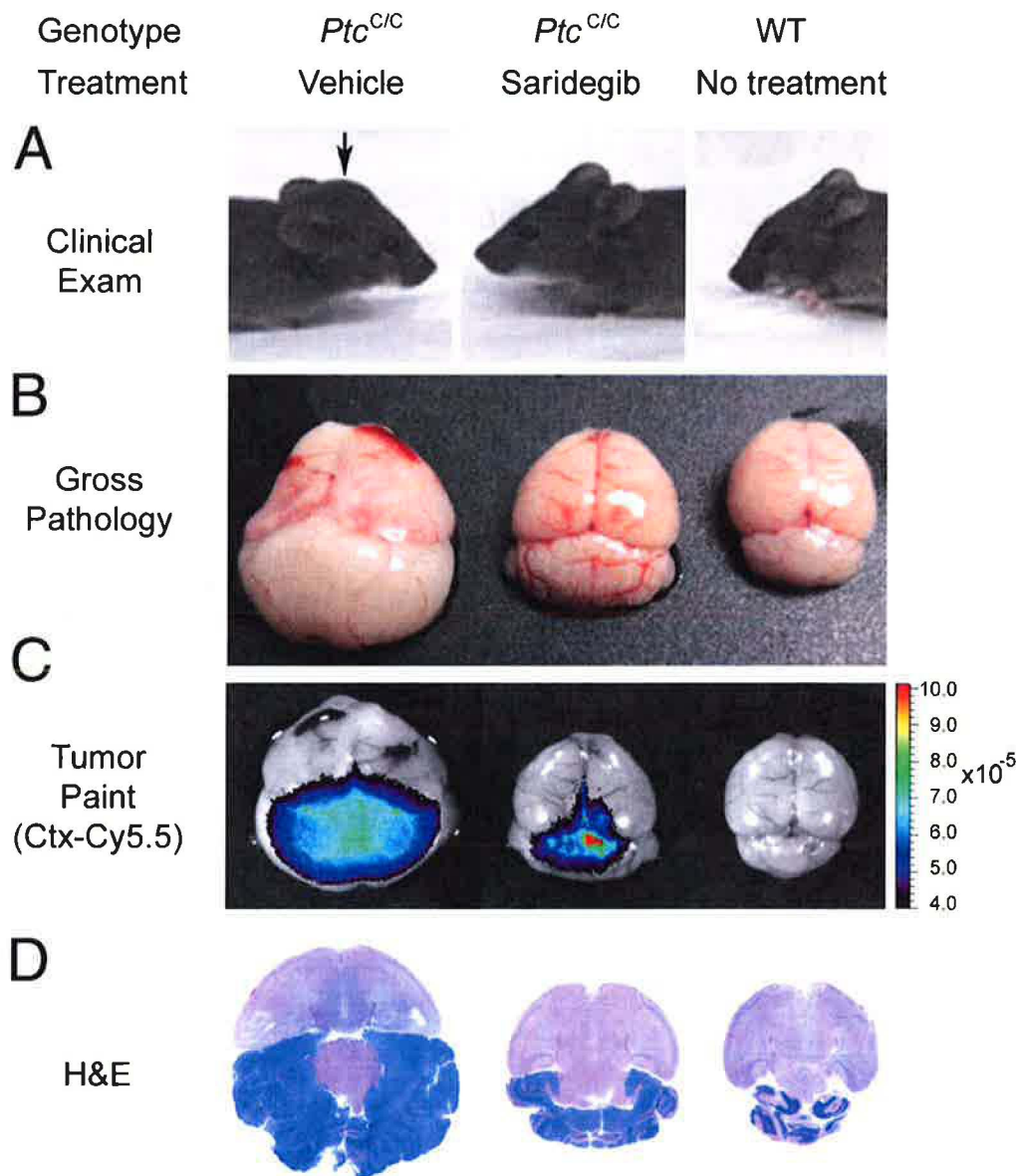


Figure 3.1 The Smo inhibitor saridegib causes regression of mouse medulloblastoma

Three-week old mice symptomatic for medulloblastoma were randomized to receive daily intraperitoneal saridegib (20 mg/kg/dose, n=3) or vehicle (n=2) for 19 days. (A) Compared to a representative vehicle-treated mouse with a large tumor (left panels) and a wild-type littermate with no tumor (right panels), a representative mouse treated with saridegib (center panels) showed complete resolution of clinical symptoms after 19 days of saridegib treatment. The arrow in denotes the bulging skull caused by tumor. (B) A response to saridegib was apparent by gross pathology, (C) imaging with Tumor Paint (Ctx-Cy5.5), and (D) H&E staining.

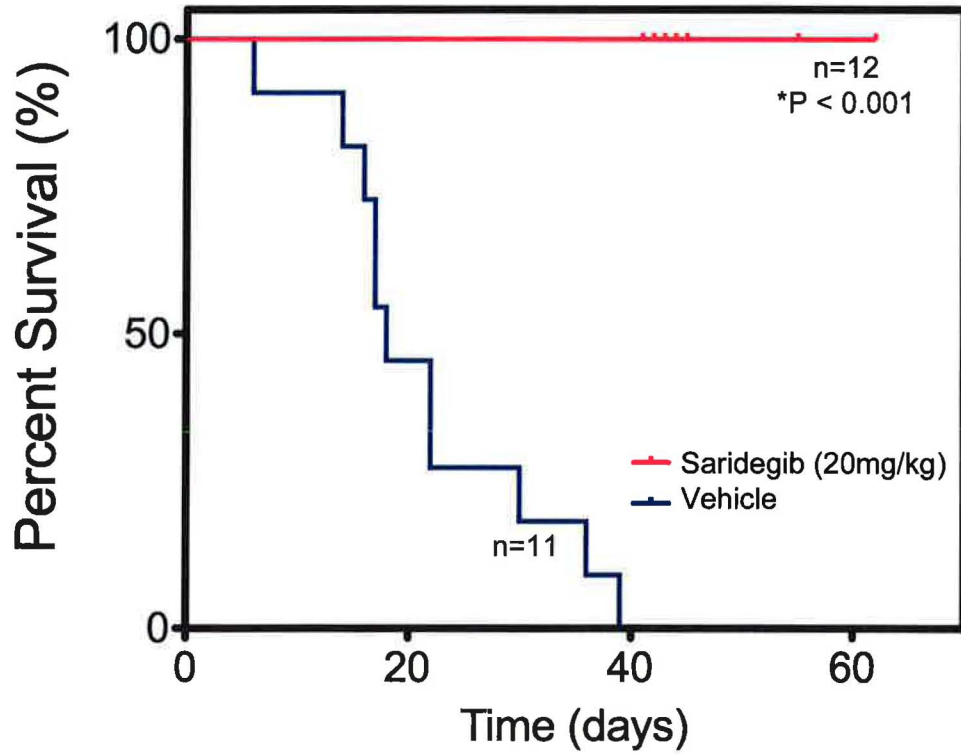


Figure 3.2 Saridegib improves survival in the $Ptc^{C/C}$ medulloblastoma model

Kaplan-Meier analysis demonstrates that all $Ptc^{C/C}$ mice receiving daily saridegib (20mg/kg, red line) survived, while all vehicle-treated mice (blue line) succumbed to their disease prior to the six-week time point ($P < 0.001$).

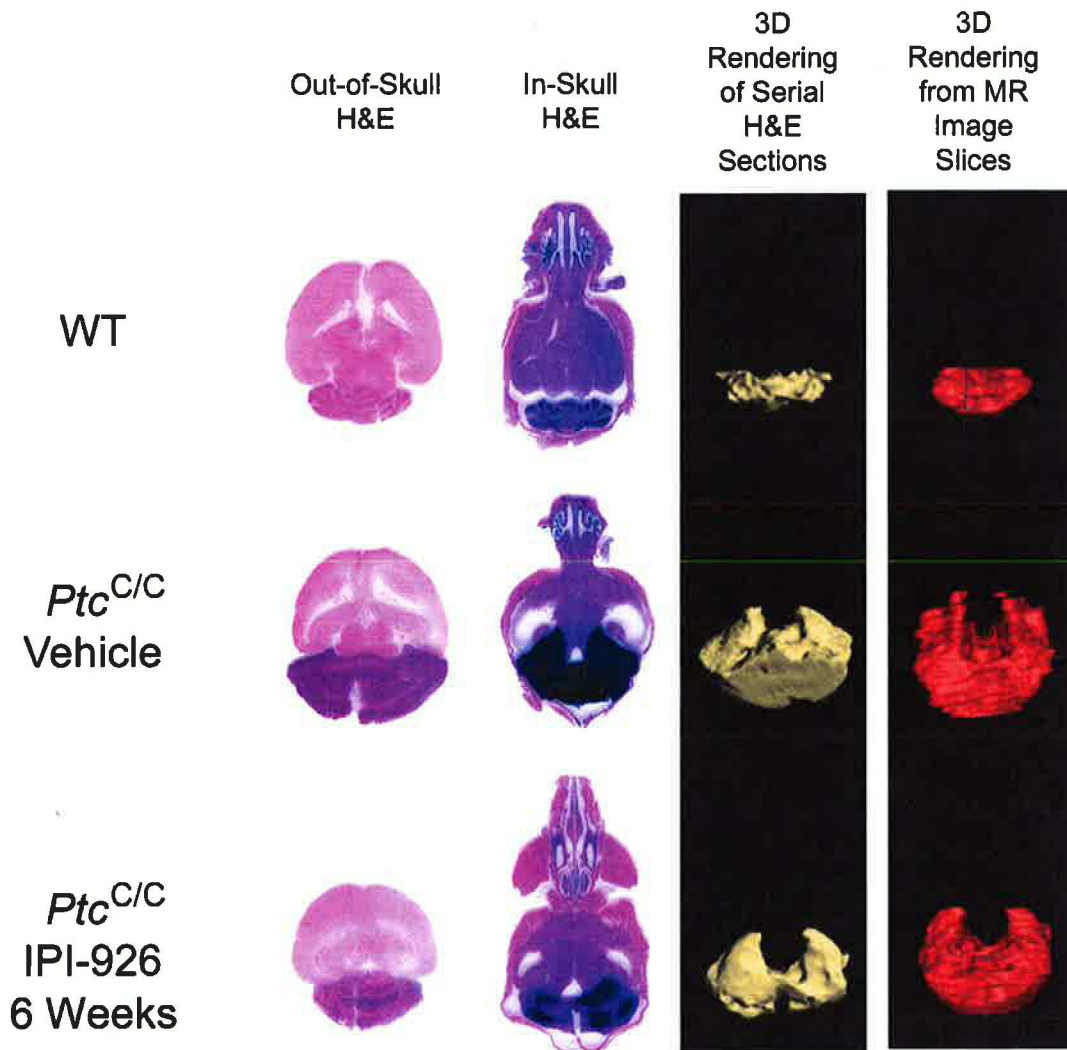


Figure 3.3 3D tumor volume rendering and analysis of pathology

Image panel summarizing a comparison of tissue sections from brains processed outside of (leftmost column) or from within the skull (second column) and the related H&E-based 3D renderings (third column) of cerebellar or tumor volume. H&E-based 3D tumor models are matched to the MRI-generated volume model for the same sample (rightmost column).

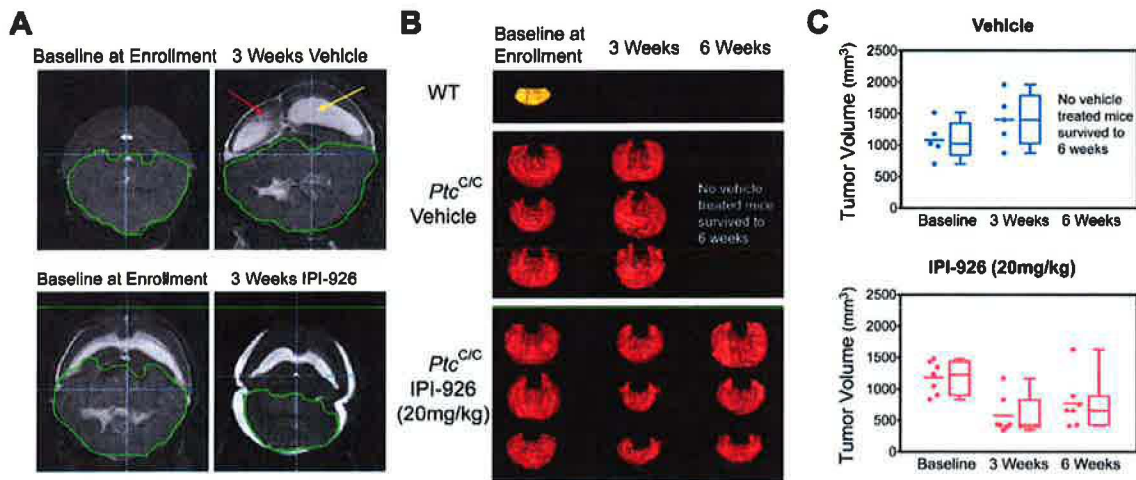


Figure 3.4 MRIs demonstrate decreasing tumor volumes during saridegib administration

(A) A representative T2-weighted MR image demonstrates the enlarged ventricles (yellow arrow) and trans-ependymal cerebral spinal fluid (CSF) flow (red arrow) resulting from cerebellar tumor progression in a vehicle treated mouse. Saridegib treated mice demonstrate a significant reduction in ventricle size and a resolution of trans-ependymal CSF flow. (B) Tumor volume was estimated from MR scans taken at enrollment, after 3 weeks, and 6 weeks of treatment. Representative images of 3D reconstructed tumors are shown, with an untreated wild-type cerebellum displayed for reference (shown in yellow). (C) Tumor volumes (mm³) were estimated at each time point for vehicle treated (n=5) and Saridegib treated *Ptc^{C/C}* mice (n=7). None of the vehicle-treated mice survived until the 6 week imaging time point.

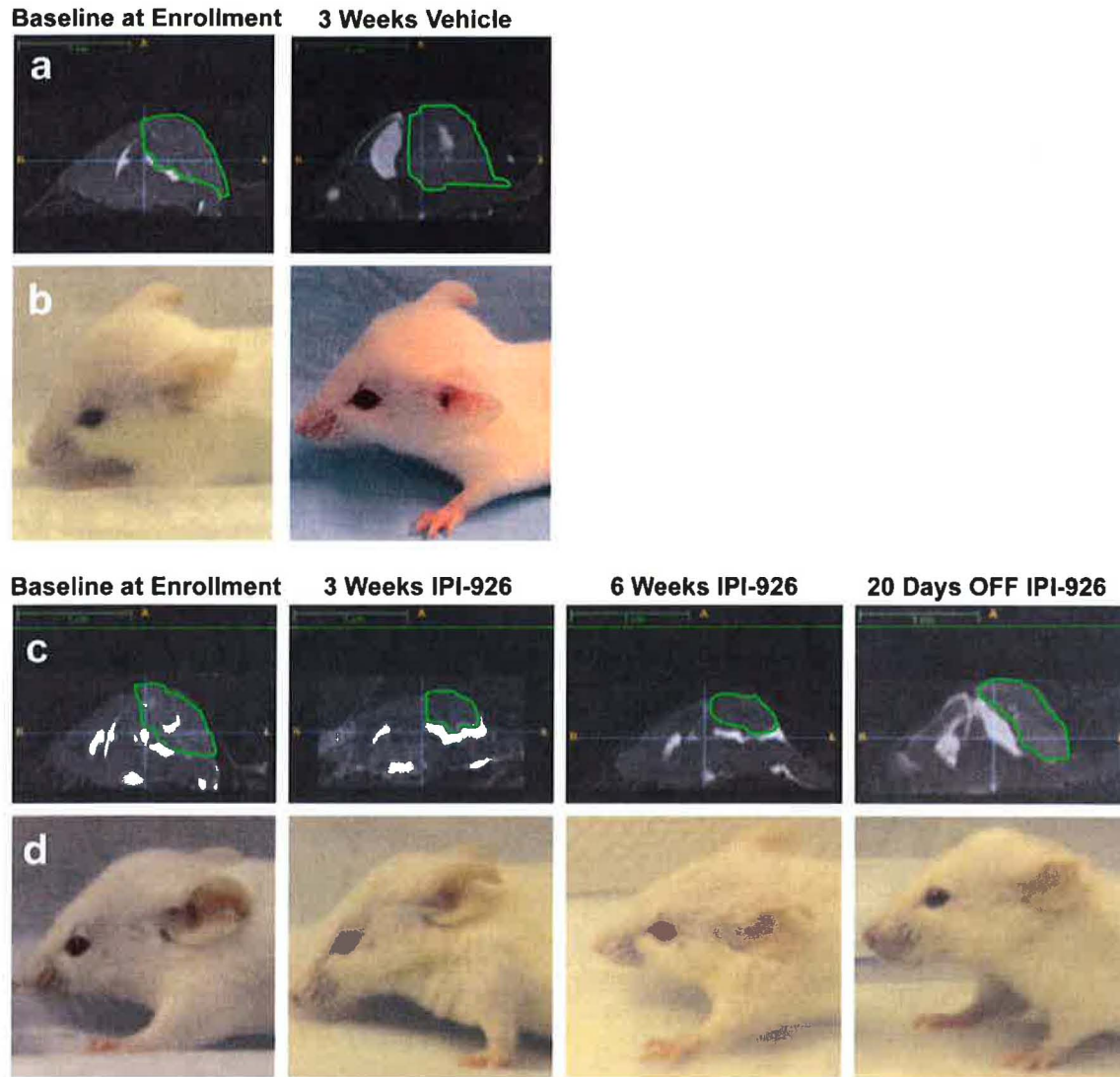


Figure 3.5 Monitoring tumor response via MRI

(A and C) Representative MRI scans in the sagittal plane from vehicle-treated (A) or saridegib-treated (C) $Ptc^{C/C}$ mice are shown at enrollment, after 3 wk of daily saridegib treatment, after 6 wk of daily saridegib treatment, and after drug withdrawal. T2-weighted axial images were acquired at 3 T with a Philips MRI system and a custom mouse-head coil. Control mice were imaged at enrollment and after 3 wk on daily vehicle treatment, although no vehicle-treated mice survived until the 6-wk imaging time point. (B and D) Live animal images are shown in parallel with the MRI scans for vehicle-treated (B) and saridegib-treated (D) mice. Saridegib maintenance administration prolongs survival in medulloblastoma mice

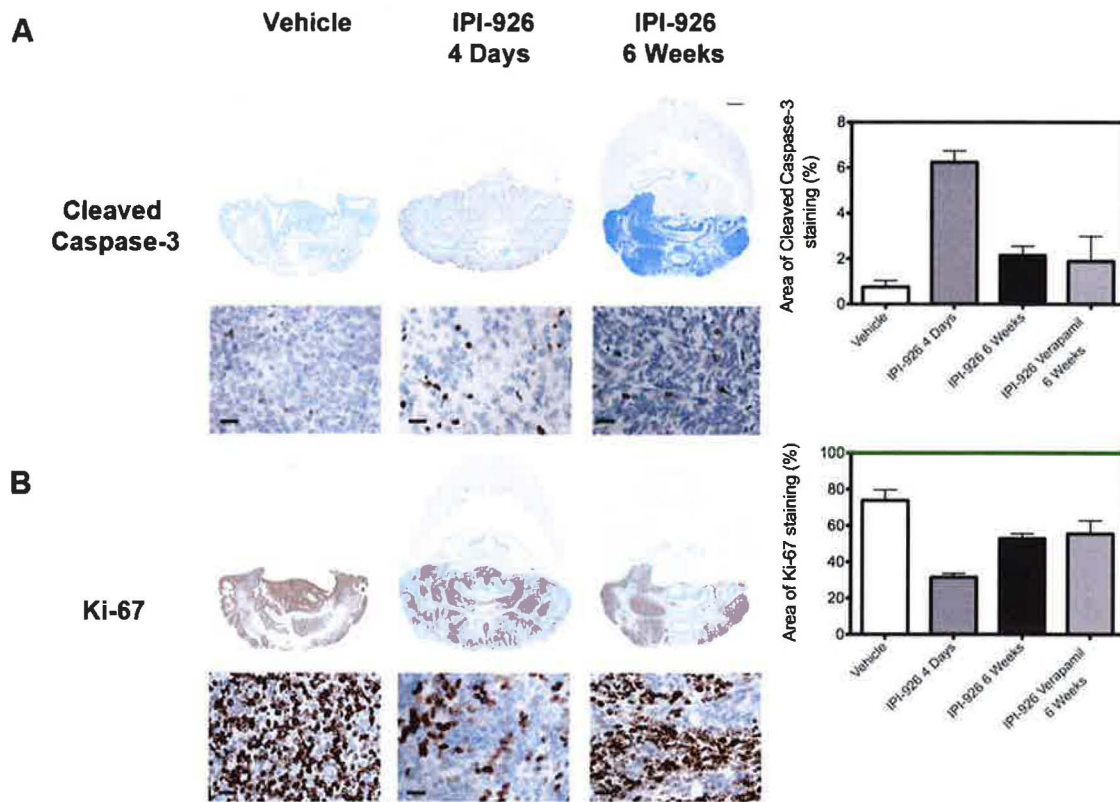


Figure 3.6 Effect of saridegib on proliferation and apoptosis

Representative examples of immunohistochemical analysis of $Ptc^{C/C}$ tumors stained with Cleaved Caspase 3 (A) and Ki67 (B) antibodies are shown. Percentage area of active Caspase 3 and Ki67 were quantified with Image J. Compared with vehicle-treated controls, mice treated with the saridegib (20 mg/kg) show reduced expression of Ki67 and increased Cleaved Caspase 3 staining after 4 d of treatment. The effect of the drug on apoptosis and proliferation was reduced after 6 wk of daily therapy. Verapamil and saridegib combination therapy resulted in similar apoptotic and proliferative responses compared with saridegib alone. (Scale bars: Upper, 1 mm; Lower, 50 μ m.) Individual data points represent the means \pm SEM of three independent samples from each treatment.

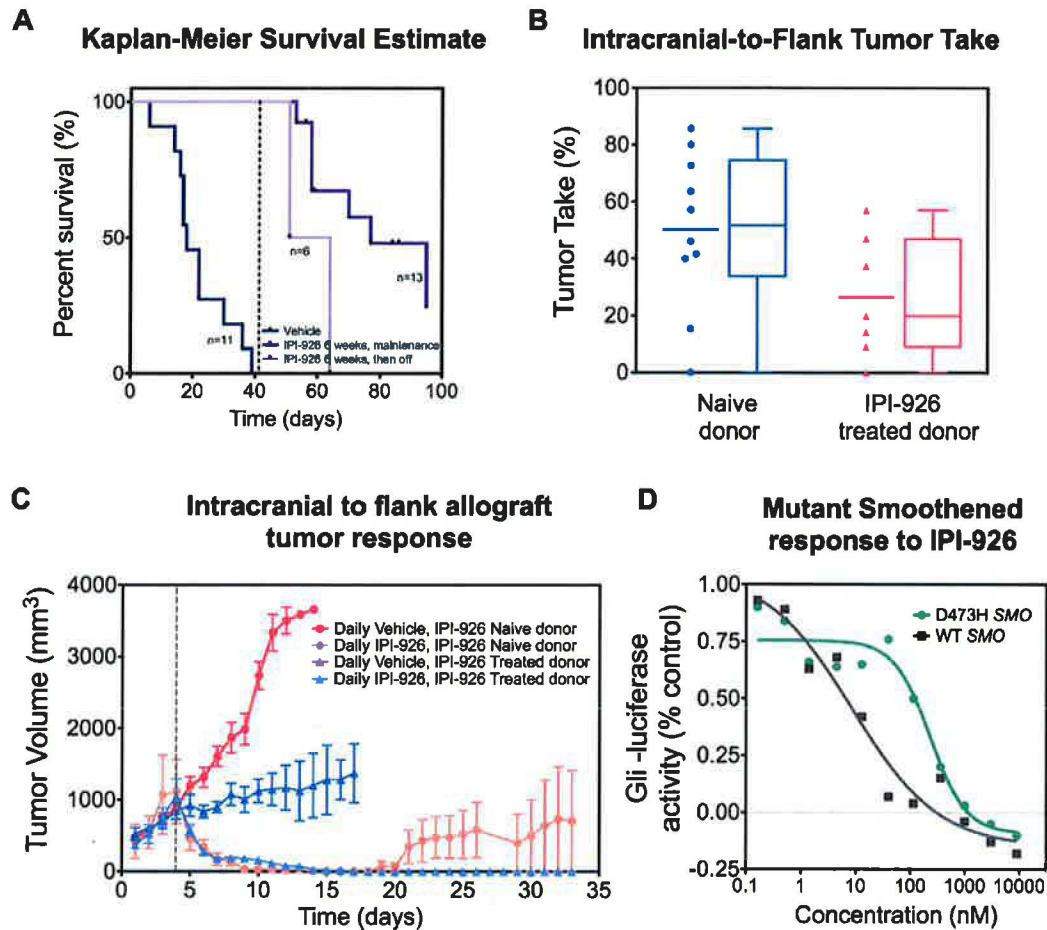


Figure 3.7 Saridegib maintenance administration prolongs survival in medulloblastoma mice

(A) Three- to five-week-old *Ptc^{C/C}* mice symptomatic for medulloblastoma were randomized to receive vehicle (blue line) or saridegib. Mice were initially given daily saridegib (20 mg/kg/dose) for six weeks (n=24), and were then taken off the drug (n=12; light purple line) or given maintenance dosing (20 mg/kg twice per week) for six additional weeks (n=12; purple line). Daily saridegib followed by twice weekly dosing provided a significant survival benefit compared to vehicle controls ($P < 0.001$) and to mice taken off drug ($P = 0.001$). (B) Flank allografts were established in 43% of recipients from drug-naïve *Ptc^{C/C}* donors. Only 23% of recipients developed flank tumor when donors were treated with saridegib daily for 6 weeks (20 mg/kg) prior to transplantation. (C) Recipient mice bearing drug-naïve and saridegib treated allograft tumors were then treated with daily saridegib (20mg/kg). Dotted line indicates beginning of treatment. Tumors were undetectable in both allograft groups by day 15. Two of five tumors became unresponsive during the 9-week trial despite initial response to saridegib. (D) The average Gli-luciferase reporter activity was measured in C3H10T1/2 cells transfected with wild type *SMOOTHENED* (*SMO*) (squares) or the D473H *SMO* mutant (triangles) after treatment with various doses of saridegib. Saridegib inhibited reporter activity at an IC_{50} of 9nM in C3H10T1/2 cells transfected with wild type *SMO* and also showed activity against the D473H *SMO* mutant at an IC_{50} of 244nM. Reporter activity is normalized to untreated C2H10T1/2 cells. (Error bars, SEM)

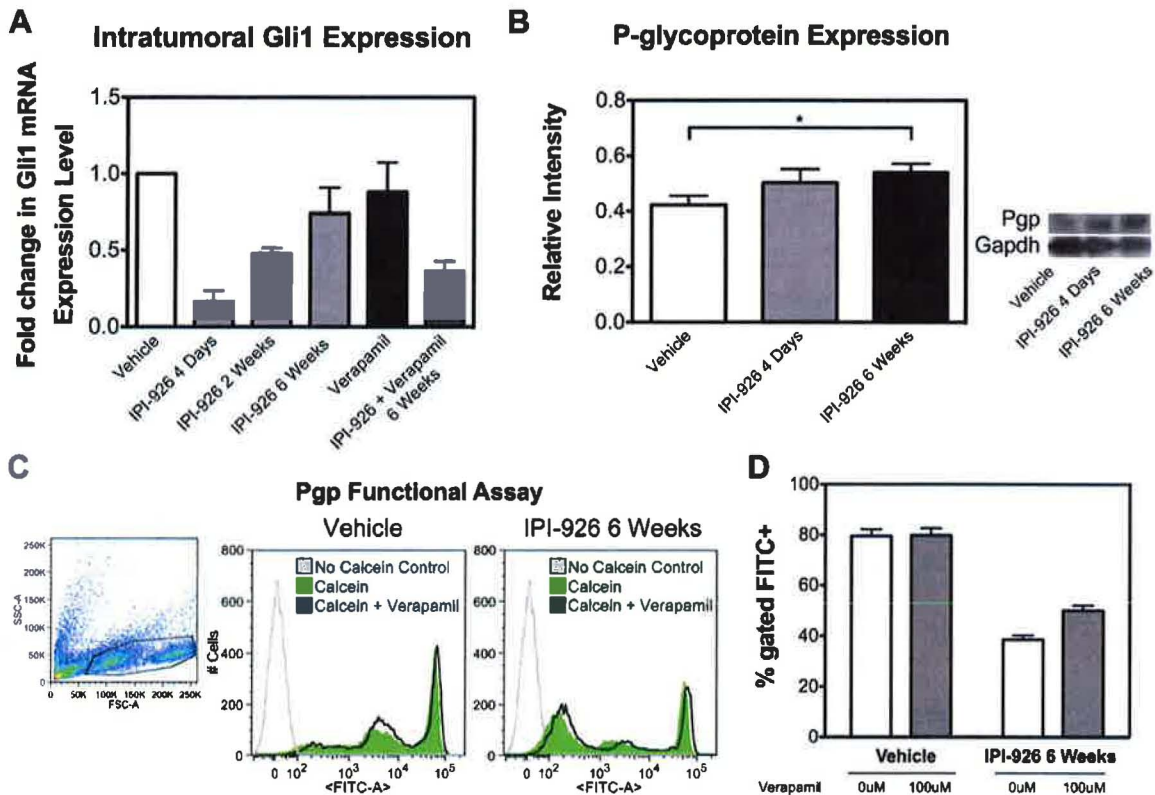


Figure 3.8 Mechanisms of resistance in saridegib treated *Ptc*^{C/C} tumors

(A) The pharmacodynamic activity of saridegib in *Ptc*^{C/C} tumors was confirmed by analysis of *Gli1* mRNA by RT-PCR. Result shows a substantial decrease in *Gli1* expression after 4 days of saridegib treatment ($P=0.05$). The initial reduction in *Gli1* expression seen in response to daily saridegib (20mg/kg/dose) was diminished after 6 weeks of therapy. Drug resistance to saridegib was partially reversed by co-treatment with Pgp inhibitor verapamil. Bars represent the average fold change in *Gli1* expression normalized to vehicle-treated controls ($n=3$ per group; error bars = SEM). (B) The expression of Pgp was quantified via Western blot at enrollment, after 4 days, and 6 weeks of treatment. Bars represent the average fold change in Pgp normalized to Gapdh ($n=3$ per group). Error bars, SEM. (C) Efflux activity of Pgp in saridegib treated *Ptc*^{C/C} was evaluated by measuring the intracellular fluorescence of calcein with flow cytometer. Compared to vehicle controls, saridegib treated tumors had lower calcein accumulation. Inhibiting the Pgp activity with 100 μ M verapamil increased calcein fluorescence as indicated by small shift of peak to the right. Gray line indicates autofluorescence of the cells that were not exposed to calcein-AM. (D) Percentage of cells appears within FITC positive gate was quantified. Pgp-mediated efflux activity was significantly increased in *Ptc*^{C/C} tumors treated with saridegib ($n=3$ per group; error bars = SEM).

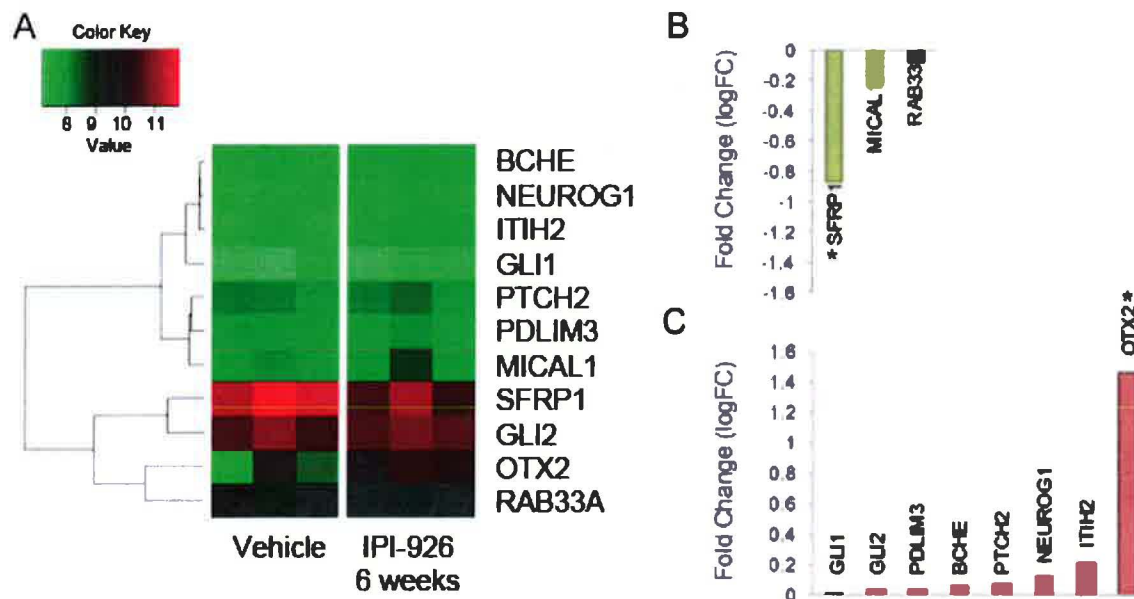


Figure 3.9 Differential gene expression in vehicle- and saridegib-treated *Ptc*^{C/C} samples

(A) Three independent vehicle- and saridegib-treated *Ptc*^{C/C} samples were analyzed with the use of an Illumina expression array. The heat map depicts the expression of the Sonic Hedgehog (Shh) signature genes. (B) Differentially expressed Shh signature genes highly expressed in vehicle-treated compared with saridegib-treated *Ptc*^{C/C} samples. (C) Differentially expressed Shh signature genes highly expressed in saridegib-treated compared with vehicle-treated *Ptc*^{C/C} samples.

Genotype	Treatment	Statistics	Tissue concentration		
			Cerebellum/tumor, ng/g	Forebrain, ng/g	Plasma, ng/mL
WT	None	Mean	0	0	0
		SD	0	0	0
<i>Ptc^{C/C}</i> intracranial tumors	Saridegib for 4 d, daily, 20 mg/kg per dose	Mean	482	393	652
		SD	75	84	276
	None	Mean	0	0	0
		SD	0	0	0
	Saridegib for 4 d, daily, 20 mg/kg per dose	Mean	478	300	803
		SD	98	32	316
	Saridegib for 6 wk, daily, 20 mg/kg per dose	Mean	1,269	376	1,135
		SD	570	58	411
	Saridegib for 3 wk, daily, 20 mg/kg per dose; one dose at 70 mg/kg	Mean	5,956	1,659	1,830
		SD	2,302	421	349
Saridegib for 3 wk, daily, 20 mg/kg per dose; 3 wk, one dose per week, 70 mg/kg	Mean	8,911	1,569	2,553	
	SD	1,726	469	501	
<i>Ptc^{C/C}</i> flank allografts (WT recipients)	None	Mean	0	N/A	N/1
		SD	0	N/A	N/A
	Saridegib for 7 d, daily, 20 mg/kg per dose	Mean	47,320	N/A	N/A
		SD	27,887	N/A	N/A
	Saridegib, daily, 20 mg/kg per dose until tumor regrowth	Mean	22,053	N/A	N/A
		SD	3,834	N/A	N/A

N/A, not applicable.

Table 3.1 Drug concentrations in plasma, brain and tumor

Category	P	No. of molecules	Genes up-regulated by more than twofold	Genes down-regulated by more than twofold
Cancer	2.19×10^{-27} – 1.04×10^{-03}	173	MT1E, ANXA5, TIMP1, IFITM3, PLEKHB1, EFF1A2	CHRNA3, MTDH
Neurological disease	6.03×10^{-25} – 8.09×10^{-04}	159	C3, SPP1, PDGDS, VSNL1, ENO2, PVALB, OTX2, CHI3L1, ITPR1, PCP2, LCN2, THY1, DCN, SLC24A2, C4B, MBP, IGFBP5, ATP2A3, HSPB8	CHRNA3, MTDH
Skeletal and muscular disorders	7.15×10^{-25} – 1.24×10^{-03}	154	C3, SPP1, PDGDS, VSNL1, ENO2, PVALB, CHI3L1, ITPR1, LCN2, THY1, C4B, MBP, IGFBP5, ATP2A3, HSPB8	CHRNA3, MTDH
Cell death	1.27×10^{-19} – 1.29×10^{-03}	140	LGALS3, C3, HBB, HBA1/HBA2, SPP1, PTGDS, CALB2, OTX2, CHI3L1, ITPR1, LCN2, Lyz1/Lyz2, THY1, DCN, MBP, IGFBP5, GADD45G, HSPB8, PCSK9, GFAP	MTDH
Cellular movement	9.06×10^{-15} – 1.26×10^{-03}	96	LGALS3, C3, SPP1, VSNL1, CHI3L1, ITPR1, LCN2, Lyz1/Lyz2, THY1, DCN, C4B, IGFBP5, RASGRF1, GFAP	—
Cellular growth and proliferation	2.13×10^{-14} – 1.08×10^{-03}	136	LGALS3, C3, SPP1, GPNMB, PTGDS, OTX2, ITPR1, LCN2, THY1, DCN, MBP, IGFBP5, GADD45G, HSPB8, RASGRF1, GAD1	—
Tissue development	1.18×10^{-13} – 1.04×10^{-03}	126	LGALS3, C3, HBB, HBA1/HBA2, SPP1, PTGDS, VSNL1, OTX2, KNDC1, ITPR1, LCN2, ATP1B1, THY1, DCN, C4B, MBP, IGFBP5, GADD45G, RASGRP1, PCSK9, GFAP	CHRNA3
Nervous system development and function	2.55×10^{-11} – 1.26×10^{-03}	96	C3, HBA1/HBA2, VSNL1, OTX2, CHI3L1, KNDC1, ITPR1, ATP1B1, THY1, SLC24A2, MBP, RASGRP1, PCSK9, GFAP	CHRNA3
Hematological system development and function	2.46×10^{-10} – 1.24×10^{-03}	89	LGALS3, C3, HBB, HBA1/HBA2, SPP1, PTGDS, CHI3L1, LCN2, Lyz1/Lyz2, THY1, DCN, C4B, MBP, GADD45G, HSPB8, GFAP, GJA1	—
Immune cell trafficking	2.46×10^{-10} – 1.24×10^{-03}	64	LGALS3, C3, SPP1, PTGDS, CHI3L1, LCN2, Lyz1/Lyz2, THY1, DCN, C4B, MBP, HSPB8, GFAP, ANXA5, NBL1, TIMP1	—

Genes from the dataset that met the log-ratio cutoff of ≥ 0.5 and $P < 0.05$ were considered for the analysis.

Table 3.2 Top 10 networks of the genes significantly altered in saridegib treated Ptc^{C/C} tumor

Genes from the dataset that met the log ratio cutoff of $\geq |0.5|$ and P value < 0.05 were considered for the analysis.

Symbol	Entrez gene name	Log ratio	P
Log ratio up-regulated			
LGALS3	Lectin, galactoside-binding, soluble, 3	2.232	1.56×10^{-16}
C3	Complement component 3	2.072	6.61×10^{-16}
HBB	Hemoglobin, β	2.000	6.62×10^{-09}
HBA1/HBA2	Hemoglobin, α 1	1.741	2.07×10^{-08}
SPP1	Secreted phosphoprotein 1	1.736	3.12×10^{-10}
GPNMB	Glycoprotein (transmembrane) NMB	1.705	1.34×10^{-12}
PTGDS	Prostaglandin D2 synthase 21 kDa (brain)	1.687	6.73×10^{-13}
CALB2	Calbindin 2	1.612	7.28×10^{-13}
VSNL1	Visinin-like 1	1.535	1.98×10^{-13}
ITIH3	Inter- α -trypsin inhibitor heavy chain H3	1.529	4.69×10^{-15}
ENO2	Enolase 2 (γ , neuronal)	1.520	2.95×10^{-13}
PVALB	Parvalbumin	1.477	7.28×10^{-13}
OTX2	Orthodenticle homeobox 2	1.460	3.86×10^{-08}
Log ratio down-regulated			
RPRML	Reprimo-like	-2.173	5.42×10^{-19}
MAK16	MAK16 homolog (<i>Saccharomyces cerevisiae</i>)	-1.481	3.60×10^{-11}
THAP4	THAP domain-containing 4	-1.081	6.54×10^{-08}
CHRNA3	Cholinergic receptor, nicotinic, α 3	-1.071	1.08×10^{-08}
MTDH	Metadherin	-1.055	1.39×10^{-07}
MAP2	Microtubule-associated protein 2	-0.953	8.11×10^{-06}
MCM6	Minichromosome maintenance complex component 6	-0.937	1.42×10^{-06}
GSTO1	GST ω 1	-0.911	3.43×10^{-07}
SFRP1	Secreted frizzled-related protein 1	-0.868	1.16×10^{-05}
ISLR2	Ig superfamily containing leucine-rich repeat 2	-0.830	3.87×10^{-03}
OTX1	Orthodenticle homeobox 1	-0.820	9.15×10^{-05}

A cutoff of log ratio $\geq |0.5|$ and $P \leq 0.05$ were used to define focus genes in the network analysis.

Table 3.3 Top genes differentially expressed in saridegib treated *Ptc*^{C/C} tumor

A cut-off of log ratio $\geq |0.5|$ and p-value ≤ 0.05 were used to define focus genes in the network analysis.

Exon	Forward primer, 5' → 3' (each prefixed with M13 forward)	Reverse primer, 5' → 3' (each prefixed with M13 reverse)
1	AAGCTGGCCCCAGACTTTC	CAACAGTTTGAGGCCTGAGC
2	GCATAAGGCAACCCTTAGCA	GCTTGACAACCATGCTCCAT
3	GCCCTATGAGGTAGGGGCTA	AGCCACAAAGGTGGCCTAAA
4	CACCAGGACATGCACAGCTA	GGACACAGGTCCGATTTGAA
5	AGCATTGCCCTGTTGTGTTT	CCAGCACGGTACCGATAGTTC
6	CTATGCCTTGATGGCTGGAG	GAACCTTGGTCATGGCTTTG
7	AGGCTCTGTCCCAGTTACCG	CCCCTTCTCAGAGGGGAGTTG
8	TGTAGCCACCCTGGACTCAG	ACCTGCTCCTGTGCATTGAC
9	CCATGAGAATCACGCAGTGG	GGTCCTGTGGCTCCTACTT
10	CTGTGAAGGCCTCAGCTCCT	CAGAGAAGAAGGAAGAGAGAGCAA
11	GCTCCAGGGTGGAATCTCTC	CACTGTCAGGGGGACAAAGA
12	ACCTGAAGGAGATGCCAAGG	CAGACACTTGGCCCACAGAC

PCR primers were designed with Primer3 and incorporated either M13 forward (5'-TGTA AACGACGGCCAGT-3') or M13 reverse (5'-CAGGAAACAGCTATGAC-3') priming sites.

Table 3.4 Primer used for sequencing

PCR primers were designed with Primer3 and incorporated either M13 forward (TGTA AACGACGGCCAGT) or reverse (CAGGAAACAGCTATGAC) priming sites.

CHAPTER 4

Mid-Size Medicines for the Treatment of Brain Cancer

Summary

Our study focused on identifying cysteine knot peptide variants that differentially recognize medulloblastoma brain cancer cells. We found that glypican-2, a member of the proteoglycan family, was markedly elevated in medulloblastoma cancer cells compared to normal brain cells. Glypicans are typically thought to act as co-receptors for other growth factors signaling pathways (e.g., integrin, and protein-tyrosine phosphatase) (Sakamoto and Kadomatsu, 2012). Glypican expression is associated with a wide variety of cancers including hepatocellular, breast, ovarian, and pancreatic cancer, although the particular role of glypican-2 has not been well studied. Previous studies indicate that dimerized midkine acts as a pro-oncogenic ligand that activates glypican-2. We hypothesize that monomeric midkine would act as a dominant negative-binding to glypican-2 in competition with the dimerized form. Our aim is to express only a C-terminal half of midkine that would bind to glypican-2, but would not crosslink the receptor and initiate signaling. It is hoped that this could inhibit both full-length midkine and inhibit the shared glypican pathway used by a variety of growth factors. If successful, these foundational studies would provide the insights into the use of cysteine knot peptide variant libraries and, also, produce novel cancer-specific variants that may be used directly to develop cancer therapeutics. In the event that the engineered midkine derivative specifically binds to medulloblastoma cells, but does not interfere with growth, the peptide could be used to target chemotherapy specifically to medulloblastoma cells.

Introduction

Peptide therapeutics and diagnostics

Cysteine-knots miniproteins, also known as knottins, are small bioactive proteins (20-40 amino acids) that are heavily disulfide bonded, conferring structural stability and protease resistance. They are commonly found in the venom of poisonous insects and have therefore been designed through evolution to be effective as injectable drugs. Knottins possess natural properties that make them attractive for *in vivo* applications. First, their highly cross-linked core structures confer high thermal and proteolytic stability. Consequently, knottins have been shown to retain their 3D structure in harsh environments (e.g., acid, base, serum), making them potentially suitable for oral drug therapy. Second, knottins have the ability to disrupt protein-protein interactions. Unlike small molecules, peptides can be selected for broad interfaces with proteins and can block protein interactions. Further, their small size has translated

well into desirable pharmacokinetic and biodistribution properties for molecular imaging applications. The small size of these knotted proteins can penetrate into solid tumors, perhaps more effectively than antibodies. Remarkably, although they are 40 times smaller than an antibody, they possess similar amounts of variable region and therefore maintain antibody-like specificity (antibodies generally utilize only a small fraction of their Complementarity Determining Regions, with the rest serving as germline scaffolding). While knottin peptides can be engineered to match antibody affinity, some knottins appear superior to antibodies for crossing the blood brain barrier (BBB) and penetrating into solid tumor tissue.

The first knottin-based protein that was developed in our lab is a tumor-imaging agent, a bioconjugate of chlorotoxin and a near infrared fluorophore, called the Tumor Paint. This imaging agent is capable of targeting and illuminating brain tumors, even in the presence of an intact BBB. Therefore, the use of a knottin scaffold to generate peptides with drug-like properties is a promising strategy for the development of therapeutics for brain tumors.

Heparan sulfate proteoglycans (HSPGs)

Heparan sulfate proteoglycans (HSPGs) are composed of a core protein to which a number of highly charged heparan sulfate polysaccharide chains (40-300 sugar residues) are covalently linked. The basic heparan sulfate structure consists of a repeating disaccharide, constituted by uronic acid and hexosamine residues with various degrees of sulfation. HSPGs are ubiquitously expressed in many animal cells and are a major component of extracellular environment in brain. Present on the cell surface and in extracellular membrane (ECM), HSPGs play an important role in a number of biological processes based on their ability to bind and regulate activities of a wide range of ligands including cytokines, chemokines and growth factors (Kirkpatrick and Selleck, 2007). HSPGs can localize bound signaling molecules to their cognate receptors on cell surfaces, or help to form molecular gradients for directional cellular activities. In addition, HSPGs are typically thought to act as co-receptors for growth factors which bind to their heparan sulfate glycosaminoglycan (GAG) chains. Interaction between fibroblast growth factor (FGF) and heparan sulfate chains is a well-studied example. The binding of FGF2 to its receptor, FGFR, causes phosphorylation of tyrosine kinase domain of the receptor and leads to increased growth, migration, and differentiation in several cancers. HSPGs play an integral role in FGF2-FGFR interaction by localizing FGF2 near the receptor and forming a bridge that stabilizes the ligand-receptor complex (Raizen et al., 2006).

Since HSPGs can act as co-receptors by facilitating the formation of ligand-receptor complexes and effectively altering the required concentration of ligand, it is not surprising that they are expressed in the tumor environment. Indeed, glypican expression is associated with a wide variety of cancers including hepatocellular, breast, ovarian, and pancreatic cancer and some studies have shown that

glypican families (HSPGs that are GPI-linked) are important for efficient angiogenesis and metastasis of the cancer (Aikawa et al., 2008).

Glypicans

Glypicans are family of HSPGs that are linked to the external surface of the plasma membrane via glycosylphosphatidylinositol (GPI) anchor (Figure 4.1). Glypicans have negatively charged heparan sulfate GAG chains (Galisteo et al., 2006) that are covalently linked to a core protein core (40-70kDa). Heparan sulfate GAG chains are responsible for biological functions of HSPGs and the core proteins have evolved to maximize their efficiency in these functions.

Glypicans comprise a family of six distinct genes in mammals (Galisteo et al., 2006) (Table 4.1). Glypicans can be divided into two broad subfamilies: glypican-1, -2, -4, -6 and glypicans-3, -5, with approximately 25% amino acid identity between groups. However, the fact that GAG chain moieties mediate much of the function of glypicans, a likelihood of functional redundancy is particularly high. All glypicans are highly expressed during embryonic development. Interestingly, their expression levels vary in a tissue-specific manner. Glypican-1 is a major proteoglycan in the developing and adult brain, but it is also expressed in the kidneys, perichondrium, and several other tissues (David et al., 1990). Glypican-2 (cereberoglycan) expression, in contrast, is expressed exclusively in the developing brain (Stipp et al., 1994). Glypican-2 expression peaks as neurons differentiate and migrate to their appropriate locations and extend neurites, and then the expression is turned off. Glypican-3 is highly expressed in the developing intestine and in mesoderm-derived tissues (Pellegrini et al., 1998), whereas glypican-4 shows a predominant expression in blood vessels, kidney, brain, and adrenal cortex (Watanabe et al., 1995). Glypican-5 shows a developmentally regulated expression in kidney, limb, and brain (Saunders et al., 1997), with brain expressions that persist into the adult. Glypican-6 shows predominant expressions in mesenchymal tissues during development. Consistent with a proposed role in development, the expression patterns of these glypicans often coincide with those of growth factors (e.g. Wnt, Shh, BMP, TGF β , and EGF, and FGF), and their receptors (Yayon et al., 1991).

Since glypicans are expressed predominantly during development, defects in glypican expression generally produce subtle and tissue-restricted defects (Perrimon and Bernfield, 2000). Most likely this reflects a relatively large number of HSPGs (six glypicans), and a likelihood of functional redundancy. Glypican-1 and -3 null mutant mice were viable and fertile. No mutants have been reported for glypican-2, -4, -6. Glypican-1 knock-out mice showed significant reduction in brain size (22% reduction compared to the wild-type littermates), with only subtle mispatterning in anterior cerebellum (Jen et al., 2009).

Heparan sulfate-based treatment strategies

The involvement of glypican genes in cancers has raised the question whether they can be targets of molecular therapies. Given the ability of heparan sulfate chains to bind to a variety of regulatory proteins, the potential treatments of malignancy involving HSPGs are aimed at targeting such interactions.

One main target for heparan sulfate-based therapy is inhibition of heparanase activity. Heparanase is an endo- β -glucuronidase capable of cleaving the heparan sulfate side chains of HSPGs (Afratis et al., 2012). Upregulation of heparanase has been documented in human cancer of various origins, including colon, gastric, liver, and pancreas (Hermano et al., 2012). In many cases, heparanase induction correlated with increased tumor metastasis, angiogenesis, and poor patient outcome (Vlodavsky and Friedmann, 2001; Ilan et al., 2006), thus suggesting heparanase as an attractive therapeutic target. A variety of inhibitory compounds have been developed, including heparin, heparin-mimicking compounds, PI-88 (phosphomannopentaose sulfate), and low-molecular-weight heparin (LMWH) - a series of heparin fragments that share many of heparin's activities. Current clinical trials using a heparan sulfate mimic and heparin-like polyanionic compounds that inhibit heparanase activity have produced promising results in cancer patients (Klerk et al., 2005; Rickles, 2006). For example, PI-88 is currently being evaluated in multiple phase II/III trials for recurrent hepatocellular carcinoma, prostate cancer, metastatic melanoma, and multiple myeloma (Liu et al., 2009). This inhibitor prevents angiogenesis and tumor growth by blocking specific interactions of FGF and VEGF with their receptors and heparan sulfate chains (Ferro et al., 2007).

Other possible heparan sulfate-dependent treatments for cancer therapy involve proteins or peptides with positively charged amino acid residues that act as competitive inhibitors of growth factor binding to heparan sulfate chains, thereby attenuating down-stream receptor signaling activation. An example is suramine, which has the ability to bind to heparin-binding sites of proteins (Marchetti et al., 2003) and is undergoing phase III clinical trial for advanced stage breast cancer patients.

Since heparan sulfate chains are ubiquitous in our body, the clinical application of targeting heparan sulfate chains still requires a better understanding of the specificity involved in HS-protein interactions.

Midkine (MK)

Midkine (MK) is a heparin-binding neuroregulatory factor that participates in neuronal cell migration and neurite outgrowth (Muramatsu, 2002). Previously, it was reported that midkine binds to oversulfated structure in heparan sulfate in glypican-2 (Kurosawa et al., 2001). MK is strongly expressed during the embryogenesis, but in adults it is only expressed in damaged tissues and involved in the

reparative process. MK is also expressed in a variety of malignant tumors and promotes their growth and invasion.

MK is a highly basic, non-glycosylated polypeptide that contains five intrachain disulfide bonds. MK has a molecular weight of about 13kDa (Figure 4.2A). MK is composed of two domains that are linked by disulfide linkage (Fabri et al., 1993). Initial structural and functional studies indicated that the C-terminal half of MK contains the main heparin-binding sites and this is responsible for the main mechanism of action. C-terminus domain has two clusters of basic amino acids: Cluster-1 (K79, R81, and K102) and Cluster-2 (K86, K87, and R89) (Akhter et al., 1998; Iwasaki et al., 1997) (Figure 4.2B). MK forms dimers via spontaneous association and when it does, Cluster 2 in the C-terminal domains form fused heparin-binding site at the dimer interface (Figure 4.2C). This fused heparin-binding sites on MK fit the sulfate group clusters on heparin (Iwasaki et al., 1997). MK dimer has shown to be the active form and dimerization of MK allows stronger heparin-binding activity.

Molecular Dynamics (MD)

Proteins are not static but dynamic. The backbone and side chains of proteins are in constant motion due to thermal motion or kinetic energy of the atoms. Although X-ray crystallography gives detailed structural information, it is only a time-averaged snapshot of the protein structure with no kinetic information. On the other hand, nuclear magnetic resonance (NMR) can detect motion of individual atoms within protein, but give limited structural information. No single experiment or combination of experiments can provide an all-inclusive view of the dynamic behavior of all atoms in a protein. Computational studies, however, can provide complementary tool to help study structure and dynamics of the protein. A method that has had a particularly large impact is molecular dynamics (MD). MD is a theoretical physics technique for examining the complex molecular motions and conformational changes in protein, which is often important for understanding their function (Doniach and Eastman, 1999). MD simulation integrates classical Newton's equations of motions and for all atoms in the molecular systems over time. In order to describe the energy of a particular protein system, it is necessary to 1) get a starting configuration of the atoms in the system, 2) set configuration in motions, and 3) calculate a new configuration based on such motions. The equations of motions are of sufficient complexity that the integration is done over a large number of very small discrete time-steps (less than 2fs). At each time step, the potential energy of a system in terms of the geometries of atomic centers is calculated. All atom molecular mechanics force fields due to intramolecular interactions (e.g., bond lengths, bond angles, and dihedral/torsion angles) and non-bonded energies (e.g., Van der Waals and electrostatic interactions) are considered. In the end, MD simulations provide the ultimate detail concerning individual particle motions as a function of time.

In this study, we aimed to engineer the fragment of natural ligand of glypican-2 and computationally designed mutant variants that could potentially act as competitive inhibitors. Furthermore, we employed MD on various these peptide variants to investigate their stability. We investigate how the mutations introduced impact dimerization and conformations of the heparan binding clusters in MKC. The mutant version of MKC we present even have a physiological relevance to cell studies.

Results

Overexpression of Glypican-2 in different types of brain cancers

We analyzed gene expression profiles in 12 pediatric medulloblastoma patients. Among 48,702 probe sets used in the Illumina beadchip, 1318 probe sets had greater than $\log_2FC=2$ and statistically significant difference ($P < 0.005$) between all tumors and normal adult brain. Candidate targets were narrowed down to 250 probe sets based upon their surface expression. These include genes known to be relevant in oncogenesis such as cell proliferation, apoptosis, development, angiogenesis, invasion and metastasis. We further narrowed down the gene list to genes that have limited expression in normal tissues (e.g., kidney, liver, brain) and that have known peptide ligands. Among the 250 over-expressed genes, we chose to study glypican-2 due to its high level of expression in medulloblastoma compared to normal brain (average: 4.64 fold) and its limited expression in normal tissues other than brain. Overexpression of *Glypican-2* mRNA was also observed in other types of brain cancers including glioblastoma, PNET, and astrocytoma (Figure 4.3A). To validate our results at the cellular level, immunohistochemistry was performed on the four medulloblastoma samples (three orthotopic xenograft and one genetically engineered mouse models). As shown in Figure 4.3B, there were marked overexpression of glypican-2 only in medulloblastoma cancer cells and not in normal brain, although the level varied among samples.

Designing mutant versions of C-terminal domain of MK (MKC)

In order to design competitive inhibitors of heparan sulfate chain of glypican-2 that prevent cross-linking the signaling complex, we focused on designing variants involving the C-terminal half of MK (from now on denoted as MKC). First, the dimer form of MKC was manually created using Chimera by aligning two MKC monomers (from now on, we denote each monomer by MKC-A and MKC-B) based on the proposed dimer model (Iwasaki et al., 1997). When designing new protein, we used computational methods to assay theoretical point mutations and rotamer optimization for increased stability and function of the protein. Using Foldit software, the sequence and conformation of a protein were optimized to find

low-energy sequence-structure pairs. Although the mutations were not explicitly modeled in the presence of the substrate or heparan sulfate, we hypothesized that some of the proteins in the designed library would prevent formation of co-receptor while still allowing heparan sulfate to bind.

The disulfide-rich knottin scaffold is considered as a useful stabilizing framework. Therefore, we kept two disulfide bonds (Cys1-Cys33 and Cys11-Cys43) intact within MKC in the process of introducing mutations. A summary of each mutant is given in Table 4.2. In Mutant1, all lysines were changed to arginines. Mutant1 was generated based on our previous experimental knowledge that multiple lysine residues can lead to multi-labeled fluorescence molecule rather than a single-labeled peptide that is preferable for drug development and manufacturing. For Mutant2, negatively charged (e.g., Aspartate) and positively charged (e.g., Arginine) residues were introduced to create stabilizing salt-bridges. For Mutant3, mutations were introduced along linker regions (between two monomers) for stronger dimerization. For Mutant4, mutations were only made on the surface opposite to the heparin binding sites.

Potential energies and number of H-bonds were calculated using software Chimera and the results are reported in Table 4.2. Mutant1 had no change in total number of H-bonds; however, substitution of lysine to arginine significantly decreased the potential energy (-10659.37). In case of Mutant 2 and Mutant3, there was no significant change in the number of H-bonds but both were more stable than WT. Mutant4 had the lowest potential energy (-11188.03).

Dynamics of MKC WT and mutants

Backbone Motion

Four engineered MKC variants were then tested for stability with respect to fold and shape of heparin binding clusters. First, the constructed models were fitted to minimize steric clashes using Chimera. Minimized structures are shown in Figure 4.5. The original secondary structure of MKC monomer has three β -sheets. However, after minimization step in dimer form, MKC-A retained two β -sheets and MKC-B lost all three β - sheets secondary structure.

To elucidate the dynamics of MKC variants, we performed MD simulations of MKC structures with four different mutants at body temperature totaling 15ns of simulation time. The convergence and the stability of the MD trajectories were quantified by $C\alpha$ RMSD, the measure of the deviation of the protein from the initial NMR structure. At body temperature (37°C), Mutant2 had the lowest core $C\alpha$ RMSD to the starting structure ($5.05 \pm 0.0835 \text{ \AA}$) over the step 1800-2000 of stimulation (Figure 4.6A). Continuous increase in $C\alpha$ RMSD in WT, Mutant1, and Mutant4 indicate sustained changes in structure (Figure 4.6B). Not only did the core $C\alpha$ RMSD for Mutant1 increased over time, but also did its standard

deviation, indicating higher structural heterogeneity. On the other hand, C α RMSD values for Mutant3 and Mutant4 were stabilized after 1500 ps of simulation.

The C α RMSF (measure of the deviation between the position of certain residue and initial reference position) was calculated for the core residues over all simulations at 37°C (Figure 4.6C). All four mutants had lower fluctuations about the mean structure than WT. Residues in Mutant3 had the lowest fluctuations, indicative of a rigid structure. As expected, the most rigid regions were within the β -sheets (near residues 4-5; 20-24; 37-39).

Secondary structure Analysis

The dictionary of secondary structure of proteins (dssp) algorithm was used to determine protein secondary structure by looking for repeating main-chain hydrogen bonding patterns (Figure 4.7). A hydrogen bond was assigned if the distance between donor and acceptor atoms was less than 4.0 Å. Dssp module detected alpha-bridges (green), 3/10 helix (pink), beta sheets (red) as well as their corresponding bridges. In MD simulation, secondary structures were lost in almost all simulations, except for MKC-A of Mutant1 and Mutant4. With mutant 4, nine additional H-bonds were formed, resulting in the stabilization of the native β -sheet. In contrast, mutant2 showed the loss of five hydrogen bonds and disrupted the native β -sheet. The numbers of hydrogen bonds for each mutant were shown in Table 4.2.

Core contacts analysis

Two non-bonded residues are considered to be in contact when they are spatially neighboring. If a contact is the same as it presents in the native structure (starting structure), it is called a native contact, otherwise a non-native contact. Considering the protein dynamics microscopically, residues with more native contacts are energetically more favorable. Native contacts are more frequently formed in properly folded protein, whereas non-native contacts are more frequently formed in the misfolded protein.

Native and non-native contacts in the 37 °C simulations of WT and four mutants are plotted in Figure 4.8, with native contacts in grey and non-native in white. The average numbers of contacts per frame in simulations are organized by whether they occurred between atoms in the main chain (mc) or side chain (sc). Mutant2 gained contacts especially native side chain contacts. However, Mutant1 gained more non-native contacts and Mutant3 and Mutant4 had no significant change.

Table 4.3 shows the percentage of charged residues as well as salt bridges formed in each mutant. For Mutant1, there was no change in number of charged residues. Lysine to arginine mutation allowed the formation of Arg2-Glu35 and Arg20-Glu6 native salt bridges (Lys2-Glu35 and Arg20-Glu6 were non-native contacts in WT). In case of Mutant2, 34.88% of residues were charged and five out of seven salt bridges detected were native contacts. All the salt bridges found in Mutant3 were non-native, which

may deter the native salt bridge from forming. Mutant4 had the highest percentage of charged residues (41.86%; 18 out of 43 residues) and thirteen salt bridges were detected. However, more than half were non-native contacts.

Biochemical characteristics of WT and Mutant1 MKC

First, we expressed WT MKC in E.Coli expression system and Daedalus expression system in mammalian 293T cells (Bandaranayake et al., 2011) (Figure 4.9). Expressed proteins were purified using size exclusion chromatography (SEC) and ran on SDS-PAGE gel. MKC expressed in E.Coli showed some extent of misfolding, indicated by smeared multiple bands in SDS-PAGE gel. (Figure 4.10B). MKC expressed in the mammalian system was properly folded, suggested by tight single band. The ability of E.Coli and mammalian MKCs to bind to heparan sulfate chain was examined using heparin-binding column chromatography (Figure 4.10A). Mammalian MKC eluted as a narrow peak centered at 0.86M NaCl, whereas E.Coli MKC came off at 0.8M NaCl. The result indicated that mammalian MKC has higher binding affinity for heparin than E.Coli MKC.

Since MKC proteins failed to fold correctly in E.Coli, we decided to carry all MKC protein expression in Daedalus mammalian system. WT MKC was eluted as a single, monodispersed peak from a SEC, which is an indication of structural homogeneity of the sample (Figure 4.11A). By SDS-PAGE, TEV cleaved fusion protein yielded a single band. In the case of Mutant1 MKC, two monodisperse peaks were detected on SEC, suggesting existence of both monomer and dimer (Figure 4.11B). The earlier fraction contained primarily dimer, whereas later fractions contained monomers. These two peak fractions were ran in SDS-PAGE gel separately and difference in size confirmed the presence of dimer. Replacement of all lysine residues to arginine increased dimerization of MKC.

Discussion

Glypican-2 is a rational target for the treatment of brain cancers because it is predominantly expressed in brain tumors compared to normal brain tissue, implying specificity. In addition, it potentially regulates multiple pathways involved in carcinogenesis, implying a broad spectrum of activity. In this study, we took the fragment of natural ligand of glypican-2 and computationally and experimentally explored the dynamical behaviors of WT and mutant MKC.

Computational structural analysis indicated that all four MKC mutants were more stable than the WT. Previously, it has been shown that addition of salt bridges on the protein surface results in increased thermostability. Salt bridges are special form of hydrogen bonds, composed of negative charges from Asp, Glu, Tyr, Cys and the C-terminal carboxylate group, and of positive charges from His, Lys, Arg and

the N-terminal amino group. In designing Mutant2, six residues were mutated to charged polar residues: Y3R, T15R, V19E, K25D, Y29D, A31K. (Four additional mutations: K2S, D12G, T23A, N30S). Many non-native salt bridges formed in the simulations may keep residues involved in native contacts from finding each other. In Mutant2, four out of six mutated polar residues spent time making salt bridges with other charged residues. It is important to note that WT had more contacts on average than Mutant2, yet Mutant2 made greater number of native contacts. All these data indicates that there were no large structural changes in Mutant2.

Mutant3 was more rigid in our simulation than any other mutants. In particular, there was less fluctuation in the backbone as observed by lower C α RMSD and C α RMSF in Mutant3 relative to WT or other mutants at 37°C (Figure 4.4). Mutant3 only formed non-native forms of salt bridges, which may be a possible explanation for complete disappearance of secondary structure in MKC-A during MD simulation (Figure 4.4).

In case of Mutant4, hydrophobic surface residues on WT MKC were mutated to polar residues: K2S, Y3E, A10R, T15R, T17A, V19E, T23A, T36R, I37T, V39D, T40K, P42D. Since alanine and threonine side chains are generally non-reactive and rarely directly involved in protein function, we mutated those residues to arginine or lysine, introducing positive charges that could potentially be involved in forming salt-bridges. The additional H-bonds in Mutant4 helped stabilize the mutant and retain secondary structure.

In summary, we have investigated the dynamics of WT MKC and its engineered stabilized variants. We computationally designed MKC mutants that are more stable as a dimer and validated our MD simulation by expressing WT and Mutant1 MKC in a *Daedalus* mammalian system. Biochemical analysis (e.g., Size exclusion column, SDS-PAGE) of Mutant1 MKC showed great improvement in its stability as a dimer compared to WT MKC. According to MD simulation, Mutant2, 3, 4 have more favorable characteristics than Mutant1 (e.g., lower RMSD/F, greater native contact). Our goal is not only to design a more stable MKC dimer, but also a peptide that can inhibit the shared glypican pathway used by a variety of growth factors. Other biochemical properties (e.g., affinity toward heparan sulfate chain), tumor-homing effect (e.g., ability to cross blood-brain barrier, specificity toward tumor), and therapeutic implications (e.g., ability to kill cells) of computationally designed MKC mutants will need to be further investigated.

Materials and Methods

Expression Analysis

Microarray data from Zhao et al. (Zhao et al., 2012), Li et al. (Li et al., 2009) and Liu et al. (Liu et al., 2011) were obtained from Gene Expression Omnibus (accession no. GSE 28192, GSE14296, GSE21354). GSE28192 consists of normal fetal brain (n=4), adult cerebellum (n=5), and childhood cerebellum (n=1), and primary medulloblastoma tumors (n=12). GSE 14296 consists of normal fetal brain (n=7), normal adult brain (n=7), and primitive neuroectodermal tumors (n=55). GSE21354 consists of normal brain tissue sample (n=3) and grade II gliomas (n=14). GEO2R was used to perform R-based analysis of GEO data to identify differential gene expression (<http://www.ncbi.nlm.nih.gov/geo/geo2r>)

Immunohistochemistry

Tissues were cut into 4- μ m sections and immunostained with biotinylated primary antibody against glypican-2 (R&D Systems). Secondary antibody were applied according to Vectastain Elite avidinbiotin complex method instructions (Vector Laboratories), and detection was carried out with 3,3'-diaminobenzidine reagent (Vector Laboratories). Sections were visualized with Nikon E800 microscope.

Structure Preparation

The starting structure of wild-type (WT) human MK for MD simulations was modeled based on a NMR structure of C-terminal domain of human MK (MKC; PDB code 1MKC) (Iwasaki et al., 1997), which contains residues 84-126. The MKC structure were renumbered to align with numbering used in ilmm, and they are discussed using residues 1-43 instead of 84-126 to avoid confusion. The dimer form of MKC was manually created using Chimera software (www.cgl.ucsf.edu/chimera) by aligning two MKC monomers (MKC-A and MKC-B) based on proposed dimer model (Iwasaki et al., 1997). Automatic moves from Foldit software - combinatorial side-chain rotamer packing ('shake'), gradient-based minimization ('wiggle'), amino acid redesigning ('mutate') - are used to design new proteins. (Summary in Figure 4.4)

MD Simulation Protocol

All simulations were performed using MD software, *in lucem* molecular mechanics (ilmm). The simulations began from the crystal structure of midkine C-terminal domain (PDB ID: 1MKC). Minimization was performed using the force field for 1000 steps of steepest decent minimization. Each system was prepared as per our standard protocols (Beck and Daggett, 2004) using a water box that extended 10 Å past the edge of the protein on all sides filled with water molecules. The final water density of the system was adjusted to the experimentally measured density of 0.993 g/mL. All simulations of WT and mutant MDK proteins were performed at 310 K for 15 ns. Simulations included all hydrogen

atoms and used using 1.8 Å as the radius of exclusion for waters around solute. Two to three independent MD simulations were performed for WT and for each mutant.

Simulation Analysis

The root-mean-square deviation of the C α atoms (C α RMSD) to the simulation starting WT and mutants structure was calculated for the core residues of all proteins. The RMSD was also calculated between all structures and then averaged to give average core C α RMSD. The C α root-mean-square fluctuation (C α RMSF) about the mean structure over time was also calculated for the core residues. The mean structure for each protein was calculated by averaging the coordinates for each C α atom across simulation time.

Contacts were counted and classified in several different ways. First, contacts were defined as native or non-native based on whether they occurred in the starting structure. They were also classified based on whether the contacting atoms were in the main chain (N, C α , C, O) or side chain. Atoms were considered in contact for carbons that were ≤ 5.4 Å apart or non-carbon atoms that were ≤ 4.6 Å apart. Hydrogen atoms were not considered, nor were interactions within a residue or between neighboring residues. Residues were considered in contact if they contained at least one contacting atom pair. Furthermore, the secondary structures of protein were assessed using the Define Secondary Structure of Proteins (DSSP) program.

Expression of WT and Mutant1 MKC in mammalian cells

Mutant libraries were created using an oligonucleotide assembly approach. The assembly reactions were amplified with primers containing XhoI/BamHI sites and the purified PCR products were cloned into the Daedalus vector pCVL-sUCOE-SFFV-IRES-GFP (Bandaranayake et al., 2011). The resulting lentiviral library was used to transduce HEK 293 cells to create a polyclonal population of cells secreting variants. Each library consists of either the parental scaffold alone, containing an N-terminal secretion signal and a C-terminal STREPII tag, or the parental scaffold fused to a secretion partner (siderocalin). The secreted peptide fusions were harvested from the culture supernatants using size-exclusion chromatography (SEC) on a Superdex 75 column (GE Healthsciences). Proteins were detected by Coomassie blue staining of sodium dodecyl sulfate–polyacrylamide gel electrophoresis (SDS–PAGE).

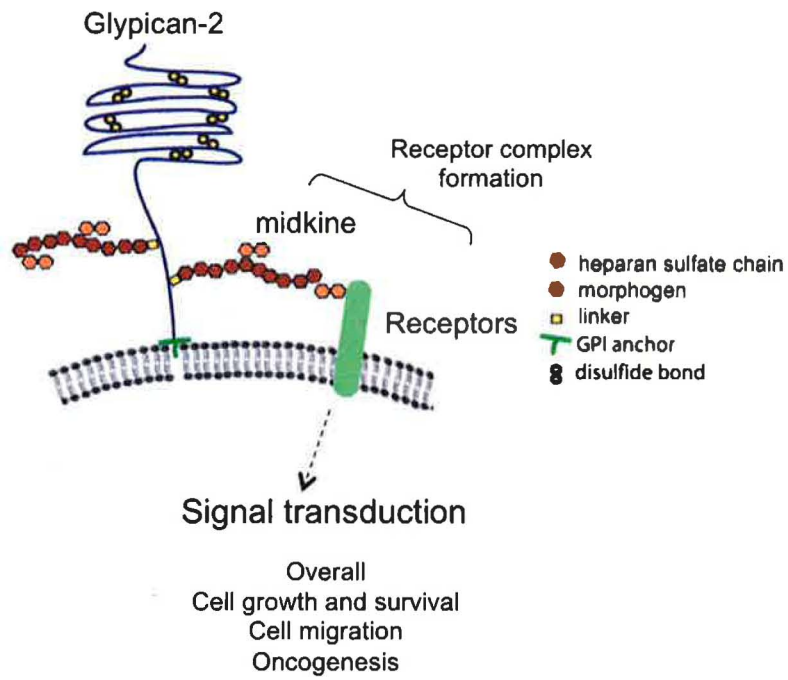


Figure 4.1 A proposed model of Glypican-2 and midkine action

Core protein of glypican-2 is decorated with long, charged polysaccharide heparin sulfate chains. Midkine, which acts as a dimer, binds to heparin sulfate chains and promotes the formation of the receptor complexes and regulates cell proliferation, differentiation and patterning.

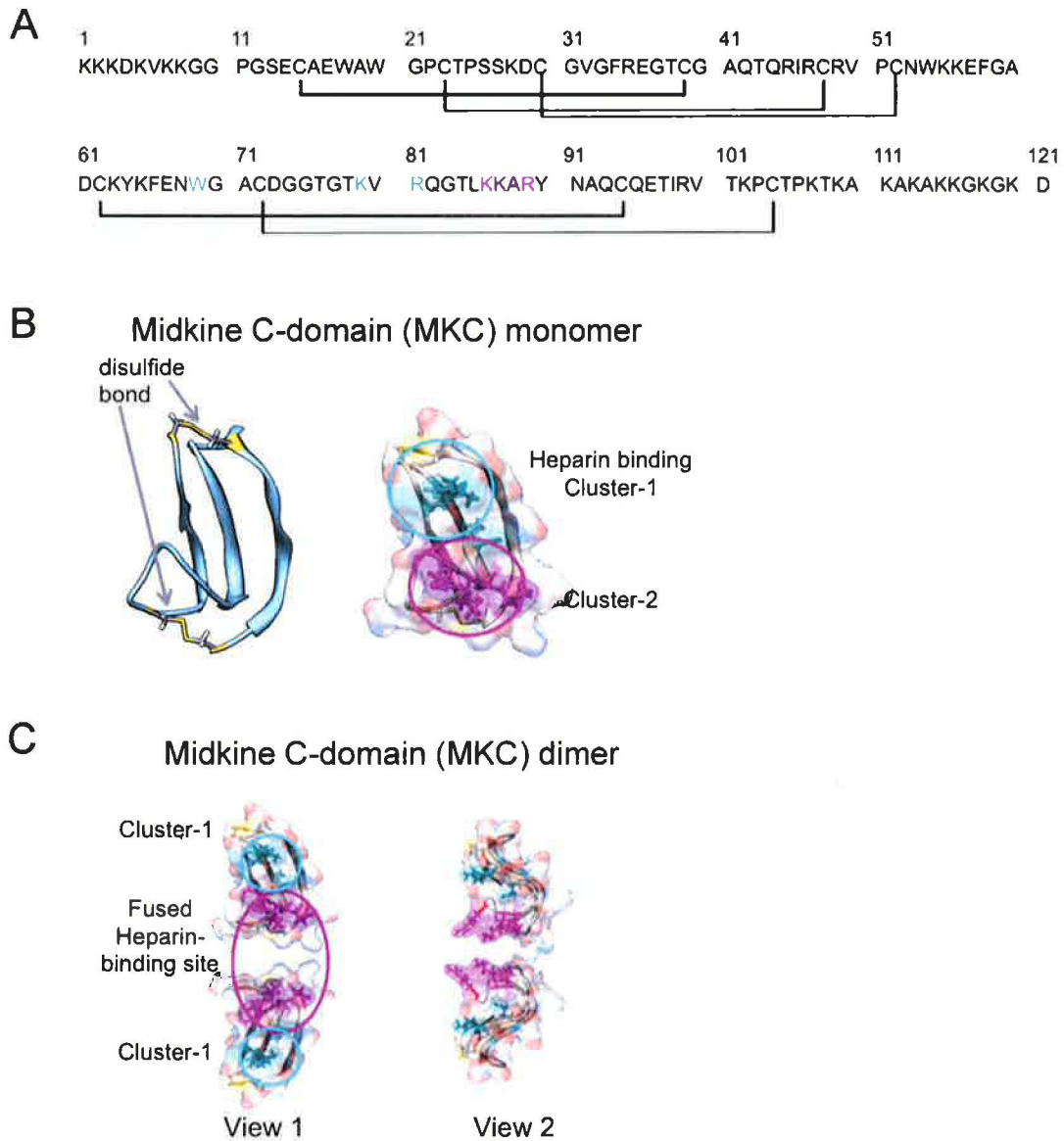


Figure 4.2 Midkine sequence and structure

(A) Primary structure of human midkine. Key amino acids involved in heparin binding (cyan, Cluster-1; magenta, Cluster-2). Lines show the position of disulfide linkages. (B) Two heparin-binding sites in the C-terminus domain are encircled. On the surface, red represents negatively charged elements, white represents neutral elements, and blue represents positively charged elements. (C) The model for midkine C-domain (62–104) head-to-head dimer complex is shown. Cluster-2s in the C-terminus domains form fused heparin-binding sites at the dimer interface. This fused heparin-binding sites fit to negatively charged clusters of heparin.

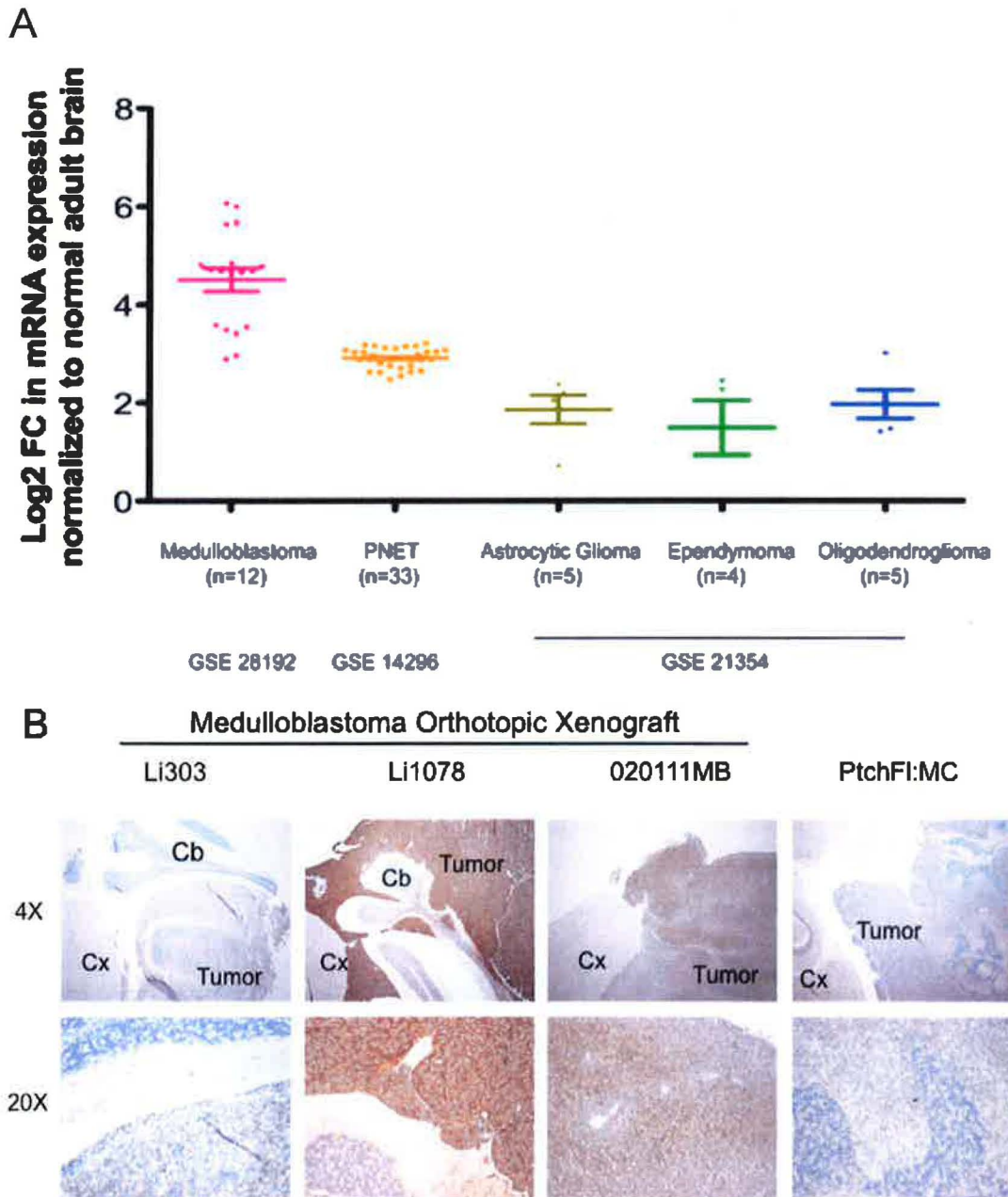


Figure 4.3 Expression of Glypican-2 in brain cancers

(A) mRNA expression of glypican-2 was calculated in five different types of brain cancer. Three different GEO datasets were used to analyze level of glypican-2 expression. (Expression level was normalized to normal adult brain; error bars = SEM). (B) The expression of glypican-2 in medulloblastoma cancer cells. Immunohistochemistry demonstrated that glypican-2 was highly expressed in human medulloblastoma orthotopic xenografts and genetically engineered medulloblastoma mouse but absent in adjacent non-tumorous normal tissues. (Cx: normal brain; Cb: normal cerebellum)

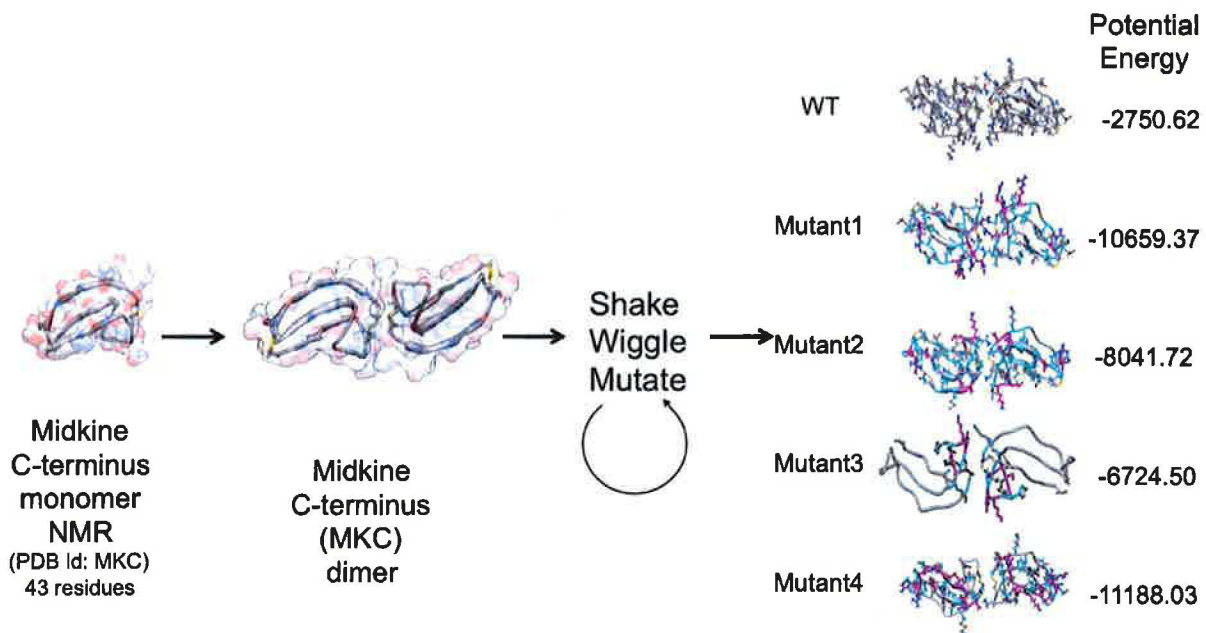


Figure 4.4 Designing MKC peptide variants

NMR structure of C-terminus domain of midkine was obtained from Protein Data Bank (PDB) and dimer form was generated. Using Foldit, the sequence and conformation of a protein were optimized to find low-energy sequence-structure pairs.

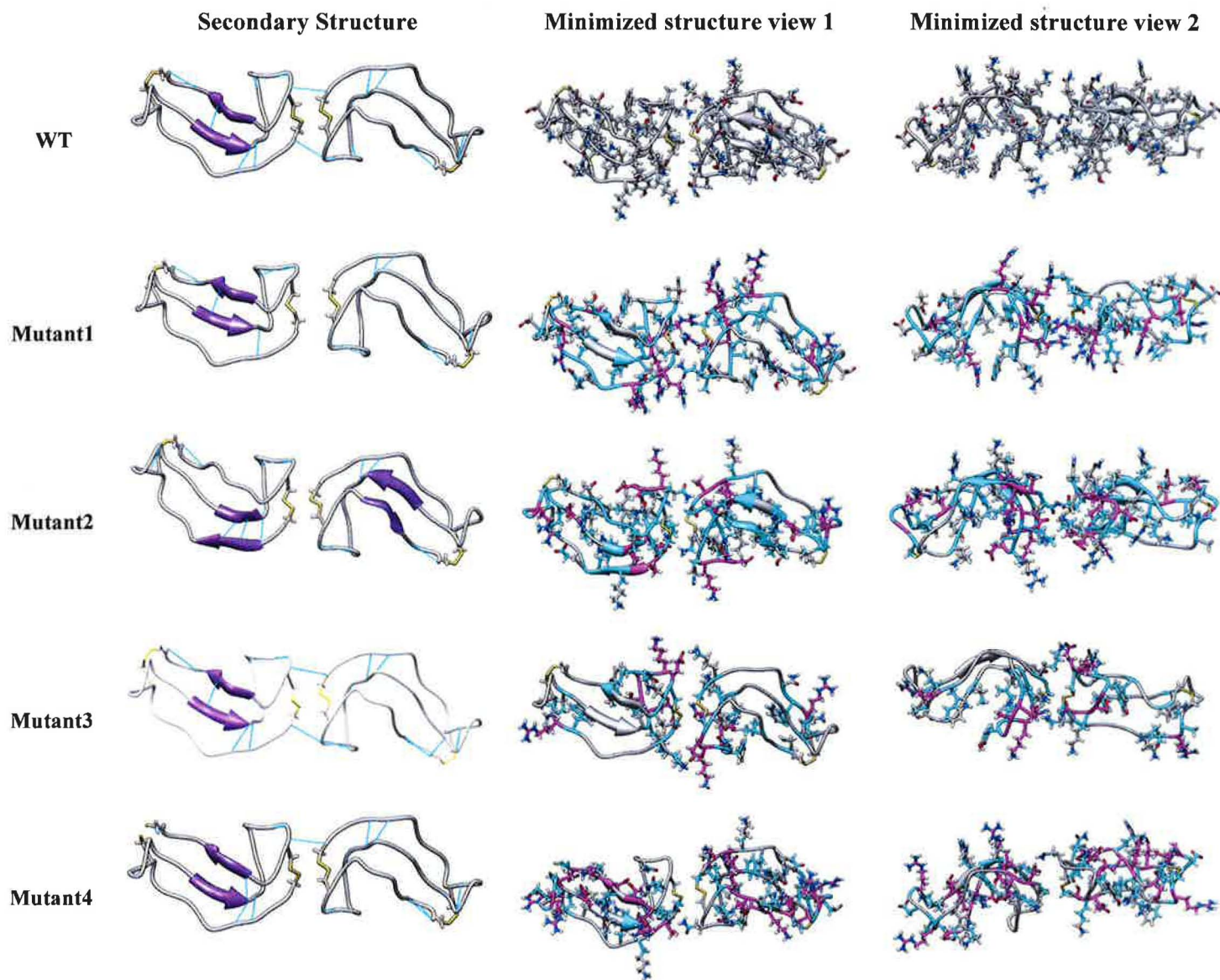


Figure 4.5 3D structures of WT and four MKC mutant dimers

(Left column) Secondary structure of minimized WT and mutant MDK dimers are shown. Disulfide bonds are colored in yellow and H-bonds are colored in cyan. (Middle and right column) All residues within 4 Å of mutation sites are colored in cyan. Mutation sites are shown in magenta.

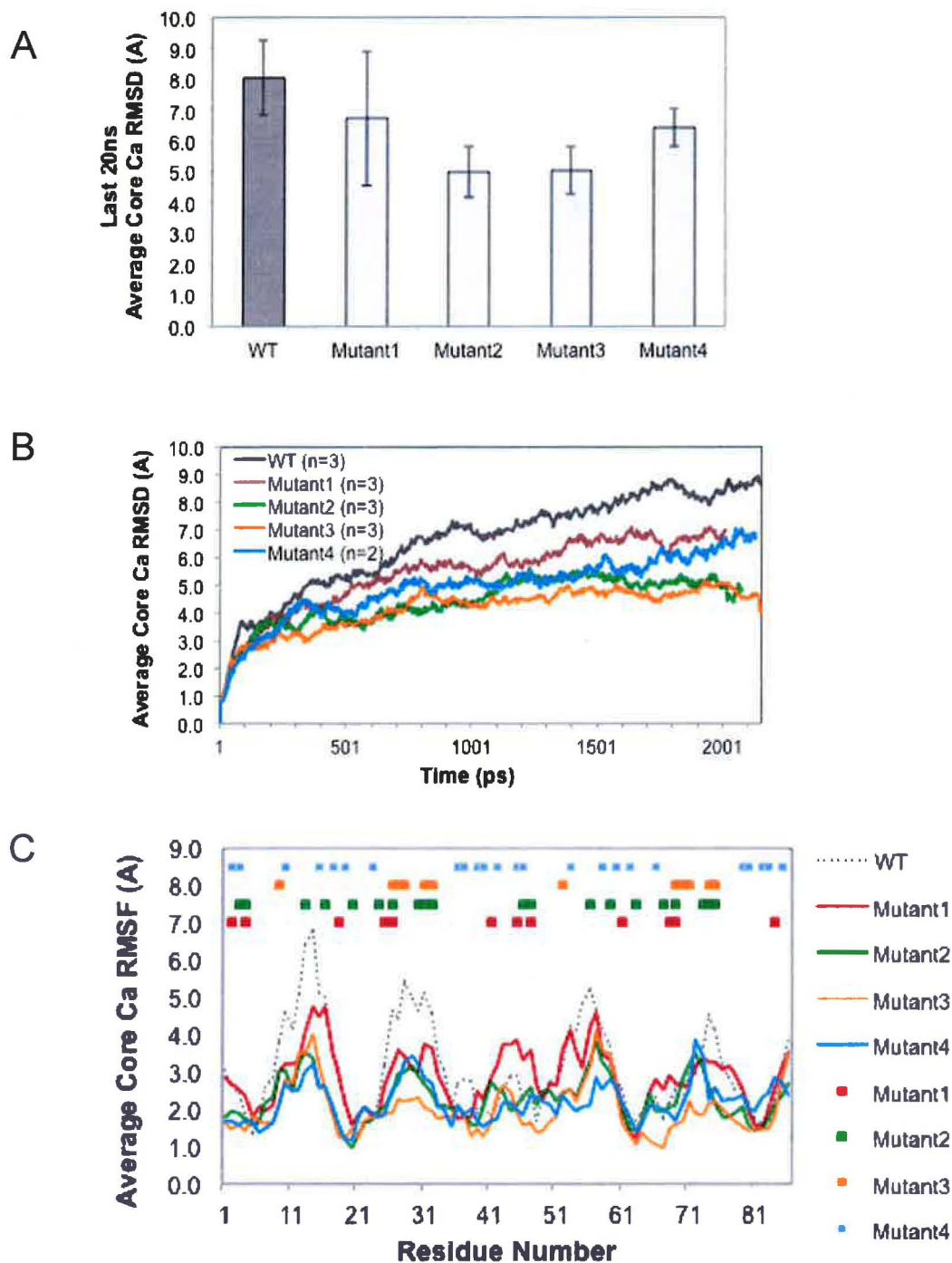


Figure 4.6 Core $\text{C}\alpha$ RMSD/F in MD simulations

(A) The average $\text{C}\alpha$ RMSD of the core residues over the last 20ns of each of the two to three independent simulations is plotted for WT and mutant MKC with the standard deviation denoted by error bars. (B) The core $\text{C}\alpha$ RMSD was averaged at each time point over the independent simulations and is plotted over time for WT and mutant MKC. (C) The core $\text{C}\alpha$ RMSF is plotted for each residue in WT and mutant MKC.

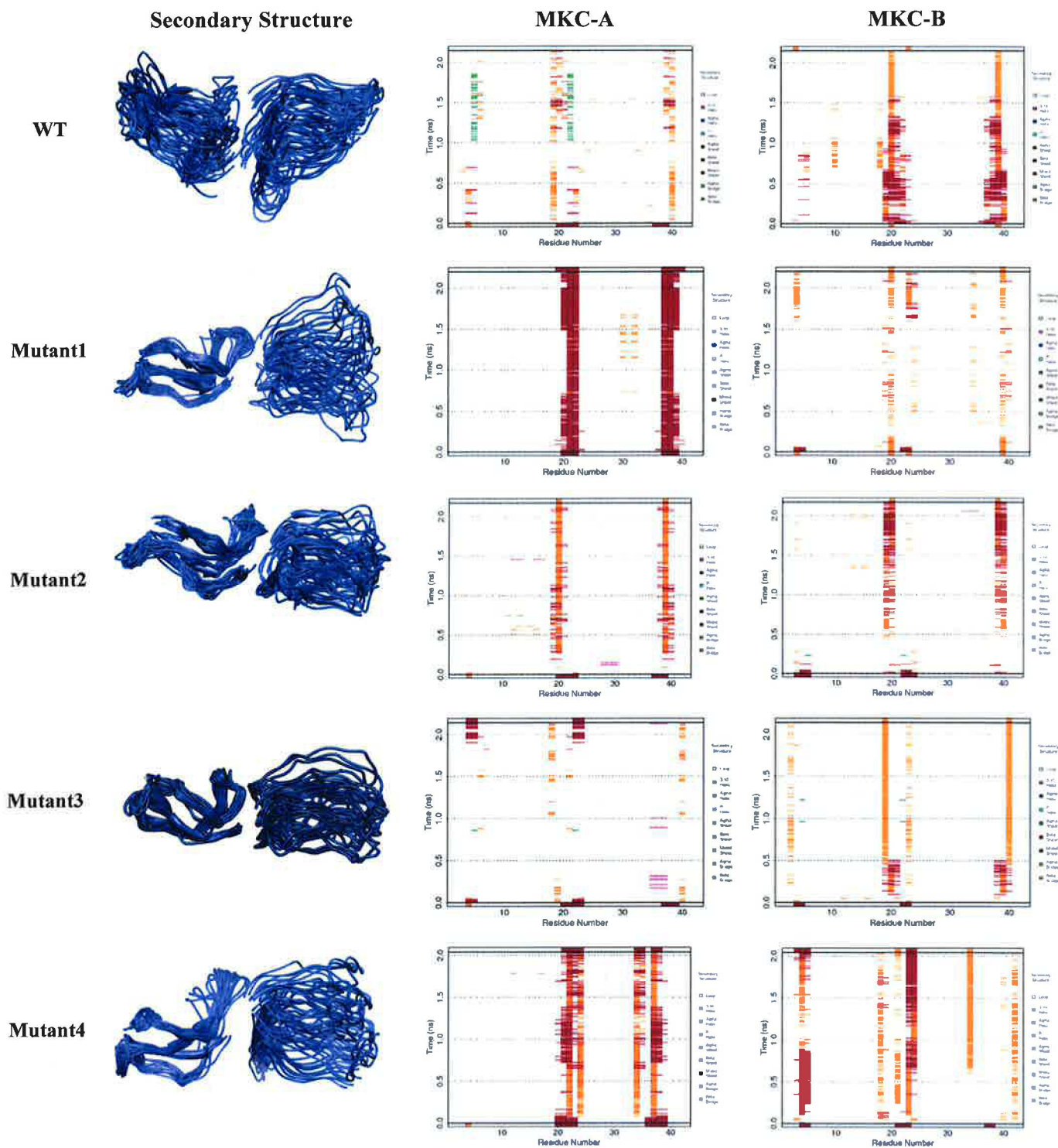


Figure 4.7 Backbone mobility in WT, and four mutant MKC dimers

(Left column) The 15-ns structures from the MD simulations at 37°C overlaid and aligned. Mutant3 was the least mobile among all. (Middle and right column) MD dssp analysis of WT and mutant dimers. (white: loop; red: β -sheet; orange: β -bridge; green: α -bridge; pink: 3/10 helix)

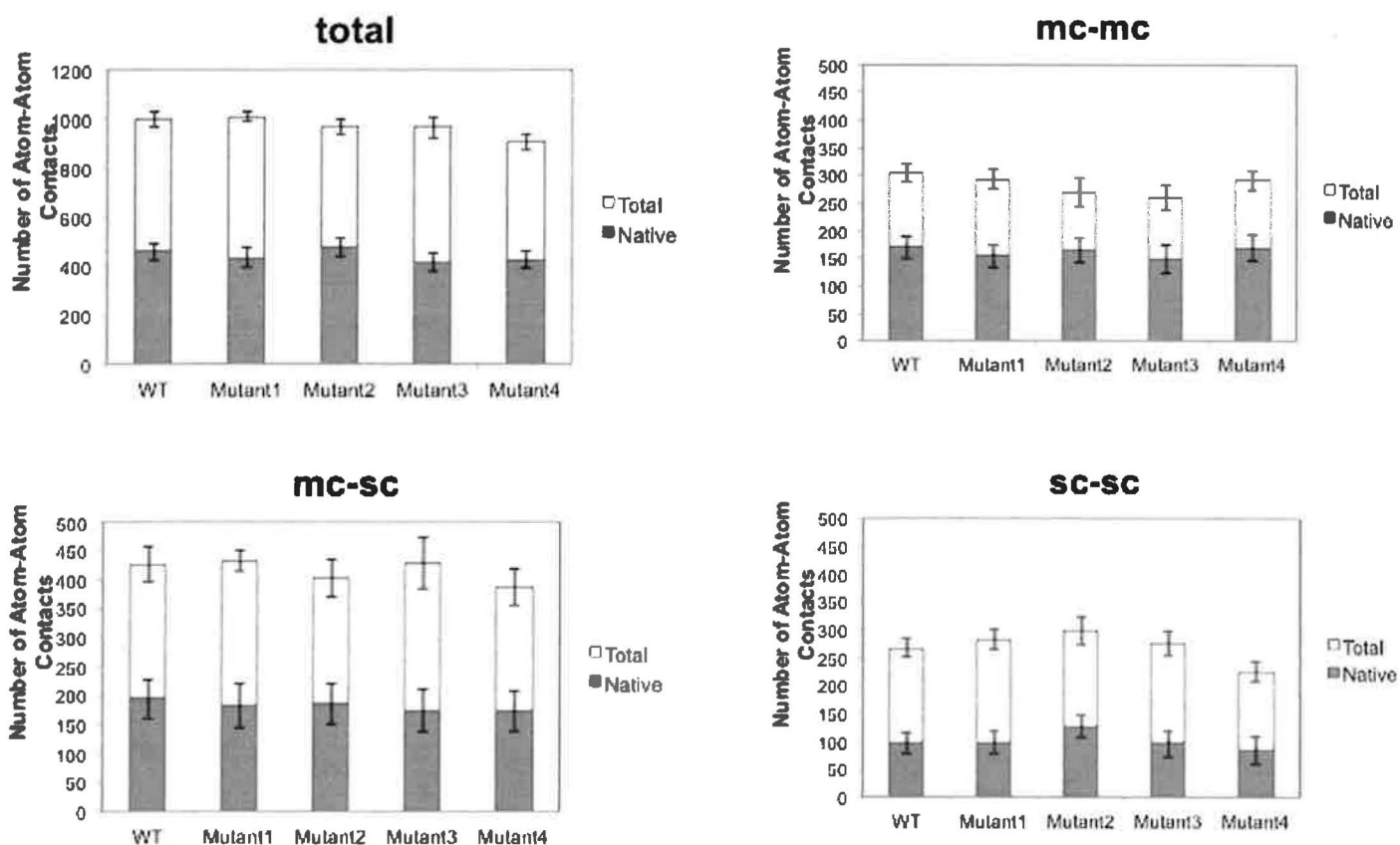


Figure 4.8 Main chain and side chain contact analysis during MD simulation

Total number of contacts for the core residues of WT and four mutant MKC dimers are plotted. The solid portion of the bar indicates native contacts and white portion indicates non-native contacts. (error bars = s.d over time). Contacts are classified as main chain- main chain (mc-ms), main chain-side chain (mc-sc), side chain-side chain (sc-sc), and total.

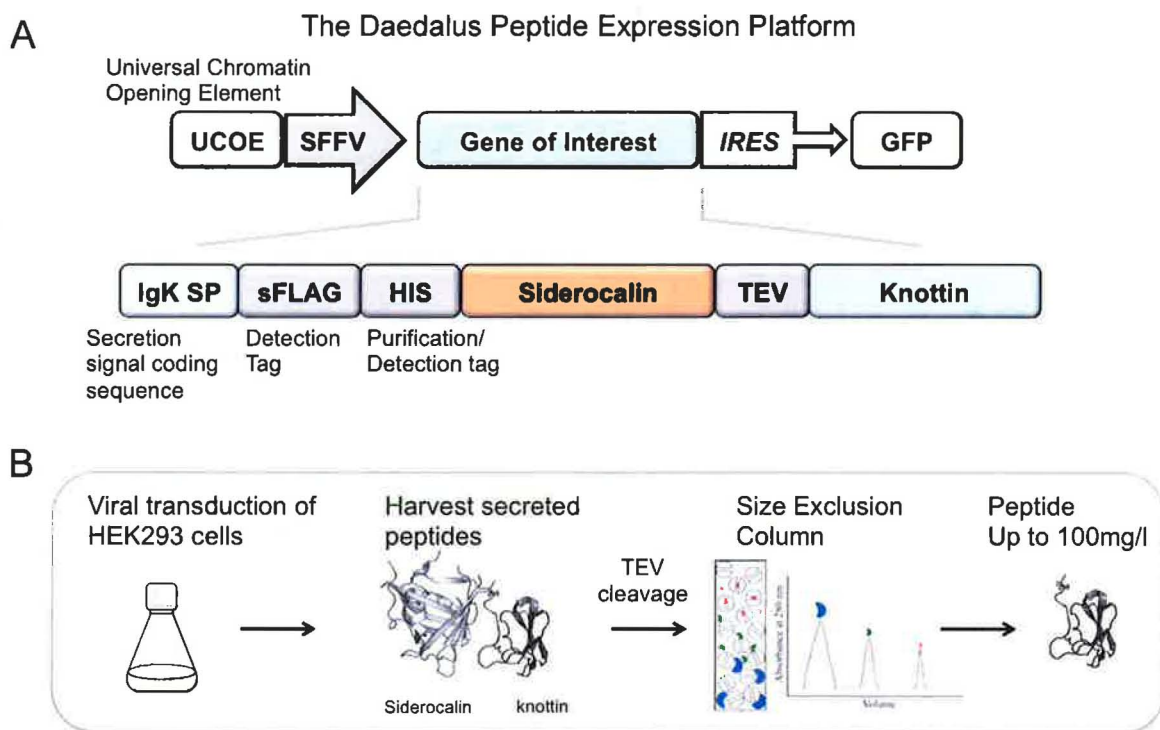


Figure 4.9 Expressing knottin proteins using Daedalus platform

(A) Daedalus platform is based on the use of lentiviral vectors that contains a minimized UCOE element, which allows for the high level expression of a particular gene. Siderocalin is used as a fusion partner to enable recovery of secreted free knottin peptide in the media. (B) Daedalus lentiviral vector is used to transduce HEK 293 cells. The secreted peptides are harvested from the culture supernatants. Treatment with TEV protease cuts and release knottin protein of interest from the fusion partner and naked peptides are purified in a single size exclusion step.

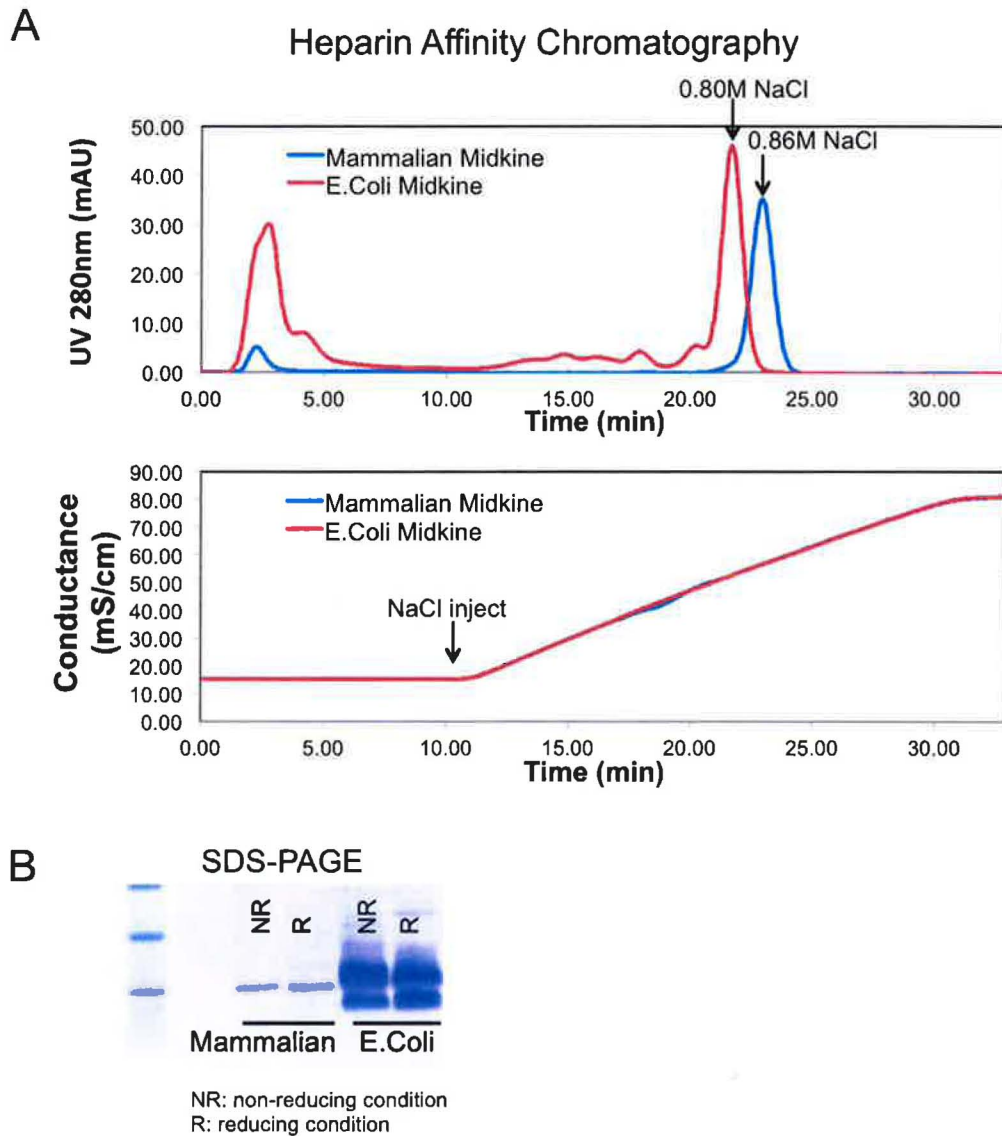


Figure 4.10 Biochemical characteristics of E.Coli and Mammalian WT MKC

(A) Heparin affinity column of E.Coli and mammalian MKC. Binding of the E.Coli and mammalian MKC WT proteins was assayed by heparin affinity chromatography. Proteins were applied to a heparin column, and after extensive washing, bound proteins were eluted using a linear salt gradient (0.0-1.0M NaCl). Mammalian MKC showed stronger binding affinity toward heparin. (2) SDS-PAGE revealed that Mammalian MKC was properly folded, but E.Coli MKC was not. (NR: non-reducing condition, R: reducing condition)

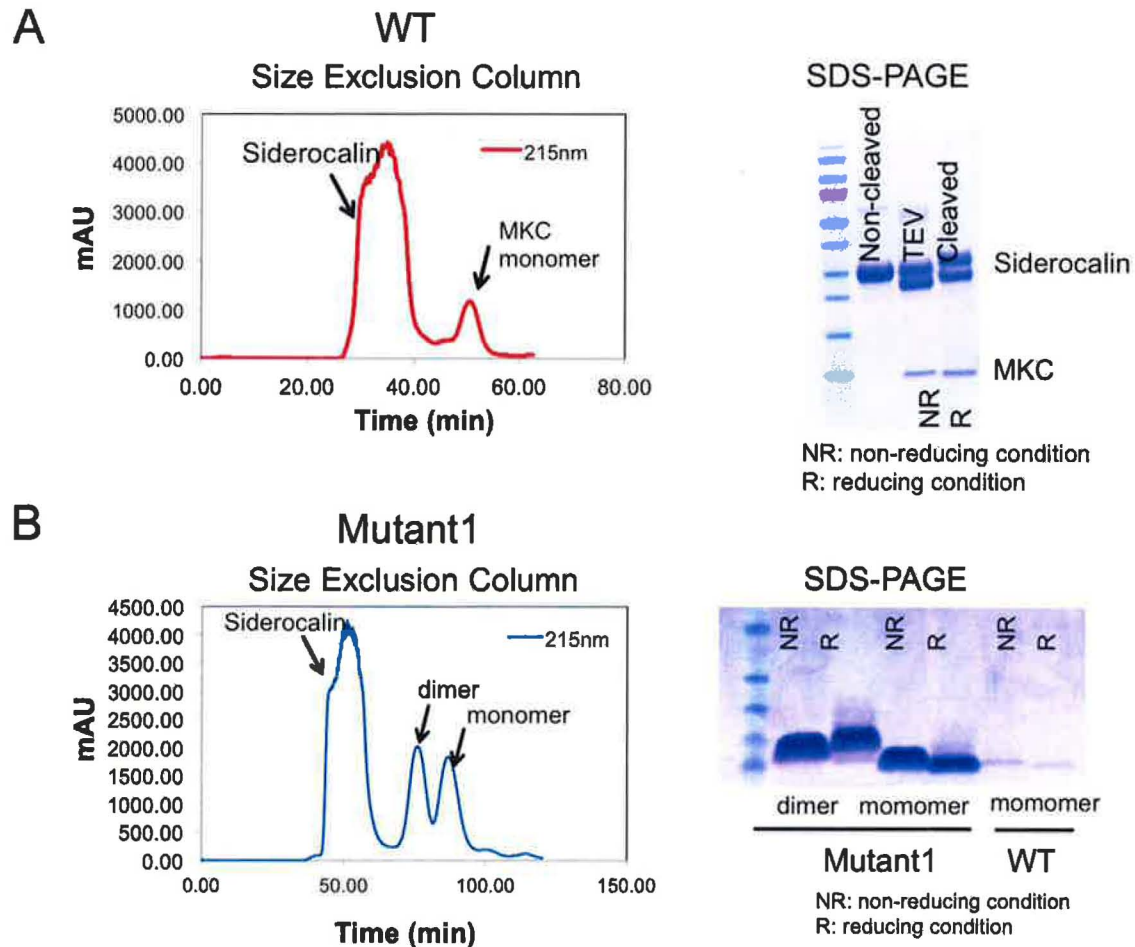


Figure 4.11 Biochemical characteristics of WT and Mutant1 mammalian MKC

(A) Size Exclusion Column analysis (SEC) and SDS-PAGE gel of WT MKC released from Siderocalin after TEV cleavage reaction. On SEC, WT MKC eluted as a single, monodisperse peak, which is an indication of structural homogeneity of the sample. By SDS-PAGE, TEV cleaved protein yielded a single band. (B) SEC analysis showed both dimer and monomer forms of Mutant1 mammalian MKC. SDS-PAGE analysis of these two SEC peaks confirmed the presence of dimers and monomers. (NR: non-reducing condition, R: reducing condition)

Name	Original Designation	Expression in Embryo	Expression in Adult
Glypican-1		Bone, bone marrow, muscle epidermis, kidney	Most tissues
Glypican-2	Cerebroglycan	Nervous system	Not detected
Glypican-3	OCI-5	Most tissues	Ovary, mammary gland, lung, kidney
Glypican-4	K-glypican	Brain, lung, lung	Most tissues
Glypican-5		Brain, lung, liver, kidney, limb	Brain
Glypican-6		Many tissues, including liver and kidney	Many tissues including ovary, kidney, liver, and intestine

Table 4.1 Glypican family during embryogenesis and in adult tissues

(Adapted from Fico et al., 2007)

	Description	Sequence	Potential Energy	H bonds found
WT		CKYKFENWGACDGGTGTKVRQGTLKKARYNAQC QETIRVTKPC	-2750.62	58
Mutant 1	Lys to Arg	CR Y R F ENWGACDGGTGT R VRQGTL RR ARYNAQCQ ETIRV T R P C	-10659.37	58
Mutant 2	Introduction of more negatively charged (e.g., Aspartate) or positively charged (e.g., Arginine) to create stabilizing H bonds	CS R K F ENWGAC G G G R G TK E R Q G A L D K A R D S K QCQ ETIRVTKPC	-8041.72	53
Mutant 3	Mutation in dimer linker regions	CKYKFENW R ACDGGTGTKVRQGTL K N S G Y N K E CQ ETIRVTKPC	-6724.50	59
Mutant 4	Mutation on the opposite side of heparin binding regions	C S E K FENW G R C D G G R G A K E R Q G A L K KARYNAQC Q E R T R D K K D C	-11188.03	67

Table 4.2 Detailed description of WT and four MKC mutants

The amino acid sequences, description of mutation, potential energy, and number of H-bonds of WT and four MKC proteins. Any residue that is different from WT is marked red.

	Basic residues	Acidic residues	% of basic and acidic residues	Salt bridge formed
WT	3 Arg, 6 Lys	2 Glu, 1 Asp	27.9% (12 of 43 residues)	**Lys2-Glu35 nn, **Lys4-Glu6 nn, Lys18-Glu6 n, Lys18-Asp12 nn, **Arg20-Glu6 nn,
Mutant1	9 Arg, 0 Lys	2 Glu, 1 Asp	27.9% (12 of 43 residues)	Arg2-Glu35 n , Arg4-Glu6 nn, *Arg18-Glu6 nn, Arg18-Asp12 n, **Arg20-Glu6 n, Arg38-Glu35 nn,
Mutant2	5 Arg, 5 Lys	3 Glu, 2 Asp	34.88% (15 of 43 residues)	**Arg3-Asp25 n, **Lys4-Glu6 nn, *Arg15-Glu6 n, Arg15-Glu80 n, Lys18-Glu6 nn, **Arg20-Glu6 both n, nn, Arg38-Glu19 both n, nn, Arg38-Glu35 nn,
Mutant3	3 Arg, 6 Lys	3 Glu, 1 Asp	30.23% (13 of 43 residues)	Lys4-Glu35 nn, Arg9-Glu6 nn, Lys18-Glu6 nn, **Arg20-Glu6 nn, *Arg18-Asp12 both n,nn,
Mutant4	6 Arg, 6 Lys	4 Glu, 2 Asp	41.86% (18 of 43 residues)	Arg10-Asp42 nn, **Arg15-Glu6 n, **Arg15-Asp12 n, **Arg15-Glu19 n, Lys18-Glu67 nn, Arg20-Asp39 n, **Lys25-Glu3 nn, Arg28-Glu3 nn, Arg38-Glu19 nn, **Arg38-Lys40 n, **Lys40-Glu19 nn, Lys41-Glu19 nn, **Lys41-Asp39 n

Table 4.3 Analysis of charged residues and salt bridges formed in WT and mutant MKC

Green: contacts new in mutants; n:native contact; nn: non-native contact; *: high number of contact; **: greater than 95% contact, *: greater than 75% contact

CHAPTER 5

Conclusion and Future Directions

Tumor imaging studies

In the current clinical practice, the intraoperative assessment of the tumor-free margin is dependent on visual appearance and palpation of the tumor. NIRF Intraoperative optical imaging has the potential of closing the gap between radiology and surgery by providing real-time visualization of the tumor. However, there remain considerable challenges bringing NIRF nanoprobe technology to clinical practice. First, stability and dispensability of nanoprobe in physiological environments and biochemical properties of nanoprobe might produce unexpected result *in vivo*. Therefore the pharmacokinetics and toxicity of the nanoprobe should be investigated in parallel with their tumor-imaging potential and unfavorable biodistribution such as nonspecific accumulation in reticuloendothelial system (RES) needs to be resolved. Second, further innovations are necessary to generate NIRF nanoprobe with high quantum yield and greater tissue penetration. Currently, indocyanine green (ICG) is the only fluorophore approved by the Food and Drug Administration (FDA). Further development and FDA approval of other organic fluorophores is essential. Third, parallel development of intraoperative surgical microscope, CCA cameras, or endoscopes is required. Existing imaging systems such as surgical microscopes (Zeiss, Olympus) and SPY imaging system daVinci Robots (Intuitive Surgical Inc.) are capable of imaging ICG in real time. Next generation device will improve on imaging in ambient light condition, higher resolution, and subtraction of background signal. Further research is in absolute need to develop more sensitive NIR camera system and to correct the measured fluorescence signal for scattering and absorption. Although the practical clinical application of NIRF nanoparobes has many challenges to be overcome, continued collaborations among the interdisciplinary research teams will speed up the translation process. The NIRF nanoprobe for real-time imaging-guided surgery holds promising possibilities for clinical use in the years to come.

Shh-targeted therapy in medulloblastoma studies

Human tumors have great genetic diversity, as revealed by gene-expression profiling. One of the major challenges in the use of Smo inhibitors for treating medulloblastoma is identification of patients who are capable of responding. Although genetic testing can reveal the presence of Ptch1 mutations, this could only account for a subset of patients (Only 30% of medulloblastoma patients have activated Shh pathway and less than 50% of those patients have *Path1* mutations). In addition, the mutation status of Smo as well as genes acting downstream of Smo needs to be evaluated. Clearly, improved understanding

of the mechanism of action of Smo inhibitors will help to broaden the usefulness of such agents. Development of robust criteria for the stratification of patients will also be very important for selecting the patients who would most likely benefit from Shh-targeted therapy.

Despite the promising clinical results, early reports indicate that patients being treated with Smo inhibitors in clinical trials eventually developed resistance via number of mechanisms, involving mutations of the target genes, overexpression of drug transporters, or upregulation of signaling pathways that interact with Shh. In case of saridegib, Pgp drug transporters were overexpressed in drug resistant medulloblastoma tumors and resistance was partially reversed by co-treatment with Pgp inhibitor verapamil. Efforts to improve drug uptake with Pgp inhibitors in animal models have shown limited success. Yet, clinical use of Pgp inhibitors, like verapamil, was hampered by the potential for adverse effects at concentrations necessary to sufficiently inhibit the drug efflux proteins. Furthermore, Pgps play a key role in protecting noncancerous tissue from chemotherapy damage. These results suggest the need for additional research in two areas: the first is to continue to explore the physiological roles of ABC transporters, and the second is to continue to investigate novel mechanisms of drug resistance. Future studies examining the function of ABC transporters beyond drug efflux could not only raise awareness of potential adverse effects, but also identify new therapeutic targets. Given the functional redundancy observed for ABC transporters, combination therapy of ABC inhibitors may be explored to effectively inhibit given transporter function.

Peptide-based targeted therapy studies

Through my studies described in Chapter 4, I have computationally designed four variants of MKC and successfully expressed WT and one of the MKC mutants. The next steps are first, to express a larger library of MKC variants using the Daedalus system. Second, to identify the top five MKC candidates that demonstrate highest binding affinity for glypican-2. Cell viability assays will be conducted to identify MKC variants that differentially affect glypican-2-dependent medulloblastoma cell lines. For those MKC variants that cause decreased cell viability, *in vitro* assays will be conducted to determine whether binding of the peptides results in functional inactivation of pathways that are linked to glypican-2 (e.g., integrin and/or protein-tyrosine phosphatase pathways). The lead candidates that emerge from the functional *in vitro* assays will be advanced to *in vivo* studies. Third, three MKC candidates that demonstrate highest efficacy *in vitro* will be administered systemically to Ptc^{C/C} medulloblastoma mice to assess their ability to target to tumor and penetrate the blood-brain barrier at various time-points. The efficacy of the lead MKC variants will be tested in mice bearing patient-derived medulloblastoma orthotopic xenografts. These studies will assess the pharmacokinetics of the candidate peptide as well as its ability to engage target and inhibit tumor growth. A definitive preclinical trial will then be performed

in which mouse survival is the primary end-point. Although the therapeutic potentials of MKC variants need to be further investigated, the foundational studies performed here may provide the first insights into the use of cysteine knot peptide variants in mammalian systems and may serve as an important step towards integrating knottin drugs into mainstream therapy.

References

- Adamson, D.C., Shi, Q., Wortham, M., Northcott, P.A., Di, C., Duncan, C.G., Li, J., McLendon, R.E., Bigner, D.D., Taylor, M.D., *et al.* (2010). OTX2 is critical for the maintenance and progression of Shh-independent medulloblastomas. *Cancer Res* 70, 181-191.
- Adolphe, C., Hetherington, R., Ellis, T., and Wainwright, B. (2006). Patched1 functions as a gatekeeper by promoting cell cycle progression. *Cancer Res* 66, 2081-2088.
- Afratis, N., Gialeli, C., Nikitovic, D., Tsegenidis, T., Karousou, E., Theocharis, A.D., Pavao, M.S., Tzanakakis, G.N., and Karamanos, N.K. (2012). Glycosaminoglycans: key players in cancer cell biology and treatment. *Febs J* 279, 1177-1197.
- Aikawa, T., Whipple, C.A., Lopez, M.E., Gunn, J., Young, A., Lander, A.D., and Korc, M. (2008). Glypican-1 modulates the angiogenic and metastatic potential of human and mouse cancer cells. *J Clin Invest* 118, 89-99.
- Akhter, S., Ichihara-Tanaka, K., Kojima, S., Muramatsu, H., Inui, T., Kimura, T., Kaneda, N., Talukder, A.H., Kadomatsu, K., Inagaki, F., *et al.* (1998). Clusters of basic amino acids in midkine: roles in neurite-promoting activity and plasminogen activator-enhancing activity. *J Biochem* 123, 1127-1136.
- Alexis, F., Pridgen, E., Molnar, L.K., and Farokhzad, O.C. (2008). Factors affecting the clearance and biodistribution of polymeric nanoparticles. *Mol Pharm* 5, 505-515.
- Amaral, M.D., Clarke, L.A., Ramalho, A.S., Beck, S., Broackes-Carter, F., Rowntree, R., Mouchel, N., Williams, S.H., Harris, A., Tzetzis, M., *et al.* (2004). Quantitative methods for the analysis of CFTR transcripts/splicing variants. *J Cyst Fibros* 3 Suppl 2, 17-23.
- Amin, S.H., Tibes, R., Kim, J.E., and Hybarger, C.P. (2010). Hedgehog antagonist GDC-0449 is effective in the treatment of advanced basal cell carcinoma. *Laryngoscope* 120, 2456-2459.
- Andersen, B.B., Korbo, L., and Pakkenberg, B. (1992). A quantitative study of the human cerebellum with unbiased stereological techniques. *J Comp Neurol* 326, 549-560.
- Bandaranayake, A.D., Correnti, C., Ryu, B.Y., Brault, M., Strong, R.K., and Rawlings, D.J. (2011). Daedalus: a robust, turnkey platform for rapid production of decigram quantities of active recombinant proteins in human cell lines using novel lentiviral vectors. *Nucleic Acids Res* 39, e143.
- Beck, D.A., and Daggett, V. (2004). Methods for molecular dynamics simulations of protein folding/unfolding in solution. *Methods* 34, 112-120.
- Becker, A., Epple, M., Muller, K.M., and Schmitz, I. (2004). A comparative study of clinically well-characterized human atherosclerotic plaques with histological, chemical, and ultrastructural methods. *J Inorg Biochem* 98, 2032-2038.
- Becker, J.B., Arnold, A.P., Berkley, K.J., Blaustein, J.D., Eckel, L.A., Hampson, E., Herman, J.P., Marts, S., Sadee, W., Steiner, M., *et al.* (2005). Strategies and methods for research on sex differences in brain and behavior. *Endocrinology* 146, 1650-1673.

- Brugieres, L., Pierron, G., Chompret, A., Paillerets, B.B., Di Rocco, F., Varlet, P., Pierre-Kahn, A., Caron, O., Grill, J., and Delattre, O. (2010). Incomplete penetrance of the predisposition to medulloblastoma associated with germ-line *SUFU* mutations. *J Med Genet* 47, 142-144.
- Bryden, M.M., Evans, H.E., and Keeler, R.F. (1971). Cyclopia in sheep caused by plant teratogens. *J Anat* 110, 507.
- Bunt, J., de Haas, T.G., Hasselt, N.E., Zwijnenburg, D.A., Koster, J., Versteeg, R., and Kool, M. (2010). Regulation of cell cycle genes and induction of senescence by overexpression of *OTX2* in medulloblastoma cell lines. *Mol Cancer Res* 8, 1344-1357.
- Buonamici, S., Williams, J., Morrissey, M., Wang, A., Guo, R., Vattay, A., Hsiao, K., Yuan, J., Green, J., Ospina, B., *et al.* (2010). Interfering with resistance to smoothed antagonists by inhibition of the PI3K pathway in medulloblastoma. *Sci Transl Med* 2, 51ra70.
- Chen, J.K., Taipale, J., Cooper, M.K., and Beachy, P.A. (2002). Inhibition of Hedgehog signaling by direct binding of cyclopamine to Smoothed. *Genes Dev* 16, 2743-2748.
- Cho, Y.J., Tsherniak, A., Tamayo, P., Santagata, S., Ligon, A., Greulich, H., Berhoukim, R., Amani, V., Goumnerova, L., Eberhart, C.G., *et al.* (2011). Integrative genomic analysis of medulloblastoma identifies a molecular subgroup that drives poor clinical outcome. *J Clin Oncol* 29, 1424-1430.
- Corrales, J.D., Blaess, S., Mahoney, E.M., and Joyner, A.L. (2006). The level of sonic hedgehog signaling regulates the complexity of cerebellar foliation. *Development* 133, 1811-1821.
- David, G., Lories, V., Decock, B., Marynen, P., Cassiman, J.J., and Van den Berghe, H. (1990). Molecular cloning of a phosphatidylinositol-anchored membrane heparan sulfate proteoglycan from human lung fibroblasts. *J Cell Biol* 111, 3165-3176.
- Di, C., Liao, S., Adamson, D.C., Parrett, T.J., Broderick, D.K., Shi, Q., Lengauer, C., Cummins, J.M., Velculescu, V.E., Fuhs, D.W., *et al.* (2005). Identification of *OTX2* as a medulloblastoma oncogene whose product can be targeted by all-trans retinoic acid. *Cancer Res* 65, 919-924.
- Dijkgraaf, G.J., Alicke, B., Weinmann, L., Januario, T., West, K., Modrusan, Z., Burdick, D., Goldsmith, R., Robarge, K., Sutherlin, D., *et al.* (2010). Small molecule inhibition of GDC-0449 refractory Smoothed mutants and downstream mechanisms of drug resistance. *Cancer Res*.
- Dijkgraaf, G.J., Alicke, B., Weinmann, L., Januario, T., West, K., Modrusan, Z., Burdick, D., Goldsmith, R., Robarge, K., Sutherlin, D., *et al.* (2011). Small molecule inhibition of GDC-0449 refractory smoothed mutants and downstream mechanisms of drug resistance. *Cancer Res* 71, 435-444.
- Doggrell, S.A. (2010). The hedgehog pathway inhibitor GDC-0449 shows potential in skin and other cancers. *Expert Opin Investig Drugs* 19, 451-454.
- Doniach, S., and Eastman, P. (1999). Protein dynamics simulations from nanoseconds to microseconds. *Curr Opin Struct Biol* 9, 157-163.
- Ellison, D.W., Kocak, M., Dalton, J., Megahed, H., Lusher, M.E., Ryan, S.L., Zhao, W., Nicholson, S.L., Taylor, R.E., Bailey, S., *et al.* (2011). Definition of disease-risk stratification groups in childhood medulloblastoma using combined clinical, pathologic, and molecular variables. *J Clin Oncol* 29, 1400-1407.

- Emerich, D.F., and Thanos, C.G. (2006). The pinpoint promise of nanoparticle-based drug delivery and molecular diagnosis. *Biomol Eng* 23, 171-184.
- Fabri, L., Maruta, H., Muramatsu, H., Muramatsu, T., Simpson, R.J., Burgess, A.W., and Nice, E.C. (1993). Structural characterisation of native and recombinant forms of the neurotrophic cytokine MK. *J Chromatogr* 646, 213-225.
- Fairweather, J.K., Hammond, E., Johnstone, K.D., and Ferro, V. (2008). Synthesis and heparanase inhibitory activity of sulfated manooligosaccharides related to the antiangiogenic agent PI-88. *Bioorg Med Chem* 16, 699-709.
- Fang, C., Bhattarai, N., Sun, C., and Zhang, M. (2009). Functionalized nanoparticles with long-term stability in biological media. *Small* 5, 1637-1641.
- Ferrari, M. (2005). Cancer nanotechnology: opportunities and challenges. *Nat Rev Cancer* 5, 161-171.
- Ferro, V., Dredge, K., Liu, L., Hammond, E., Bytheway, I., Li, C., Johnstone, K., Karoli, T., Davis, K., Copeman, E., *et al.* (2007). PI-88 and novel heparan sulfate mimetics inhibit angiogenesis. *Semin Thromb Hemost* 33, 557-568.
- Galisteo, M.L., Yang, Y., Urena, J., and Schlessinger, J. (2006). Activation of the nonreceptor protein tyrosine kinase Ack by multiple extracellular stimuli. *Proc Natl Acad Sci U S A* 103, 9796-9801.
- Hatten, M.E., and Roussel, M.F. (2011). Development and cancer of the cerebellum. *Trends Neurosci* 34, 134-142.
- Hermano, E., Lerner, I., and Elkin, M. (2012). Heparanase enzyme in chronic inflammatory bowel disease and colon cancer. *Cell Mol Life Sci* 69, 2501-2513.
- Ilan, N., Elkin, M., and Vlodavsky, I. (2006). Regulation, function and clinical significance of heparanase in cancer metastasis and angiogenesis. *Int J Biochem Cell Biol* 38, 2018-2039.
- Iwasaki, W., Nagata, K., Hatanaka, H., Inui, T., Kimura, T., Muramatsu, T., Yoshida, K., Tasumi, M., and Inagaki, F. (1997). Solution structure of midkine, a new heparin-binding growth factor. *Embo J* 16, 6936-6946.
- Jen, Y.H., Musacchio, M., and Lander, A.D. (2009). Glypican-1 controls brain size through regulation of fibroblast growth factor signaling in early neurogenesis. *Neural Dev* 4, 33.
- Johnson, R.L., Rothman, A.L., Xie, J., Goodrich, L.V., Bare, J.W., Bonifas, J.M., Quinn, A.G., Myers, R.M., Cox, D.R., Epstein, E.H., Jr., *et al.* (1996). Human homolog of patched, a candidate gene for the basal cell nevus syndrome. *Science* 272, 1668-1671.
- Josephson, L., Kircher, M.F., Mahmood, U., Tang, Y., and Weissleder, R. (2002). Near-infrared fluorescent nanoparticles as combined MR/optical imaging probes. *Bioconjug Chem* 13, 554-560.
- Katoh, Y., and Katoh, M. (2009). Hedgehog target genes: mechanisms of carcinogenesis induced by aberrant hedgehog signaling activation. *Curr Mol Med* 9, 873-886.
- Kaul, G., and Amiji, M. (2004). Biodistribution and targeting potential of poly(ethylene glycol)-modified gelatin nanoparticles in subcutaneous murine tumor model. *J Drug Target* 12, 585-591.

- Kircher, M.F., Mahmood, U., King, R.S., Weissleder, R., and Josephson, L. (2003). A multimodal nanoparticle for preoperative magnetic resonance imaging and intraoperative optical brain tumor delineation. *Cancer Res* 63, 8122-8125.
- Kirkpatrick, C.A., and Selleck, S.B. (2007). Heparan sulfate proteoglycans at a glance. *J Cell Sci* 120, 1829-1832.
- Klerk, C.P., Smorenburg, S.M., Otten, H.M., Lensing, A.W., Prins, M.H., Piovella, F., Prandoni, P., Bos, M.M., Richel, D.J., van Tienhoven, G., *et al.* (2005). The effect of low molecular weight heparin on survival in patients with advanced malignancy. *J Clin Oncol* 23, 2130-2135.
- Kurosawa, N., Chen, G.Y., Kadomatsu, K., Ikematsu, S., Sakuma, S., and Muramatsu, T. (2001). Glypican-2 binds to midkine: the role of glypican-2 in neuronal cell adhesion and neurite outgrowth. *Glycoconj J* 18, 499-507.
- Laine, J., and Axelrad, H. (2002). Extending the cerebellar Lugaro cell class. *Neuroscience* 115, 363-374.
- Laurent, S., Forge, D., Port, M., Roch, A., Robic, C., Vander Elst, L., and Muller, R.N. (2008). Magnetic iron oxide nanoparticles: synthesis, stabilization, vectorization, physicochemical characterizations, and biological applications. *Chem Rev* 108, 2064-2110.
- Lerner, I., Hermano, E., Zcharia, E., Rodkin, D., Bulvik, R., Doviner, V., Rubinstein, A.M., Ishai-Michaeli, R., Atzmon, R., Sherman, Y., *et al.* (2011). Heparanase powers a chronic inflammatory circuit that promotes colitis-associated tumorigenesis in mice. *J Clin Invest* 121, 1709-1721.
- Li, M., Lee, K.F., Lu, Y., Clarke, I., Shih, D., Eberhart, C., Collins, V.P., Van Meter, T., Picard, D., Zhou, L., *et al.* (2009). Frequent amplification of a chr19q13.41 microRNA polycistron in aggressive primitive neuroectodermal brain tumors. *Cancer Cell* 16, 533-546.
- Liu, C.J., Lee, P.H., Lin, D.Y., Wu, C.C., Jeng, L.B., Lin, P.W., Mok, K.T., Lee, W.C., Yeh, H.Z., Ho, M.C., *et al.* (2009). Heparanase inhibitor PI-88 as adjuvant therapy for hepatocellular carcinoma after curative resection: a randomized phase II trial for safety and optimal dosage. *J Hepatol* 50, 958-968.
- Liu, Z., Yao, Z., Li, C., Lu, Y., and Gao, C. (2011). Gene expression profiling in human high-grade astrocytomas. *Comp Funct Genomics* 2011, 245137.
- LoRusso, P.M., Rudin, C.M., Reddy, J.C., Tibes, R., Weiss, G.J., Borad, M.J., Hann, C.L., Brahmer, J.R., Chang, I., Darbonne, W.C., *et al.* (2011). Phase I trial of hedgehog pathway inhibitor vismodegib (GDC-0449) in patients with refractory, locally advanced or metastatic solid tumors. *Clin Cancer Res* 17, 2502-2511.
- Loscher, W., and Potschka, H. (2005). Drug resistance in brain diseases and the role of drug efflux transporters. *Nat Rev Neurosci* 6, 591-602.
- Marchetti, D., Reiland, J., Erwin, B., and Roy, M. (2003). Inhibition of heparanase activity and heparanase-induced angiogenesis by suramin analogues. *Int J Cancer* 104, 167-174.
- Metcalf, C., and de Sauvage, F.J. (2011). Hedgehog fights back: mechanisms of acquired resistance against Smoothed antagonists. *Cancer Res* 71, 5057-5061.

- Michaud, E.J., and Yoder, B.K. (2006). The primary cilium in cell signaling and cancer. *Cancer Res* 66, 6463-6467.
- Muramatsu, T. (2002). Midkine and pleiotrophin: two related proteins involved in development, survival, inflammation and tumorigenesis. *J Biochem* 132, 359-371.
- Neunaber, C., Catala-Lehnen, P., Beil, F.T., Marshall, R.P., Kanbach, V., Baranowsky, A., Lehmann, W., Streichert, T., Ignatius, A., Muramatsu, T., *et al.* (2010). Increased trabecular bone formation in mice lacking the growth factor midkine. *J Bone Miner Res* 25, 1724-1735.
- Ng, J.M., and Curran, T. (2011). The Hedgehog's tale: developing strategies for targeting cancer. *Nat Rev Cancer* 11, 493-501.
- Northcott, P.A., Korshunov, A., Witt, H., Hielscher, T., Eberhart, C.G., Mack, S., Bouffet, E., Clifford, S.C., Hawkins, C.E., French, P., *et al.* (2011). Medulloblastoma comprises four distinct molecular variants. *J Clin Oncol* 29, 1408-1414.
- Olive, K.P., Jacobetz, M.A., Davidson, C.J., Gopinathan, A., McIntyre, D., Honess, D., Madhu, B., Goldgraben, M.A., Caldwell, M.E., Allard, D., *et al.* (2009). Inhibition of Hedgehog signaling enhances delivery of chemotherapy in a mouse model of pancreatic cancer. *Science* 324, 1457-1461.
- Osterlund, T., and Kogerman, P. (2006). Hedgehog signalling: how to get from Smo to Ci and Gli. *Trends Cell Biol* 16, 176-180.
- Pasca di Magliano, M., and Hebrok, M. (2003). Hedgehog signalling in cancer formation and maintenance. *Nat Rev Cancer* 3, 903-911.
- Peer, D., Karp, J.M., Hong, S., Farokhzad, O.C., Margalit, R., and Langer, R. (2007). Nanocarriers as an emerging platform for cancer therapy. *Nat Nanotechnol* 2, 751-760.
- Pei, Y., Moore, C.E., Wang, J., Tewari, A.K., Eroshkin, A., Cho, Y.J., Witt, H., Korshunov, A., Read, T.A., Sun, J.L., *et al.* (2012). An animal model of MYC-driven medulloblastoma. *Cancer Cell* 21, 155-167.
- Pellegrini, M., Pilia, G., Pantano, S., Lucchini, F., Uda, M., Fumi, M., Cao, A., Schlessinger, D., and Forabosco, A. (1998). Gpc3 expression correlates with the phenotype of the Simpson-Golabi-Behmel syndrome. *Dev Dyn* 213, 431-439.
- Perrimon, N., and Bernfield, M. (2000). Specificities of heparan sulphate proteoglycans in developmental processes. *Nature* 404, 725-728.
- Pirollo, K.F., and Chang, E.H. (2008). Does a targeting ligand influence nanoparticle tumor localization or uptake? *Trends Biotechnol* 26, 552-558.
- Raizen, D.M., Cullison, K.M., Pack, A.I., and Sundaram, M.V. (2006). A novel gain-of-function mutant of the cyclic GMP-dependent protein kinase egl-4 affects multiple physiological processes in *Caenorhabditis elegans*. *Genetics* 173, 177-187.
- Ramalho, A.S., Beck, S., Farinha, C.M., Clarke, L.A., Heda, G.D., Steiner, B., Sanz, J., Gallati, S., Amaral, M.D., Harris, A., *et al.* (2004). Methods for RNA extraction, cDNA preparation and analysis of CFTR transcripts. *J Cyst Fibros* 3 *Suppl* 2, 11-15.

- Rickles, F.R. (2006). If heparanase is the answer, what is the question? *J Thromb Haemost* 4, 557-559.
- Romer, J.T., Kimura, H., Magdaleno, S., Sasai, K., Fuller, C., Baines, H., Connelly, M., Stewart, C.F., Gould, S., Rubin, L.L., *et al.* (2004). Suppression of the Shh pathway using a small molecule inhibitor eliminates medulloblastoma in *Ptc1(+/-)p53(-/-)* mice. *Cancer Cell* 6, 229-240.
- Rossi, A., Caracciolo, V., Russo, G., Reiss, K., and Giordano, A. (2008). Medulloblastoma: from molecular pathology to therapy. *Clin Cancer Res* 14, 971-976.
- Rossin, R., Pan, D., Qi, K., Turner, J.L., Sun, X., Wooley, K.L., and Welch, M.J. (2005). ⁶⁴Cu-labeled folate-conjugated shell cross-linked nanoparticles for tumor imaging and radiotherapy: synthesis, radiolabeling, and biologic evaluation. *J Nucl Med* 46, 1210-1218.
- Rudin, C.M., Hann, C.L., Laterra, J., Yauch, R.L., Callahan, C.A., Fu, L., Holcomb, T., Stinson, J., Gould, S.E., Coleman, B., *et al.* (2009). Treatment of medulloblastoma with hedgehog pathway inhibitor GDC-0449. *N Engl J Med* 361, 1173-1178.
- Rutkowski, S., von Hoff, K., Emser, A., Zwiener, I., Pietsch, T., Figarella-Branger, D., Giangaspero, F., Ellison, D.W., Garre, M.L., Biassoni, V., *et al.* (2010). Survival and prognostic factors of early childhood medulloblastoma: an international meta-analysis. *J Clin Oncol* 28, 4961-4968.
- Sakamoto, K., and Kadomatsu, K. (2012). Midkine in the pathology of cancer, neural disease, and inflammation. *Pathol Int* 62, 445-455.
- Saunders, S., Paine-Saunders, S., and Lander, A.D. (1997). Expression of the cell surface proteoglycan glypican-5 is developmentally regulated in kidney, limb, and brain. *Dev Biol* 190, 78-93.
- Schutter, D.J., and van Honk, J. (2005). The cerebellum on the rise in human emotion. *Cerebellum* 4, 290-294.
- Sheng, Y., Liu, C., Yuan, Y., Tao, X., Yang, F., Shan, X., Zhou, H., and Xu, F. (2009). Long-circulating polymeric nanoparticles bearing a combinatorial coating of PEG and water-soluble chitosan. *Biomaterials* 30, 2340-2348.
- Siegel, R., Naishadham, D., and Jemal, A. (2012). Cancer statistics, 2012. *CA Cancer J Clin* 62, 10-29.
- Skvara, H., Kalthoff, F., Meingassner, J.G., Wolff-Winiski, B., Aschauer, H., Kelleher, J.F., Wu, X., Pan, S., Mickel, L., Schuster, C., *et al.* (2011). Topical treatment of Basal cell carcinomas in nevoid Basal cell carcinoma syndrome with a smoothed inhibitor. *J Invest Dermatol* 131, 1735-1744.
- Stipp, C.S., Litwack, E.D., and Lander, A.D. (1994). Cerebroglycan: an integral membrane heparan sulfate proteoglycan that is unique to the developing nervous system and expressed specifically during neuronal differentiation. *J Cell Biol* 124, 149-160.
- Taipale, J., Chen, J.K., Cooper, M.K., Wang, B., Mann, R.K., Milenkovic, L., Scott, M.P., and Beachy, P.A. (2000). Effects of oncogenic mutations in Smoothed and Patched can be reversed by cyclopamine. *Nature* 406, 1005-1009.
- Taylor, M.D., Northcott, P.A., Korshunov, A., Remke, M., Cho, Y.J., Clifford, S.C., Eberhart, C.G., Parsons, D.W., Rutkowski, S., Gajjar, A., *et al.* (2012). Molecular subgroups of medulloblastoma: the current consensus. *Acta Neuropathol* 123, 465-472.

- Tempe, D., Casas, M., Karaz, S., Blanchet-Tournier, M.F., and Concordet, J.P. (2006). Multisite protein kinase A and glycogen synthase kinase 3beta phosphorylation leads to Gli3 ubiquitination by SCFbetaTrCP. *Mol Cell Biol* 26, 4316-4326.
- Tremblay, M.R., Lescarbeau, A., Grogan, M.J., Tan, E., Lin, G., Austad, B.C., Yu, L.C., Behnke, M.L., Nair, S.J., Hagel, M., *et al.* (2009). Discovery of a potent and orally active hedgehog pathway antagonist (IPI-926). *J Med Chem* 52, 4400-4418.
- Veiseh, M., Gabikian, P., Bahrami, S.B., Veiseh, O., Zhang, M., Hackman, R.C., Ravanpay, A.C., Stroud, M.R., Kusuma, Y., Hansen, S.J., *et al.* (2007). Tumor paint: a chlorotoxin: Cy5.5 bioconjugate for intraoperative visualization of cancer foci. *Cancer Res* 67, 6882-6888.
- Veiseh, O., Sun, C., Fang, C., Bhattarai, N., Gunn, J., Kievit, F., Du, K., Pullar, B., Lee, D., Ellenbogen, R.G., *et al.* (2009). Specific targeting of brain tumors with an optical/magnetic resonance imaging nanoprobe across the blood-brain barrier. *Cancer Res* 69, 6200-6207.
- Vlodavsky, I., and Friedmann, Y. (2001). Molecular properties and involvement of heparanase in cancer metastasis and angiogenesis. *J Clin Invest* 108, 341-347.
- Volk, H.A., and Loscher, W. (2005). Multidrug resistance in epilepsy: rats with drug-resistant seizures exhibit enhanced brain expression of P-glycoprotein compared with rats with drug-responsive seizures. *Brain* 128, 1358-1368.
- Wang, B., and Li, Y. (2006). Evidence for the direct involvement of {beta}TrCP in Gli3 protein processing. *Proc Natl Acad Sci U S A* 103, 33-38.
- Wang, V.Y., and Zoghbi, H.Y. (2001). Genetic regulation of cerebellar development. *Nat Rev Neurosci* 2, 484-491.
- Watanabe, K., Yamada, H., and Yamaguchi, Y. (1995). K-glypican: a novel GPI-anchored heparan sulfate proteoglycan that is highly expressed in developing brain and kidney. *J Cell Biol* 130, 1207-1218.
- Winkler, J.D., Isaacs, A., Holderbaum, L., Tatard, V., and Dahmane, N. (2009). Design and synthesis of inhibitors of Hedgehog signaling based on the alkaloid cyclopamine. *Org Lett* 11, 2824-2827.
- Yang, L., Xie, G., Fan, Q., and Xie, J. (2010). Activation of the hedgehog-signaling pathway in human cancer and the clinical implications. *Oncogene* 29, 469-481.
- Yang, Z.J., Ellis, T., Markant, S.L., Read, T.A., Kessler, J.D., Bourbonoulas, M., Schuller, U., Machold, R., Fishell, G., Rowitch, D.H., *et al.* (2008). Medulloblastoma can be initiated by deletion of Patched in lineage-restricted progenitors or stem cells. *Cancer Cell* 14, 135-145.
- Yauch, R.L., Dijkgraaf, G.J., Alicke, B., Januarío, T., Ahn, C.P., Holcomb, T., Pujara, K., Stinson, J., Callahan, C.A., Tang, T., *et al.* (2009). Smoothed mutation confers resistance to a Hedgehog pathway inhibitor in medulloblastoma. *Science* 326, 572-574.
- Yayon, A., Klagsbrun, M., Esko, J.D., Leder, P., and Ornitz, D.M. (1991). Cell surface, heparin-like molecules are required for binding of basic fibroblast growth factor to its high affinity receptor. *Cell* 64, 841-848.

Zhao, X., Liu, Z., Yu, L., Zhang, Y., Baxter, P., Voicu, H., Gurusiddappa, S., Luan, J., Su, J.M., Leung, H.C., *et al.* (2012). Global gene expression profiling confirms the molecular fidelity of primary tumor-based orthotopic xenograft mouse models of medulloblastoma. *Neuro Oncol* 14, 574-583.

Zurawel, R.H., Chiappa, S.A., Allen, C., and Raffel, C. (1998). Sporadic medulloblastomas contain oncogenic beta-catenin mutations. *Cancer Res* 58, 896-899.

Michelle Jeung-Eun Lee

Education:

- Mar 2013 Ph.D. Neurobiology & Behavior
Targeted therapies for medulloblastoma
Advisor: Dr. James M. Olson
University of Washington; Fred Hutchinson Cancer Research Center
Seattle, WA
- Jun 2007 B.S. Bio And Brain Engineering,
Korea Advanced Institute of Science and Technology, Daejeon, Korea

Research Experience:

- Jul 2008 – Mar 2013 Doctoral Candidate in Neurobiology & Behavior
Fred Hutchinson cancer Research Center, Seattle, WA
*Understanding drug resistance mechanisms against Sonic hedgehog pathway
targeted therapy and strategies to overcome resistance*
Advisor: Dr. James M. Olson
- Apr 2008 – Jun 2008 Graduate Research Assistant
University of Washington, Seattle, WA
Department of Computer Science and Engineering
*Development of feedback distorted rehabilitation paradigm for stroke patients:
coordinated multi-fingered "twisting" task*
Advisor: Dr. Yoky Matsuoka
- Jan 2008 – Mar 2008 Graduate Research Assistant
Fred Hutchinson cancer Research Center, Seattle, WA
*Characterization of pharmacokinetic and biodistribution properties of MRI and
NIR fluorescence dual modality tumor targeting agent (Chlorotoxin based)*
Advisor: Dr. James M. Olson
- Sep 2007 – Dec 2007 Graduate Research Assistant
University of Washington, Seattle, WA
Department of Neurological Surgery, Seattle, WA
Understanding the role of astrocytes in the pathogenesis of acquired epilepsy
Advisor: Dr. Raimondo D'Ambrosio
- Dec 2005 – Feb 2006 Undergraduate Research
Korea Advanced Institute of Science and Technology
Department of Bio And Brain Engineering, Daejeon, Korea
Memory and Dementia Clinic, Department of Neurology, Samsung Medical
Center, Seoul, Korea
Advisor: Dr. Yong Jeong
- Jun 2005 – Aug 2005 Undergraduate Research
Boston University, Center for Biomedical Imaging, Boston, MA
*Investigating audio-visual cross-modal interaction within the brain using
functional MRI (fMRI) in human subjects*
Advisor: Dr. Daeshik Kim

Publications:

Lee, M.J., Hatton, B.A., Villavicencio, E.H., Khanna, P.C., Friedman, S.D., Ditzler, S., *et al.* (2012). Hedgehog pathway inhibitor saridegib (IPI-926) increases lifespan in a mouse medulloblastoma model. *Proc Natl Acad Sci U S A* 109, 7859-7864.

Lee, MJ-E, Veiseh, O., Bhattarai, N., Sun, C., Hansen, S.J., *et al.* (2010) Rapid Pharmacokinetic and Biodistribution Studies Using Chlorotoxin-Conjugated Iron Oxide Nanoparticles: A Novel Non-Radioactive Method. *PLoS ONE* 5(3): e9536. doi:10.1371/journal.pone.0009536

Presentations:

Lee, M.J., Hatton, B.A., Villavicencio, E.H., Khanna, P.C., Friedman, S.D., Ditzler, S., *et al.* (2010). Identifying Mechanisms of Drug Resistance to a Shh Pathway Inhibitor in a Medulloblastoma Mouse Model. Society For Neuroscience (Sfn) San Diego, CA, USA. Poster Presentation.

Olson, J.M., Bahrami, S., Veiseh, M., Hatton, B., **Lee, M.J.**, Klinghoffer, R. (2010). A Porous Needle Array Technology Platform for Multiplexed *in vivo* Comparison of Oncology Drug Efficacy. Fl, USA. Poster Presentation.

Suh, M.K., **Lee, J.E.**, Jeong, Y., Kim, K.M., Lee, K.H., Na, D.L. (2006). Lip Reading in Patients with Apraxia of Speech. *Journal of The Korean Neurological Association*. Seoul, Korea. Poster Presentation.

Lee, M.J., Lee, K.D., Lee, S.Y. (2006). Unsupervised Feature Extraction for the Representation and Recognition of Lip Motion Video. International Conference on Intelligent Computing (ICIC2006). Published at Computational Intelligence And Bioinformatics, Springer Lecture Notes On Bioinformatics (LNCS/LNBI 4115). Oral Presentation.

Lee, M.J., Lee, K.D., Lee, S.Y. (2005) Unsupervised Extraction of Multi-Frame Features from Lip Motion Video. Computational Neuroscience Annual Meeting (CNS). Madison, Wisconsin, USA. Poster Presentation.

Fellowships:

Sep 2010 – Mar 2013 NIH Predoctoral Training Grant For Neurobiology (T32)

Awards/Honors:

2011	Korea-US Science Cooperation Center (KUSCO)-KSEA Graduate Scholarship
2010	Best Presentation Award, KSEA Northwest Regional Conference (NWRC)
2008	RIKEN Student Travel Grant
	RIKEN Brain Science Institute Summer Program, Saitama, Japan
2003 – 2007	KAIST Undergraduate Scholarship, KAIST, Korea
2006	Korea National Science Scholarship, KAIST, Korea
2005	Student Travel Grant, Computational Neuroscience meeting (CNS)

Teaching and Mentoring Experience:

Mar 2008 – Jun 2009 University of Washington, Seattle, WA
Teaching Assistant for undergraduate introductory Neurobiology course

Dec 2011 – May 2012 Northwest Association for Biomedical Research, Seattle, WA
Mentored two high school students on their biomedical research expo projects

Scientific Outreach and Advocacy

2010-2013 Neurobiology & Behavior Community Outreach
University of Washington, Seattle, WA

Service

2012 – present Senior Advisor, KSEA – Seattle Chapter, Young Generation (YG) Group
2011 – present Young Generation Committee, KSEA Headquarter
2012 Organizer, KSEA Young Generation Technical & Leadership Conference
2011 Co-Chair, KSEA Young Generation & Professional Forum, US-Korea Conference
2011 Program Chair, KSEA Young Generation Technical & Leadership Conference
2010 Young Generation Forum Session Chair, KSEA North-West Regional Conference
2010 KSEA Young Generation Associate Director, KSEA Headquarter
2009, 2010 Committee, KSEA National Science Competition – Seattle Chapter